UNIVERSITÀ DEGLI STUDI DI PADOVA

Dipartimento di Fisica e Astronomia "Galileo Galilei"

Master degree in Physics

Final Dissertation

Millikelvin temperatures testbed for future dark matter experiments with quantum-limited amplifiers

Thesis supervisor

Prof. Caterina Braggio

Candidate

Enrico Bogoni

Academic Year 2023/2024

Contents

Introduction

At the low energy frontier of particle physics, experiments that test the validity of fundamental theories require detectors at the ultimate level of sensitivity allowed by quantum mechanics. In cavity-based searches of axion dark matter (DM), 3D resonators and the first stage of amplification of the receiver electronics, a Josephson parametric amplifier (JPA), are cooled down to ultra-cryogenic temperatures to minimize thermal noise. This is accomplished within dilution refrigerators, that are equipped with microwave components and devices that have to be carefully tested and characterised in order to assess the noise introduced by the receiver. This thesis presents the characterisation and optimization of a receiver chain operated in the new dilution refrigerator available at LNL INFN laboratories that will be used for future DM searches. I will also describe in detail how it was equipped with all the necessary RF components to run the receivers tests while not impacting on the base temperature, i.e. about 7 mK, reached during commissioning.

Chapter 1

Axions

Three open questions in the physical description of our universe might be answered by probing the existence of axions: the strong CP problem, the matter-antimatter asymmetry and the composition of dark matter. The presentation of the strong CP problem and matter-antimatter asimmetry and the solution given by the Peccei-Quinn mechanism is discussed in section 1.1 In section 1.2 I will discuss the evidences of DM existence and derive useful axion properties assuming it constitutes the entirety of DM. The axion-matter interactions, the parameter space of experimental search and the principal axion models are treated in section 1.3.

1.1 Strong CP problem and Peccei-Quinn solution

The Standard Model of particle physics provides a successful description of the visible matter in the Universe for all fundamental interactions other than gravity. However it presents some unanswered questions. For each matter particle in the Standard Model (SM) there exists an anti-particle with opposite charges, that has been experimentally observed at colliders. One thus would expect an equal concentration of matter and antimatter in the universe [19]. However, from astrophysical and cosmological observations we know that most of the visible material is composed of matter, without any large concentration of antimatter. It has been shown that, to create an imbalance in matter and antimatter, the Sakharov conditions, including the existence of CP violation during the first seconds after the Big Bang, must be satisfied [60].

CP violation in electro-weak interaction was experimentally observed [78], however, this mechanism is insufficient to explain matter-antimatter asymmetry. Moreover the SM predicts a CP violation for the strong nuclear interaction, that is not found: this is the "strong-CP problem" . The amount of P and CP violation in the strong interactions is controlled by a parameter, the angle $\theta_{\rm QCD}$, which appears as the coefficient of a P and CP odd term in the SM action density [67]

$$\mathcal{L}_{\rm SM} = ... + \theta_{\rm QCD}\frac{g_s^2}{32\pi^2}G^a_{\mu\nu}\ \tilde{G}^{a\mu\nu} \tag{1.1}$$

where the $G^a_{\mu\nu}$, $a = 1, 2, ...8$, are the field strengths of Quantum Chromodynamics (QCD) and g_s is the QCD coupling constant.

The main observable effect of the expected strong CP violation is the presence of an electric dipole moment (EDM) of the neutron d_n. In fact the neutron EDM depends on $\bar{\theta}$ that is the sum of the strong and weak interactions contributions. For small $\bar{\theta}$ to the neutron EDM is of order [67]

$$d_n \sim \bar{\theta}\frac{m_u m_d}{m_u + m_d}\frac{1}{\Lambda_{\rm QCD}}\frac{e}{m_n} \sim 3\cdot 10^{-16}\bar{\theta}e{\rm cm}\ , \tag{1.2}$$

where m_u and m_d are the up and down quark masses, m_n is the neutron mass, e is the electron charge and $\Lambda_{\rm QCD}$ the QCD scale. The experimental upper limit on the neutron EDM is $|d_n| < 3{\cdot}10^{-26}e$ cm [48], therefore $\theta_{\rm QCD}$ should be less than of order 10^{-10}.

The axion is the most popular solution to the strong CP problem. It appeared first in a model proposed by Roberto Peccei and Helen Quinn in 1977 [47, 46]. They introduced a new symmetry, called

the PQ symmetry, which is a global axial $U(1)$ symmetry, mathematically equivalent to a rotation about a single axis. "Global" and "axial" mean respectively that the symmetry transformation is the same everywhere and for all time, and that it acts differently on left-handed and right-handed particles[19]. Moreover it is an exact symmetry of the classical action, it is spontaneously broken, and has a color anomaly, i.e. it is explicitly broken by the non-perturbative QCD instanton effects that make physics depend on the value of θ_{QCD} [67].

With the PQ symmetry, a new bosonic field beyond the single Higgs boson of the Standard Model is introduced. At high temperatures, such as in the early universe, the PQ symmetry is evident in all particle interactions. However, when the temperature is sufficiently low, the spontaneous symmetry breaking (SSB) hides the symmetry. In particle physics, a SSB corresponds to the appearance of the massless Nambu-Goldstone boson [42, 29], that in this case is the axion. The parameter θ_{QCD} is therefore replaced by $a(x)/f_a$ where $a(x)$ is the axion dynamical pseudo-scalar field and f_a its decay constant, a quantity with dimension of an energy proportional to that at which the PQ symmetry is spontaneously broken.

With only the spontaneous symmetry breaking, the massless axion field could a priori take any value. At sufficiently low temperature, QCD becomes strongly-coupled and confines quarks and gluons into the bound-state protons, neutrons and other hadrons. This phase transition breaks the PQ symmetry introducing an effective potential for $a(x)$ [74, 76]. The minimum of this effective potential is shown to be at $a(x) = 0$ [72]. The Strong CP Problem is solved after the $a(x)$ field settles there. Notice that after the explicit symmetry breaking the axion acquires a mass m_a, inversely proportional to f_a, with a Compton frequency, that is the frequency of a photon whose energy is the same as the rest energy of the particle, $\nu_a = m_a c^2/h$, where h is the Planck constant and c is the speed of light. Here the contribution of θ_{QCD} vanishes, setting the neutron EDM to zero.

The original Peccei-Quinn-Weinberg-Wilczek (PQWW) model [74, 76] predicts f_a of the order the electroweak scale, thus an axion relatively strongly coupled and heavy, with an m_a of order 100 keV. However this model was soon ruled out by a variety of laboratory experiments. It was later shown that the PQ symmetry doesn't have to be necessarily broken at the electroweak scale [26], but it may be broken at an arbitrarily high energy. When f_a is really large, the axion is very light and extremely weakly coupled. This axion is called the "invisible axion".

A direct solution to the problem of the matter-antimatter asymmetry through axions was recently proposed. The mechanism called axiogenesis generates the excess of matter from the rotation of the QCD axion. Thus the rotation of a PQ charged scalar field is induced by the PQ symmetry that might have been explicitly broken in the early universe [20, 77].

1.2 Dark matter and axions

From the 1930s different measurements hinted the presence of matter whose interaction seemed only of gravitational nature. A it is not visible, it was called dark matter (DM). Observation of the rotation speeds of spiral galaxies showed that objects far from the center of the rotating disk are traveling at a speed much higher than expected [5, 59]. In fact, from luminous object mass measurements, over a certain radius the mass M is expected to be constant, with the velocity v increasing as $v = \sqrt{\frac{GM}{r}}$, with G the gravitational constant. Instead, it is found that v plateaus as shown in Fig. 1.1 for the galaxy M33.

The discrepancy between measured rotation curves and those expected from visible matter can be explained assuming a DM halo in the galaxy. Other types of observations support this hypothesis including gravitational lensing and the Cosmic Microwave Background (CMB).

The first occurs when large masses in the universe bends light towards themselves. In this case more gravitational lensing is observed compared to what is expected from the visible mass distributions [41].

The CMB power spectrum instead encodes information on the conditions of the early universe, in particular the baryon density Ω_b, composed mainly of matter that is already known and described by the SM, and the matter density Ω_m comprising all the matter present in the universe. Planck measurements of CMB anisotropies gave $\Omega_b = 0.0486 \pm 0.0010$ and $\Omega_m = 0.3089 \pm 0.0062$ [52]. DM

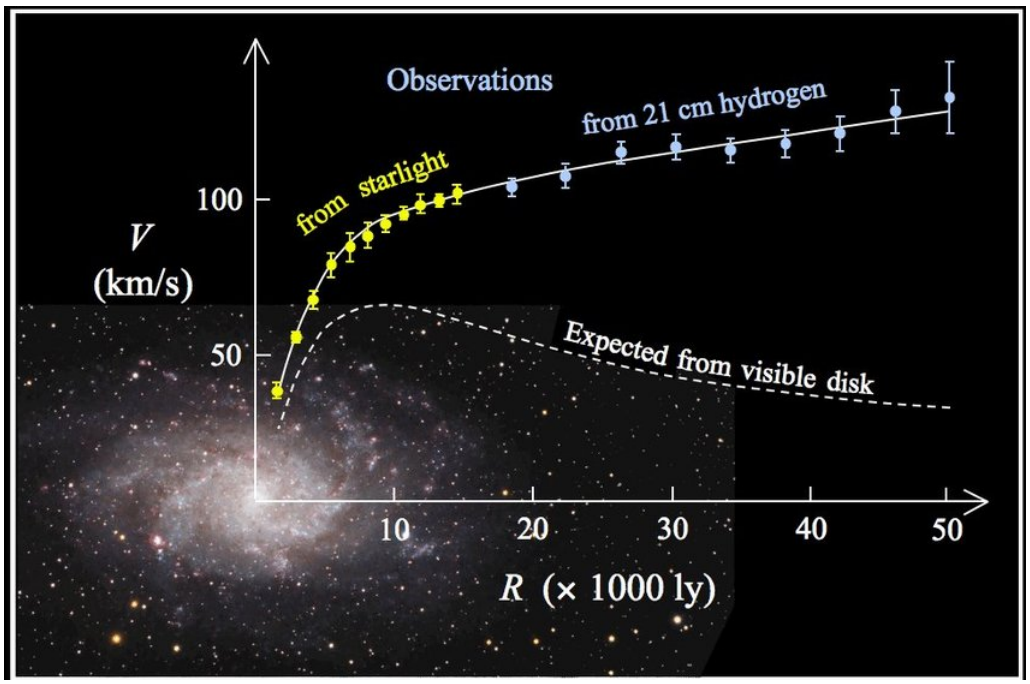

Figure 1.1: The image of M33 and the corresponding rotation curve. In yellow and light blue the observed velocities, fitted with a solid line, while the dotted line represents the velocities expected form the mass of visible matter [62]

should then be composed of non-baryonic matter with density $\Omega_m - \Omega_b$, making up about the 85% of the matter in the universe. The case of a non-baryonic DM is where cosmology meets particle physics and candidates are searched between particles beyond the SM, able to also explain other open problems in fundamental physics.

A main, long-sought DM candidate is the weakly-interacting massive particle (WIMP). These particles have been extensively searched in collider experiments and underground detectors in the last 30 years, excluding their presence in a vast portion of the parameter space. The scientific community interest therefore moved to weakly interacting sub-eV particles (WISPs), like low-mass bosons that may populate the Universe in a coherent wave-like state.

The axion has recently become a favored DM candidate, owing to its small interaction with SM particles, for its long De Broglie length and for the fact that it can solve, as detailed in the previous section, the strong CP problem. Moreover axions thermalize through their gravitational self-interactions and, as a result, form a Bose-Einstein condensate (BEC) and observations support the hypothesis that DM is a rethermalizing BEC [67].

Experimentalits rely on models to devise experiments, here I describe the most relevant properties and assumptions that are made for axion detection. A first assumption that is made when axion DM experiments are devised, is that it constitutes all the DM, so $\rho_a = \rho_{\rm DM}$. Axion searches literature typically assume a local dark matter density of $\rho_a \approx 0.45\,{\rm GeV/cm^3}$ [57].

The velocity of the DM halo is estimated assuming that its time averaged kinetic and potential energy are in equilibrium, related by the virial theorem. Their virial velocity is measured as $\bar{v} = \langle v^2\rangle^{1/2} \approx 270\,{\rm km/s} \approx 10^{-3}{\rm c}$ where the bracketed $\langle v^2\rangle$ is the second moment of the Maxwell-Boltzmann velocity distribution.

For an axion of mass $m_a \sim 40\,\mu{\rm eV}$ ($\nu_a \sim 10\,{\rm GHz}$), the de Broglie wavelength is $\lambda_a = h/m_a\bar{v} \sim 1.7\times10^{-8}\,{\rm eV}^{-1} \sim 34$ m and is approximately equal to the axion coherence length. We can also define a coherence time $\tau_a = \lambda_a/\bar{v} \sim 126\,\mu{\rm s}$ and the axion quality factor $Q_a = m_a c^2\tau_a/h = (c/\bar{v})^2 \sim 1.2\times10^6$. This quality factor is the expected width of the frequency peak of axion field oscillations [40, 14].

In some models [67] the DM halo is not virialized and overlapping flows, called "caustic", should be observed. Earth should be located close to a caustic, and this model DM parameters are calculated as $\bar{v} \sim 520\,{\rm km/s}$ and $\rho_{\rm DM} \geq 6{\rm GeV/cm^3}$, corresponding to much larger axion quality factors.

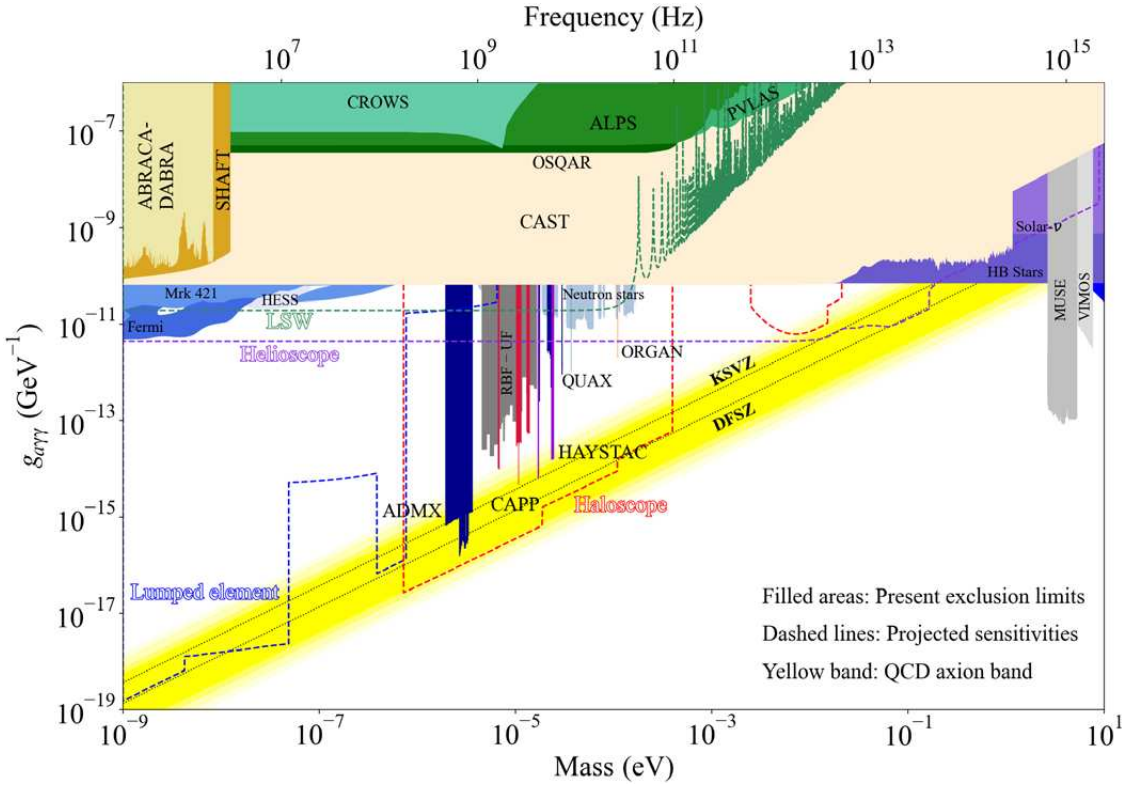

Figure 1.2: Experimental exclusion limits on the axion-photon coupling versus axion mass. The projected sensitivities are represented by dashed lines. The two benchmark models are represented by the diagonal dashed lines with the uncertainty band in yellow. Filled areas represent the exclusion limits and are labelled with the experiments and observation that probed them [63]

1.3 Axion interactions and parameter space

The axion mass can be computed in terms of the strong nuclear force by considering the axion-pion mixing. Since they have the same quantum numbers, the pion's mass gives rise to a small mass for the axion m_a. In terms of the decay constant f_a, the axion mass is given by [74]

$$m_a \simeq \frac{\sqrt{m_u m_d}}{m_u + m_d} \frac{f_\pi m_\pi}{f_a} \simeq 6 \cdot 10^{-6} \text{ eV} \left(\frac{10^{12} \text{ GeV}}{f_a} \right) \quad , \tag{1.3}$$

where m_π is the pion mass, and $f_\pi \simeq 93$ MeV the pion decay constant.

The axion does not interact only with quarks and gluons, but also with the other SM particles. These can be expressed by the non-relativistic Hamiltonian:[19]

$$\mathcal{H} = \underbrace{\sqrt{\frac{\epsilon_0}{\mu_0}} g_{a\gamma\gamma} \int a\mathbf{E} \cdot \mathbf{B} dV}_{photons} + \underbrace{\hbar c \nabla a \cdot \hat{\mathbf{S}} g_{aff}}_{fermions} + \underbrace{\sqrt{\epsilon_0 (\hbar c)^3} g_{\text{EDM}} a \hat{\mathbf{S}} \cdot \mathbf{E}}_{EDM}, \tag{1.4}$$

where a is the axion field measured in units energy, $g_{a\gamma\gamma}$ is the axion coupling to photons measured in units of inverse energy, g_{aff} is the axion's coupling to fermions f dependent on the particle in question and g_{EDM} is the strength of a nuclear EDM induced by the axion. $\mathbf{E}$ and $\mathbf{B}$ are the electric and magnetic fields, and $\hat{\mathbf{S}}$ is the direction of the spin of particle in question. ϵ_0 and μ_0 are the permittivity and permeability of free space respectively and $\hbar = h/2\pi$ is the reduced Planck's constant.

By interacting with $\mathbf{E}\cdot\mathbf{B}$, axion DM would manifest as an additional electrical current or anomalous magnetic field [66]. In fact the addition of the axion field modifies Maxwell's equations of electromagnetism. In turn axion DM coupling to nuclear and electron spins would cause these spins to precess, as in a magnetic field, with an anomalous magnetization caused by the axion itself[7, 15].

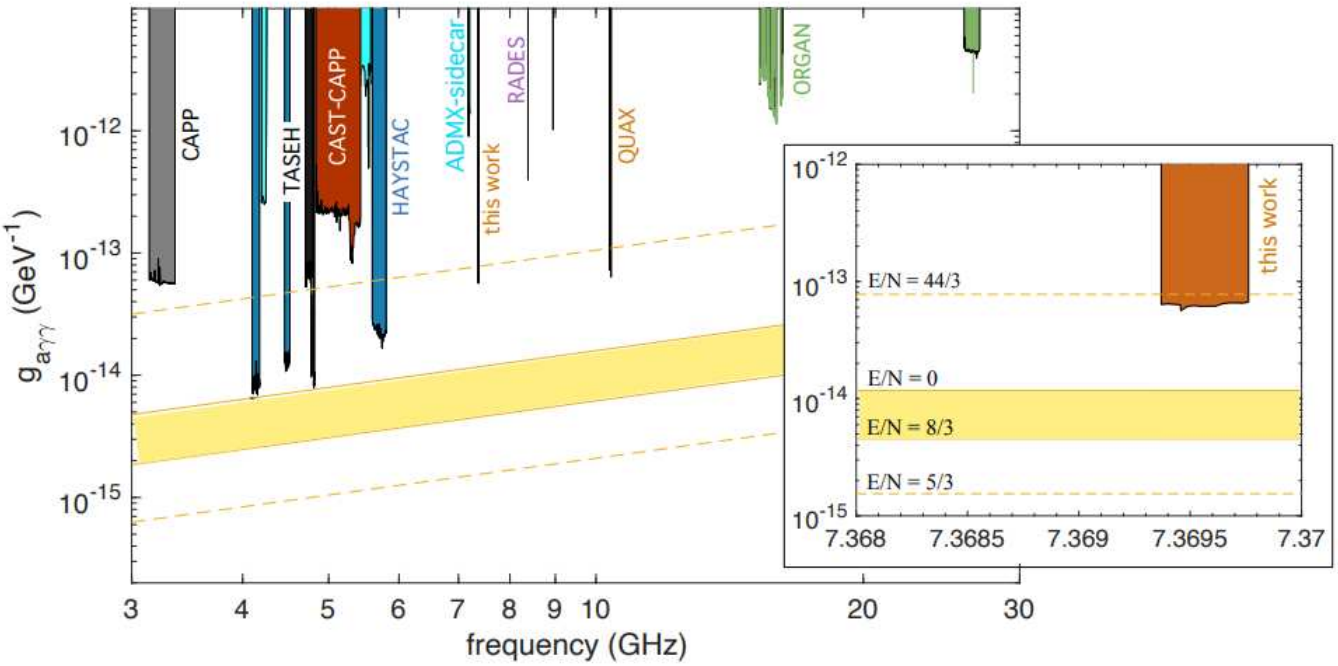

Figure 1.3: Up-to-date experimental exclusion limits on the axion-photon coupling versus axion frequency, in the haloscope frequency range. Solid colour area represent the exclusion limits while the yellow area represent the sensitivity between the benchmark models, with less expected model values represented by the dashed lines. In particular latest QUAX experimental results with an Single-photon counter are shown on the right insert [12].

As a consequence of Effective Field Theory [75], axion couplings are inversely proportional to the scale of symmetry breaking:

$$g_i \sim \frac{1}{f_a}\,. \tag{1.5}$$

As this energy f_a could be very high, the axion interactions could be very weak, as required by the experimental constraints. Comparing equations (1.3) and (1.5), we see that the QCD axion couplings obey:

$$g_i \propto m_a. \tag{1.6}$$

From these relations we can draw the parameter space map, as in Fig. 1.2 and 1.3, whose axis represent the coupling parameters g_i and the axion mass m_a or frequency ν_a. Experimental bounds are typically reported in axion exclusion plots, where the yellow band represents the family of models for the QCD axion. In contrast to axion-like particles (ALPs), for these axions the coupling parameters can be calculated depending on the particular extension of the axion mechanism to the SM [19]. In models a new complex field Φ is introduced, which gains a non-zero vacuum expectation value that breaks the PQ symmetry spontaneously. The axion is related to the phase of Φ by $a = N f_a \theta_{QCD}$, where N is an integer, the "colour anomaly", model dependent.

The diagonal yellow line in Fig. 1.2 is bounded by the two benchmark models Kim-Shifman-Vainshtein-Zakharov (KSVZ) and Dine-Fischler-Srednicki-Zhitnitsky (DFSZ).

The KSVZ model introduces two new fields in the SM: the Peccei-Quinn field Φ and a new exotic quark $\mathcal{Q}$.

The DFSZ model instead splits the Higgs into two doublets, avoiding the introduction of the new quark and mediating the axion-gluon coupling with the SM quarks. In this model a direct coupling between the axion and the electron g_{aee} is present. A different strength of photon coupling $g_{a\gamma\gamma}$ is found between the models due to the different mediators [19]:

$$g_{a\gamma\gamma} = \frac{\alpha_{em}}{2\pi f_a}\left(\frac{\mathcal{E}}{N} - 1.92\right) = \left(0.203\frac{\mathcal{E}}{N} - 0.39\right)\frac{m_a}{\mathrm{GeV}^2}, \tag{1.7}$$

where α_{em} is the electromagnetic fine structure constant and $\mathcal{E}$ is the electromagnetic anomaly of the PQ symmetry and N the colour anomaly. The said dependence on the model is on these anomaly parameters, that give for the DFSZ model $\frac{\mathcal{E}}{N} = \frac{8}{3}$, whereas for the described KSVZ model $\frac{\mathcal{E}}{N} = 0$.

A thorough description of the different axion models can be found in Ref. [24].

1.3.1 Astrophysical and cosmological bounds

Astrophysical considerations can provide the best clues to the range of allowed values for the axion mass in the parameter space map.

The lower bound results from a property known as "black hole superradiance". In fact rapidly spinning black holes would quickly spin down if a resonant boson existed, and so the observation of spinning and old black holes may place exclusions on axion masses. Stellar mass black holes with spins measured from X-ray images exclude the range $1 \times 10^{-13}\,\text{eV} \leq m \leq 2 \times 10^{-11}\,\text{eV}$ [70].

An upper bound on m_a can be derived from the axion-nucleon coupling g_{aNN}, that leads to the emission of axions inside a collapsing supernova core. The produced axions interact weakly with the surrounding nuclear matter, and so can escape from the core. Their production cools the supernova more quickly and reduces the time interval of neutrino emission, leading to a lower neutrino flux. The flux produced in the supernova SN1987A [55] was observed on Earth detectors, and the results were consistent with predictions of standard supernova models. Thus, the axion production rate must be low, leading to $m_a \lesssim 2 \times 10^{-2}$ eV.

The superradiance and SN1987A bounds thus limit the QCD axion natural frequency to the range:

$$10\ \text{kHz} \lesssim \nu_a \lesssim 10\ \text{THz}. \tag{1.8}$$

The coupling between axions and photons would also allow axions to be copiously produced in stars. This would create an additional cooling mechanism for the star and would therefore alter the course of stellar evolution. This effect can also be used to constrain $g_{a\gamma\gamma}$, requiring $g_{a\gamma\gamma} < 6.6 \times 10^{-11}\,\text{GeV}^{-1}$ over a very wide range of masses [4].

Chapter 2

Haloscopes and Scan rate

Axion experiments mainly rely on the axion-photon interaction for the detection of the hypotetical particle [67, 63, 31]. In light through wall (LSW) experiments, axions are generated in the laboratory through intense light fields resonating within Fabry-Perot cavities in the presence of strong magnetic fields, while in helioscopes axions are sourced by the Sun. In this thesis we focus on the haloscope detector that probes axions as a main constituent of the galaxy DM halo. This is the most sensitive axion detector that is the only one that reached the QCD axion band.

The process that underlies the haloscope method is the inverse Primakoff effect, typical of pions. It consists in the reversed time process of the axion natural decay in two photons, changing one of the photons with a classical electromagnetic field, as in the Feynman diagram in Fig. 2.1 The classical homogeneous field is obtained through a magnet and can be seen as a flux of virtual photons with which the axion scatters elastically to produce a new photon with the same polarization of the virtual ones and the total energy of the axion.

As the DM axion is a non-relativistic particle, its kinetic energy is negligible with respect to its mass energy, thus the frequency of the produced photon will be $\nu_a = m_a c^2/h$.

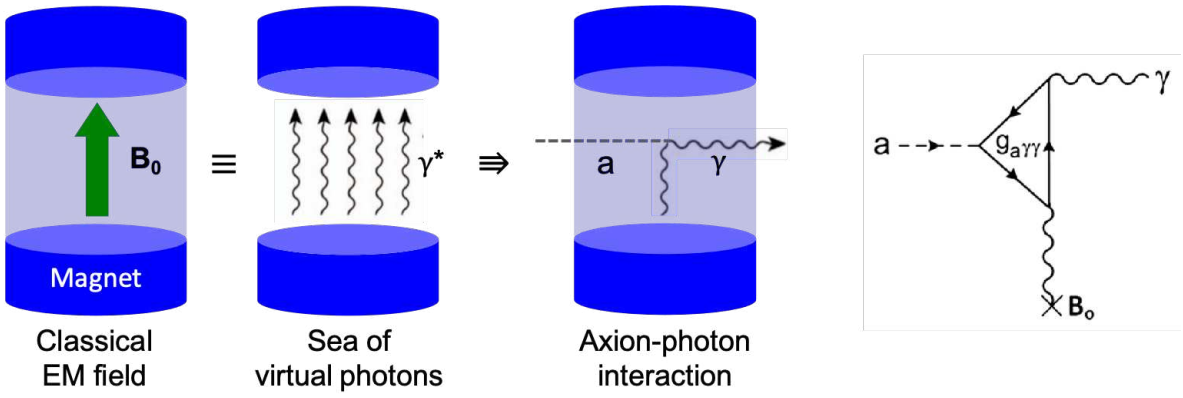

Figure 2.1: Primakoff interaction in the presence of a constant magnetic field B_0 and the relative Feynman diagram: the magnetic field can be seen as a sea of virtual photons with which the axion can interact and emit a photon of frequency ν_a [63].

The core of the haloscope is a high quality factor 3D microwave resonator in which the tiny signal corresponding to the axion to photon conversion is resonantly enhanced. The cavity is mounted in the bore of a multi-Tesla superconducting (SC) magnet.

Basic cavity theory and the derivation of the output signal are presented in section 2.1 As in best haloscopes the signal is at the level of $10^{-22} - 10^{-23}$ W, minimum noise has to be added in the receiver chain as discussed in section 2.2. In section 2.3 we obtain the haloscope scan rate formula, which is the most important figure of merit for this detectors, as it sets the speed at which the parameter space shown in section 1.3 is probed. Finally, section 2.4 deals with possible ways to improve the scan rate, focusing on the receiver chain past achievements and future improvements.

2.1 Cavity resonator

A microwave cavity can be modelled as a waveguide that extends in the z direction, in which are added two conducting faces at $z = 0$ and $z = d$. In these two ends the field is reflected and standing waves are created. In the walls and i the faces the electric and magnetic components of the field have to satisfy the boundary conditions

$$\hat{n} \times \mathbf{E} = 0, \qquad \hat{n} \cdot \mathbf{B} = 0 \tag{2.1}$$

where $\mathbf{E}$ and $\mathbf{B}$ are the electric and magnetic fields and $\hat{n}$ is the vector normal to the surface of the conductor.

The fields in cylindrical coordinates (ρ, ϕ, z) obey the Maxwell's wave equation

$$\nabla_{\perp}^2 + \left(\frac{\omega^2}{c^2} - k^2\right)\mathbf{F} = 0, \qquad \mathbf{F} = \{\mathbf{E}, \mathbf{B}\} \tag{2.2}$$

where $\nabla_{\perp}^2 = \nabla^2 - \partial^2/\partial z^2$, ω is the angular frequency, k is the wave number and c is the speed of light. Through this equation we can express the transverse fields in a waveguide $E_{\perp}$ and $B_{\perp}$ as a function of the longitudinal components E_z and B_z, that are independent of each other. From the boundary conditions given by eq. 2.1 and the fact that the longitudinal components are independent, we get that the solutions to eq. 2.2 form two sets of modes with different eigenvalues: the transverse magnetic modes (TM) and the transverse electric modes (TE). In the TM modes all the magnetic field components are perpendicular to the z axis, as shown in Fig. 2.2. In the case of a cylindrical pill-box

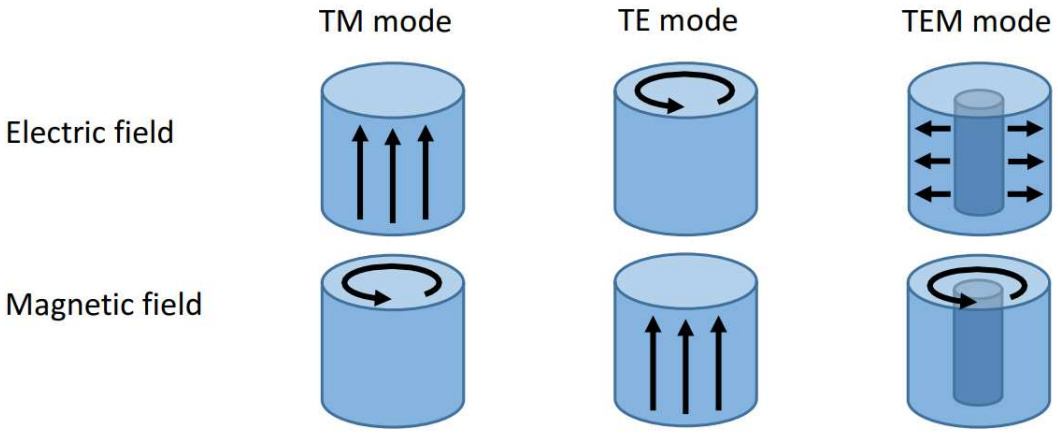

Figure 2.2: Visual representation of the fields inside the cavity for different modes types [40]

cavity of length d and radius R, similar to the cavities that are used in haloscopes, the fundamental TM_{010} mode is constituted of only the non vanishing components:

$$E_z = E_0 J_0\left(\frac{2.405\rho}{R}\right) e^{-i\omega t} \tag{2.3}$$

$$B_{\phi} = -i\frac{E_0}{c} J_1\left(\frac{2.405\rho}{R}\right) e^{-i\omega t} \tag{2.4}$$

where J_0 and J_1 are the zeroth- and first-order Bessel functions and 2.405 is the value of the first root of the zeroth [44].

A cavity can be characterized through several figures of merit, all mode-dependent. The losses are set by the surface resistance R_s, and defined as the power dissipated per unit area $\mathrm{d}P_c/\mathrm{d}s$ is:

$$\frac{\mathrm{d}P_c}{\mathrm{d}s} = \frac{1}{2\mu_0^2} R_s |\mathbf{B}|^2 \tag{2.5}$$

where μ_0 is the vacuum magnetic permeability.

Another figure of merit of importance to haloscopes is the quality factor Q_0 defined as

$$Q_0 = \frac{\omega_c U}{P_c} \tag{2.6}$$

where P_c is the power dissipated in the cavity walls, U and ω_c are respectively the electromagnetic energy stored in the cavity and the resonant frequency for the considered mode. Q_0 is 2π times the number of cavity cycles that a wave performs before the stored energy is fully dissipated. The stored energy is given by

$$U = \frac{1}{2\mu_0}\int_V |\mathbf{B}|^2 \mathrm{d}v = \frac{1}{2}\epsilon_0 \int_V |\mathbf{E}|^2 \mathrm{d}v \tag{2.7}$$

where ϵ_0 is the vacuum permittivity and the integral is performed over the volume of the cavity. By integrating over the cavity surface eq. 2.5 we obtain

$$P_c = \frac{1}{2\mu_0^2} R_s \int_S |\mathbf{H}|^2 \mathrm{d}s. \tag{2.8}$$

Thus we find for Q_0:

$$Q_0 = \frac{\omega_c \mu_0 \int_V |\mathbf{B}|^2 \mathrm{d}v}{R_s \int_S |\mathbf{H}|^2 \mathrm{d}s} = \frac{G}{R_s} = \frac{\omega_c}{\Delta\omega} \tag{2.9}$$

where the last two equalities are other useful definitions of the quality factor, with G the geometric constant and $\Delta\omega$ the bandwidth or the resonance transmission power spectrum.

Another crucial parameter for the haloscope is the form factor:

$$C = \frac{|\int_V \mathbf{B_0}\cdot\mathbf{E}|^2 \mathrm{d}v}{B_0^2 V \int_V \epsilon_0 |\mathbf{E}|^2 \mathrm{d}v} = \frac{|\int_V E_z|^2 \mathrm{d}v}{V \int_V \epsilon_0 |\mathbf{E}|^2 \mathrm{d}v} \tag{2.10}$$

where the integrals are performed over the cavity volume V and $\mathbf{B_0}$ is the applied magnetic field. The last equality holds when the field is directed parallel to the z axis as is the case for the majority of haloscopes [69]. C in an empty cylindrical cavity is different from zero only for TM_{0n0}, with its maximum value C_{010}. Notice that the product of form factor and volume is

$$C_{0n0} V = \frac{4\pi c^2 d}{\omega_n^2} \tag{2.11}$$

which scales inversely to the squared cavity frequency.

To read-out the cavity signal, the mode is connected via a transmission line to the receiver chain. The coaxial line is terminated by an antenna coupled to the cavity mode with coefficient β. The length of the antenna inserted inside the cavity determines β, and movable antennas allow for tuning the coupling. Total dissipated power includes also the power directed to the receiver chain P_r, so a loaded quality factor Q_L must be introduced:

$$\frac{1}{Q_L} = \frac{1}{Q_0} + \frac{1}{Q_r} \tag{2.12}$$

where Q_r is the external quality factor. The coupling parameter β is now defined as

$$\beta = \frac{P_r}{P_c} = \frac{Q_0}{Q_r}, \tag{2.13}$$

in terms of which

$$Q_L = \frac{Q_0}{1+\beta}. \tag{2.14}$$

Finally the signal power coupled to the receiver can be expressed as

$$P_r = P_{sig} = \omega_c \frac{U}{Q_r} = \frac{\beta}{1+\beta}\omega_c \frac{U}{Q_L}. \tag{2.15}$$

2.1.1 Signal power derivation

The cavity resonant frequency of a particular mode can be tuned by inserting conducting or dielectric rods inside the cavity with an automated mechanical system. In the first case the frequency is moved to higher frequencies while dielectric rods are able to diminish ω_c from the empty cavity one. A new technique to tune cavities by opening them in half on the length side is under exploration by the QUAX group and gave positive results in the last months. In practice also Q_L, β, and $C_{mn\ell}$ will vary throughout the tuning range posing some limits on the maximum tuning range explorable.

In the presence of an interaction with the axion field, Ampere and Gauss laws of the Maxwell's equations in the absence of electromagnetic sources, are modified into[63]:

$$\nabla \cdot \mathbf{E} = g_{a\gamma\gamma}\mathbf{B} \cdot \nabla a \tag{2.16}$$

$$\nabla \times \mathbf{B} - \partial_t \mathbf{E} = g_{a\gamma\gamma}(\mathbf{E} \times \nabla a - \mathbf{B}\partial_t a) \tag{2.17}$$

where a is the axion field and $g_{a\gamma\gamma}$ the axion-photon coupling. Recalling the largeness of the de Broglie wavelength λ_a terms in ∇a can be neglected, and assuming a spatially constant external field in the whole cavity volume we can replace $\mathbf{B}$ with $B_0\hat{z}$, where $\hat{z}$ is the z axis versor. Thus from all the new Maxwell's equation we obtain the inhomogeneus wave equation

$$\nabla^2 \mathbf{E} - \partial_t^2 \mathbf{E} = -g_{a\gamma\gamma} B_0 \partial_t a \hat{z} \tag{2.18}$$

By applying the cavity modes electric fields in this wave equation, the following formula for the energy stored U can be derived [14]:

$$U \propto g_{a\gamma\gamma}^2 \frac{\rho_a}{m_a^2} B_0^2 V C_{mn\ell} Q_L^2 \frac{1}{1 + (2Q_L \delta\omega_a/\omega_c)^2}. \tag{2.19}$$

where ρ_a is the axion density, m_a the axion mass and $\delta\omega_a = \omega_a - \omega_c$ is the detuning between the axion frequency and the cavity resonance frequency. Note the lorentzian dependence of the stored energy on the detuning.

If we insert eq. 2.19 into 2.15 we obtain the power signal produced by the interaction of an axion:

$$P_{sig} \propto g_{a\gamma\gamma}^2 \frac{\rho_a}{m_a^2} \frac{\beta}{1+\beta} \omega_c B_0^2 V C_{mn\ell} Q_L \frac{1}{1 + (2\delta\nu_a/\Delta\nu_c)^2} \tag{2.20}$$

where the cavity mode linewidth is $\Delta\nu_c = \nu_c/Q_L$ and $\nu_c = \omega_c/2\pi$. Notice that the signal is maximized for a cavity coupling parameter $\beta = 1$.

2.2 Microwave receiver and noise system temperature

The receiver chain amplifies the generated signal, that is digitized and processed using a discrete Fourier transform at room temperature and analyzed as a power spectrum as in the scheme Fig. 2.3.

The haloscope signal is a noise signal in any measurement of duration $\tau > \tau_a$, and the conversion power will be distributed over a finite bandwidth $\Delta\nu_a = 1/\tau_a = \nu_a/Q_a$. Therefore the presence of axions will manifest in narrowband incoherent electric field fluctuations, in principle indistinguishable from other noise in the same bandwidth. The noise signal of the axion has to go over the rest of the noise present in the system to be effectively detected. Thus the latter has to be minimized in designing the haloscope apparatus. The figure of merit that encodes the sensitivity of the measurements is the signal-to-noise ratio (SNR):

$$\mathrm{SNR} = \frac{P_{\mathrm{sig}}}{\delta P_N}, \tag{2.21}$$

where δP_N is the uncertainty in our estimate of the total noise power.

Johnson thermal noise [43] due to the power dissipated by the thermal motion of electrons in an imperfect conductor at finite temperature is always present. Several physical processes produce noise

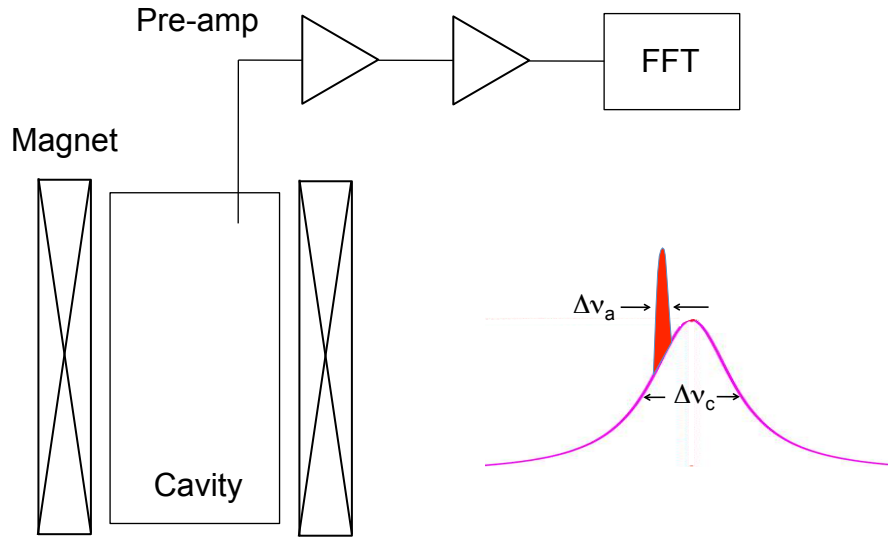

Figure 2.3: Haloscope scheme and expected signal spectrum (on the right). A cavity is inserted inside a solenoidal magnet and its electric field is coupled to the amplification chain through the insertion of an antenna. The amplified signal is analyzed with a fast Fourier transform to obtain its spectrum. The spectrum is expected to be composed of a gain curve relative to the cavity, of bandwidth $\Delta\nu_c$, with an over-imposed narrow peak, relative to the axion, of bandwidth $\Delta\nu_a$ [14].

indistinguishable from Johnson noise at some effective temperature. Thus we can express the total noise power present in a system in any bandwidth $\Delta\nu$ as Johnson noise in the form

$$P_N = k_B T_{sys} \Delta\nu, \tag{2.22}$$

with k_B the Boltzmann constant, and define an equivalent noise temperature of the system T_{sys}. The equivalent noise temperature of a cavity kept at thermodynamic temperature T_{cav} in the Rayleigh-Jeans limit $k_B T_{cav} \gg h\nu_{cav}$ can is precisely T_{cav} while in the Wien limit $k_B T_{cav} \ll h\nu_{cav}$ can be evaluated as [68]

$$T_{eqcav} = \frac{h\nu_{cav}}{2k_B} \coth\left(\frac{hf_{cav}}{2k_B T_{cav}}\right) \tag{2.23}$$

Moreover the equivalent noise temperature of a receiver chain, seen as a cascade of amplifiers, can be calculated as [54]

$$T_{syscascade} = T_1 + \frac{T_2}{G_1} + \frac{T_3}{G_1 G_2} + ... \tag{2.24}$$

where $T_{1,2,3}$ are the measured equivalent noise temperature of the various elements of the chain and $G_{1,2}$ are the gains relative to the chain elements. Notice that with high gains the noise temperature of the components after the first are greatly reduced and therefore $T_{syscascade}$ is mostly dependent on the first stage of amplification. Finally we can write the T_{sys} at the receiver input as equal to

$$T_{sys} = T_{noisecav} + T_{syscascade} \tag{2.25}$$

The expression for δP_N in an axion haloscope depends on the type of receiver coupled to the cavity. A coherent or linear receiver main characteristic is that its output is a linear function of the electric input field. Thus the Fourier component of the input signal will show up at the same frequency in the output signal, without limiting its frequency resolution. An incoherent or bolometric receiver presents an output signal proportional to the average intensity of the input, without preserving the phase information of the input signal, and its spectral resolution is limited by the receiver bandwidth. The haloscope setup of this thesis is based on a coherent amplifiers chain, so the following derivations will not consider the bolometric case.

Modeling the total noise power as Johnson noise, we can assume that the amplitude distribution of the noise voltage within a bandwidth $\Delta\nu$ is Gaussian [14][8]. Therefore, recalling the formula for the standard error of the variance of a Gaussian distribution, we obtain

$$\delta P_N = \sqrt{\frac{2}{n-1}} k_B T_{\rm sys} \Delta\nu, \tag{2.26}$$

where n is the number of independent samples, sufficiently large to approximate $n-1 \approx n$. Using in eq. (2.26) the Nyquist-Shannon sampling theorem[65], that states that noise limited to a bandwidth $\Delta\nu$ and measured for a time τ is completely represented by $n = 2\Delta\nu\tau$ independent samples, we obtain

$$\delta P_N = \frac{k_B T_{\rm sys} \Delta\nu}{\sqrt{\Delta\nu\tau}}, \tag{2.27}$$

which describes the uncertainty in the Johnson noise power in any bandwidth $\Delta\nu$. By assuming $\Delta\nu = \Delta\nu_a$, so that we capture the whole signal without adding more unnecessary noise, and inserting eq. (2.27) in eq. (2.21), we obtain the Dicke radiometer equation [25]

$$\mathrm{SNR} = \frac{P_{\rm sig}}{k_B T_{\rm sys}} \sqrt{\frac{\tau}{\Delta\nu_a}}. \tag{2.28}$$

Eq. (2.28) tells us the time τ required to detect or exclude axion conversion power P_{sig} at a sensitivity set by the SNR value, assuming to know T_{sys}. Since an SNR of ~ 1 is the minimum to see the signal, the usual requirement is at least $\sim 3-5$ [8].

2.3 Scan rate

The scan rate R determines the maximum speed at which the search can be conducted for a given SNR. We can derive its formula from eq. 2.28 by solving for t [69]

$$t = \mathrm{SNR}^2 \frac{k_B^2 T_{sys}^2}{P_{sig}^2} \Delta\nu_a \tag{2.29}$$

that is the time necessary for a measure at a given SNR Assuming that $Q_L < Q_a$, multiple signal bandwidth can be scanned simultaneously by the cavity. Their number is defined $N = Q_a/Q_L$. Therefore if we want to scan a frequency range $\Delta\nu$ it is necessary a scanning time

$$\Delta t = \frac{\Delta\nu}{N\Delta\nu_a} t. \tag{2.30}$$

By combining eq. 2.30 with eq. 2.29 and eq. 2.20 and rearranging we obtain the scan rate

$$\frac{\mathrm{d}\nu}{\mathrm{d}t} \propto \left(\frac{\rho_a^2 Q_a}{m_a^2}\right) \left(\frac{g_{a\gamma\gamma}^4}{\mathrm{SNR}^2}\right) \frac{B_0^4 Q_L (C_{mnl} V)^2}{(k_B T_{sys}^2}. \tag{2.31}$$

Notice that to double the sensitivity of the detector in the coupling parameter $g_{a\gamma\gamma}$ we need to reduce the scanning time of a factor 16. In particular for the purpose of this thesis the interesting dependence is

$$\frac{\mathrm{d}\nu}{\mathrm{d}t} \propto T_{sys}^{-2} \tag{2.32}$$

From the scan rate eq. 2.31 we see that the parameters on which we can operate to improve it are not few, being the magnetic field B_0, the cavity quality factor Q_L, the cavity form factor and volume $C_{mnl}V$ and the noise temperature T_{sys}. However there are some physical limitations to further improve the state of the art, specially if we want to reach higher signal frequencies [45].

We discussed in section 2.1 that the product $C_{mnl}V$ is limited by mode crossing when the volume is increased maintaining a fixed ν_c. Its dependence on the cavity frequency can be evaluated as $V \propto \nu^{-\zeta}$ with $\zeta \sim 2-3$.

Improvement on Q_0 are instead limited by the surface resistance due to the anomalous skin effect [50] [14] that poses a limit from above to the maximum cavity quality factor, for normal conducting cavities. This skin effect sets the dependence $Q_0 \propto \nu^{-2/3}$. SC cavities can reach much higher Q_0, as proven with particles accelerators, but it quickly degrades when a magnetic field is applied.

The $\mathrm{d}\nu/\mathrm{d}t \propto B_0^4$ dependence, although being promising, has not seen the hoped improvement in the last decades. High temperature SC magnets could be the turning point, being ideally able to reach fields $B \sim 20\,\mathrm{T}$, that would more than double the actual state of the art, but the research on this front is not that fast.

Taking in account the presented contributes, scan rate optimistically scales with frequency as $R \propto \nu^{-14/3}$, so a great effort is put on the improvement of the last parameter T_{sys}.

The noise temperature already improved a few hundredfold between 1987 and 2018 [45], owing it to two separate innovations: the use of colder thermal environments as the dilution refrigerators to house the haloscopes, and the continued improvement of amplifier technology, culminating in Josephson parametric amplifiers capable of reaching the standard quantum limit of noise, as we will see in the next section.

2.4 Cavity readout methods

A hundredfold improvement on the system noise temperature has been achieved during the last three decades [45], yet overcoming the standard quantum limit SQL of half a photon of noise, imposed by quantum mechanics uncertainty relation. The relative equivalent noise temperature to the SQL is calculated as

$$T_{\mathrm{SQL}} = \frac{1}{2}\frac{h\nu}{k_B} \tag{2.33}$$

In the following section the main cavity readout methods that helped achieve this milestone will be presented and future improvements that will further lower the system noise temperature T_{sys} will be discussed.

2.4.1 HEMT

In the field of usual transistor amplifier, the low bound on noise reduction is achieved through high electron mobility transistors (HEMTs), which will be further described in sec. 4.3.1. This is the first type of low noise amplifier utilized in axion detection and they allowed the exclusion of axion models with $|g_\gamma| \geq |g_\gamma^{\mathrm{KSVZ}}|$ and 700 MHz $\leq \nu_a \leq$ 800 MHz, with a $T_{add} \approx 2$ K, by the ADMX haloscopes [49]. In tab. 2.1 are presented the best commercial HEMTs based low noise amplifier produced by LNF, with the relative bandwidth, gain and noise temperature compared with the standard quantum limit at the central frequency of the bandwidth. The noise levels vary for different ranges, as also does the SQL, maintaining for most of the bandwidths a ratio between $T_{add}/T_{\mathrm{SQL}} \sim 10$. Therefore at the present day they are not recommended as first stage haloscopes amplifier, due to the existence of less noisy solutions, but are suitable components for second part of the amplification chain. DC SQUID superconducting amplifiers should also be mentioned as a step in the noise improvement, implemented in the ADMX haloscope after HEMTs [2], but their added noise is still distant from the SQL.

2.4.2 Parametric amplifiers: standard quantum limit and beyond

Even lower noise than HEMTs and DC SQUIDs can be achieved through parametric amplification in superconductors based amplifiers. In particular Josephson parametric amplifiers (JPA), further discussed in chapter 3, are able to reach the SQL of added noise.

Any classical narrowband ($\Delta\nu_c \ll \nu_c$) voltage signal may be written in the two equivalent forms [14]

$$V(t) = V_0\Big[I(t)\cos(2\pi\nu_c t) + Q(t)\sin(2\pi\nu_c t)\Big] \tag{2.34}$$

$$= \frac{V_0}{2}\Big[a(t)e^{-2\pi i\nu_c t} + a^*(t)e^{2\pi i\nu_c t}\Big] \tag{2.35}$$

model	bandwidth (GHz)	T_{add} (K)	gain (dB)	T_{rmSQL} (K)	T_{add}/T_{SQL}
LNF-LNC0.6_2A	0.6-2	1.5	30	0.03	48.08
LNF-LNC2_4A	2-4	1.3	34	0.07	18.06
LNF-LNC4_8F	4-8	1.5	44	0.14	10.42
LNF-LNC4_16C	4-16	3.1	36	0.24	12.92
LNF-LNC6_20D	6-20	3.8	32	0.31	12.18
LNF-LNC15_29B	15-29	7	28	0.53	13.26
LNF-LNC23_42WB	23-42	7.5	28	0.78	9.62
LNF-LNC28_52WB	28-52	10.5	36	0.96	10.94
LNF-LNC45_77WA	45-77	13	33	1.46	8.88
LNF-LNC65_115W	65-115	24	23	2.16	11.11

Table 2.1: Specifics of the best commercially available HEMT amplifier, sorted by bandwidth

where I and Q are the signal quadratures. In the case of the haloscope, $V(t)$ is the voltage on the antenna at the receiver input, which is proportional to the electric field of the cavity mode of interest. Electromagnetic fields are considered to be coherent light comprising photons, thus they can be quantized by promoting a and a^* to operators $\hat{a}$ and $\hat{a}^\dagger$ with the commutation relation $[\hat{a}, \hat{a}^\dagger] = 1$.

In a linear, phase-insensitive amplifier, an input state $\langle a_{in} \rangle$ is amplified to an output state $\langle a_{out} \rangle$, with an amplitude gain $\sqrt{G}$. Their operators must obey the commutation relations [61]

$$[\hat{a}_{in}, \hat{a}_{in}^\dagger] = [\hat{a}_{out}, \hat{a}_{out}^\dagger] = 1, \tag{2.36}$$

from which it can be shown that it is not possible to simultaneously amplify both quadratures of $\hat{a}_{in}$ without also adding noise, the so-called Haus-Caves theorem [32, 17]. The gain relation [36]

$$\hat{a}_{out} = \sqrt{G}\hat{a}_{in}. \tag{2.37}$$

constitutes the ideal scenario for an amplifier process. However, this relation does not satisfy the commutation relation in eq. 2.36. The solution to this problem is to take into account the vacuum fluctuations of another mode, called the idler mode $\hat{a}_{in}$, also obeying $[\hat{b}_{in}, \hat{b}_{in}^\dagger] = 1$. To satisfy the commutation relation, the idler mode is amplified by the gain factor $\sqrt{G-1}$. It can be shown that, for large gain, half a photon of noise $h\nu/2$ is added to a signal amplified with gain $\sqrt{G}$, that is the SQL for amplifiers added noise. Thus the correct relation between input and output fields takes the form

$$\hat{a}_{out} = \underbrace{\sqrt{G}\hat{a}_{in}}_{Amplification} + \underbrace{\sqrt{G-1}\hat{b}_{in}^\dagger}_{Added\,idler\,noise}. \tag{2.38}$$

When both quadratures of the input field gets equally amplified, this process takes the name of phase-insensitive parametric amplification. This is illustrated in Fig. 2.4, where the in-phase ($\hat{I}_{in}$) and quadrature ($\hat{I}_{in}$) components of the fields are plotted, before and after the parametric amplifier.

In a special case the amplification process in eq. 2.38, can be accomplished noiselessly for one of the two quadratures, but at the expense of adding more noise to the other. In this way it does not violate Heisenberg's uncertainty relation for the two field quadratures. This is known as phase-sensitive amplification, and is obtained when the idler and the signal modes oscillate at the same frequency, but the idler phase can be shifted. By substituting the idler mode in Eq. (2.38) with $\hat{b}_{in} = e^{i\phi}\hat{a}_{in}$, we get

$$\hat{a}_{out} = \underbrace{\sqrt{G}\hat{a}_{in}}_{Amplification} + \underbrace{e^{-i\phi}\sqrt{G-1}\hat{a}_{in}^\dagger}_{Phase-dep.\,noise}. \tag{2.39}$$

The overall phase factor allows us to tune the orientation of the amplification, and de-amplification, by operating on the pump phase, thus reducing the noise on the wanted quadrature, see Fig. 2.5. In this way the noise can be suppressed even below the standard quantum limit. This is known as single-mode squeezing.

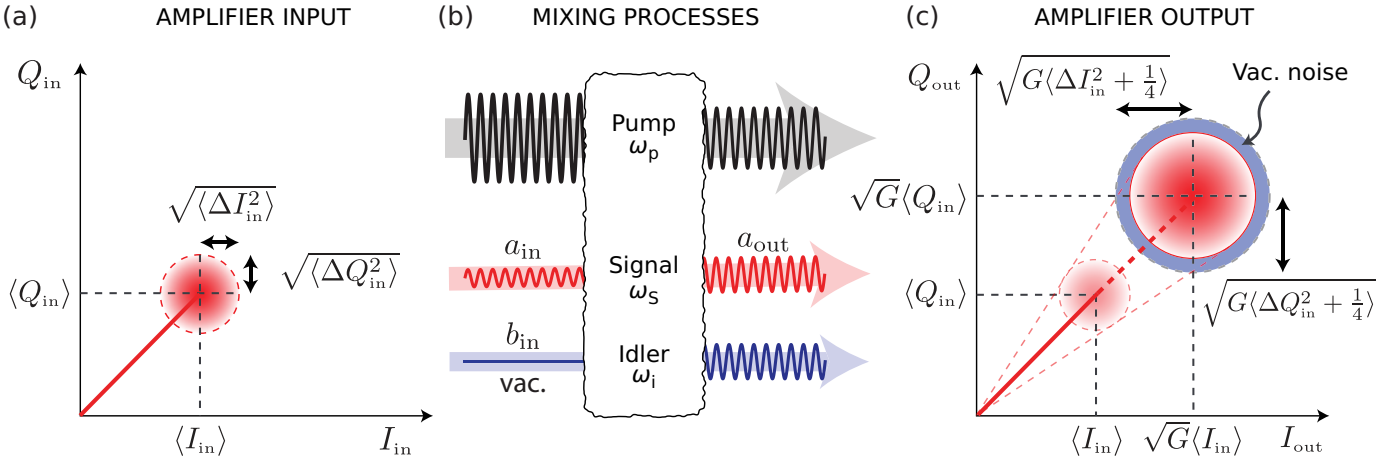

Figure 2.4: Schematic illustration of a quantum-limited, phase-preserving parametric amplification process of a coherent input state, $\hat{a}_{in} = \hat{I}_{in} + i\hat{I}_{in}$. (a) The state is centered at $(\langle I_{in}\rangle, \langle Q_{in}\rangle)$ and has a noise represented by the radii of the circles along the real and imaginary axes, respectively. (b) Scattering representation of parametric mixing, where the signal and pump photons are interacting via a purely dispersive nonlinear medium. (c) In the case of phase-preserving amplification, both quadratures get amplified by a factor $\sqrt{G}$, while (in the ideal case) half a photon of noise gets added to the output distribution (blue). [36]

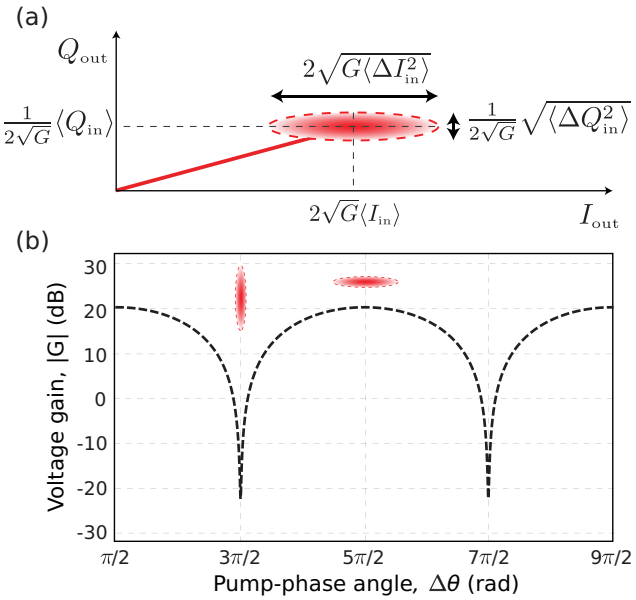

Figure 2.5: Phase-sensitive parametric amplification. **(a)** In contrast to the phase-insensitive operation, phase-sensitive parametric amplification allows us to suppress the noise along one axis. Consequently, the noise is added to the other quadrature. **(b)** Voltage gain as a function of pump-phase angle, in which the amplification depends on the phase of the pump, providing either amplification or de-amplification of the quadrature voltage [36].

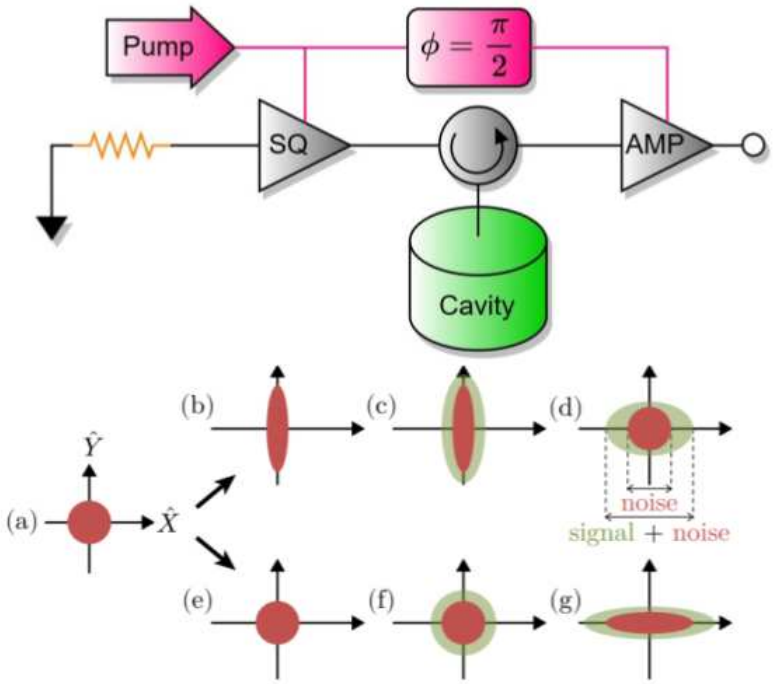

Figure 2.6: The upper figure represents the squeezed state receiver scheme at the HAYSTAC haloscope: SQ parametric amplifier prepares a squeezed vacuum state on the X quadrature for the cavity, that is later amplified by AMP on the Y quadrature. A phase difference of $\pi/2$ is maintained between the pump signals of the two parametric amplifiers. The lower picture represents the measure of the cavity vacuum noise (a) in the presence of SQ (b, c, d) and in its absence (e, f, g). If an axion signal is produced inside the cavity, in the first case, with a squeezed vacuum, obtains an higher SNR than in the second case, with a simple phase-sensitive amplification [21].

The squeezed state receiver

Single-mode squeezing was effectively implemented in an haloscope by the HAYSTAC experiment [6]. With the use of two JPA, positioned in the circuit line respectively before and after the cavity by mounting a three port circulator they achieved a final scan rate improvement of a factor 2. In this technique, see upper part of Fig. 2.6, a $50\,\Omega$ resistor generates thermal noise that is squeezed on one quadrature by the first JPA and fed to the cavity. The exiting signal will contain both squeezed noise and cavity noise, in which may be contained the axion signal, and is further amplifiedby the second JPA, that is pumped with a phase difference from the first JPA of $\pi/2$. In this way the signal will be squeezed on the other quadrature and measured, with a smaller noise than in the case with no squeezed vacuum, see lower part of Fig. 2.6. Thus near-noiseless amplification is obtained.

2.4.3 Single-photon counters

Bolometric amplifiers as single-photon counters, behave differently from linear amplifiers, as we already discussed in section 2.2. In particular they don't suffer of the low bound on noise reduction imposed by the SQL, as explained in the following. Considering the commutation relations introduced in section 2.4.2, the Hamiltonian for a haloscope cavity mode results that of quantum harmonic oscillator (QHO): $\hat{H} = h\nu_c\big(\hat{N} + 1/2\big)$ with $\hat{N} = \hat{a}^\dagger\hat{a}$ the photon number operator. For the equivalence of Eqs. 2.35 and 2.34, this Hamiltonian can also be written in function of the quadratures:

$$\hat{H} = \frac{h\nu_c}{2}\big(\hat{I}^2 + \hat{Q}^2\big), \tag{2.40}$$

with $[\hat{I}, \hat{Q}] = i$. A linear receiver measures the quadrature amplitudes $\hat{I}$ and/or $\hat{Q}$, whereas a bolometric receiver measures $\hat{N}$. Thus the unavoidable quantum added noise in coherent amplifiers arises

because neither of the quadratures commutes with the Hamiltonian. Conversely bolometric single-photon amplifiers can evade the SQL because their measure commutes with the QHO Hamiltonian, $[\hat{H}, \hat{N}] = 0$. This type of measurements are called quantum non-demolition measurement (QND) or back-action evading measurement (BAE), in the first case because the measured degree of freedom commutes with the Hamiltonian, in the second because the a first measurement doesn't increase the uncertainty of a second one [8].

To understand in which conditions the QND property of single-photon counters significantly improves the noise in the system with respect to that of a linear amplifier, we can compare their noise power. Considering a low temperature environment, linear amplifier noise power eq. 2.27 becomes

$$P_\ell = h\nu(\bar{n}+1)\sqrt{\frac{\Delta\nu_a}{t}} \tag{2.41}$$

where $\bar{n} = 1/(\exp(\hbar\omega/k_BT) - 1)$ is the Bose Einstein distribution and t is observation time. In this way we consider the zero-point fluctuation contribute.

For photon-counting experiments the primary source of noise is shot noise on the detected thermal photons. Given a detection efficiency η the rate of photon detection is [38]

$$\dot{n} = \eta\Gamma\bar{n} \tag{2.42}$$

where $\Gamma = 1/\tau_c$ is the loaded cavity lifetime.

In an observation time t, N photons, associated with both the axion and the thermal excitations, are detected, where

$$N = \dot{n}t = \eta\bar{n}\Gamma t \tag{2.43}$$

which has fluctuations due to counting poissonian statistics of

$$\delta N = \sqrt{N} = \sqrt{\eta\bar{n}\Gamma t}. \tag{2.44}$$

Assuming only thermal photons, we can derive an equivalent photon counting noise power,

$$P_{sp} = \frac{h\nu\delta N}{t} = h\nu\sqrt{\frac{\eta\bar{n}\Gamma}{t}}. \tag{2.45}$$

Comparing the noise powers of the two methods, eqs. 2.41 and 2.45 we get

$$\frac{P_\ell}{P_{sp}} = \frac{\bar{n}+1}{\sqrt{\bar{n}}}\sqrt{\frac{\Delta\nu_a}{\eta\Gamma}}. \tag{2.46}$$

We can cast this relation in a simpler and more expositive form noting that $\Gamma = 2\pi\nu/Q_c$ and $\Delta\nu_a \approx \nu/Q_a$. Therefore, in terms of the thermal photon occupation number, Q_a, and Q_c,

$$\frac{P_\ell}{P_{sp}} = \left[\sqrt{\bar{n}} + \frac{1}{\sqrt{\bar{n}}}\right]\sqrt{\frac{Q_c}{2\pi\eta Q_a}}. \tag{2.47}$$

We see that moving to higher frequencies in the axion parameter space and decreasing the cavity and detector temperature creates more and more favorable condition to prefer a single-photon counter to a linear amplifier. As a prove, for a temperature $T = 10\,\mathrm{mK}$, achieved also in the experiment presented in this thesis, a frequency $\nu = 10.4\,\mathrm{GHz}$ and $Q_a/Q_c \sim 25$, as for our experimental cavity, the photon population is $\bar{n} \approx 2 \times 10^{-22}$ we obtain (with $\eta \approx 1$)

$$\frac{P_\ell}{P_{sp}} \approx \left(\frac{1}{1.5\times10^{-11}} + 1.5\times10^{-11}\right) \times \frac{1}{12.5} \approx 5.5\times10^{9} \tag{2.48}$$

Notice that this extremely positive result is considering an ideal case in which the efficiency is maximum and there are no dark counts in the detected photons. Considering also these limitation, the noise improvement decreases, but will be significant, especially at even higher frequencies.

The proposed implementations of single-photon counters in haloscope involve Rydberg atoms and SC qubits.

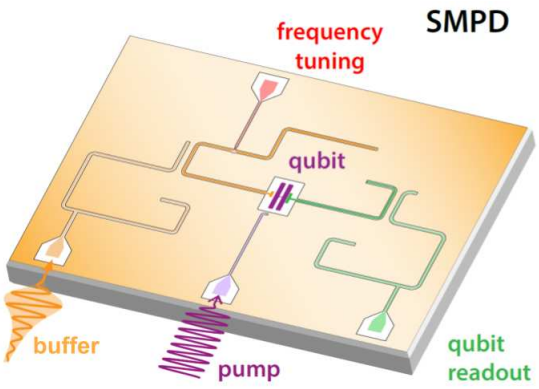

Figure 2.7: The SMPD, a SC circuit with $\lambda/2$ coplanar waveguide resonators linked to a transmon qubit. Its frequency is adjustable by threading the flux through a SQUID embedded in the buffer resonator. Upon activating the four-wave mixing process, the qubit cycles through photon detection phases. [12].

Rydberg atoms

Rydberg atoms detection technique was first proposed in the 90s by the CARRACK experiment that measured an added noise $T_{add} = 67\,\text{mK}$ at 2.527 GHz, a factor of two below the SQL noise temperature [71], but was never implemented on an effective haloscope. A new proposal on a Rydberg-atom-based single-photon detector for signal readout between 10 GHz and 50 GHz has been lately made by the HAYSTAK experiment, with a promising scan rate enhancement of a factor 10^4 [30].

Superconducting qubits

The coupling between a SC qubit and a resonator in the so-called dispersive regime is a good example of QND measurement. The qubit-resonator interaction is described by the Jaynes-Cummings Hamiltonian[36]

$$H_{JC} = \omega_r \left(a^\dagger a + \frac{1}{2}\right) + \frac{\omega_q}{2}\sigma_z + g\left(\sigma_+ a + \sigma_- a^\dagger\right), \tag{2.49}$$

where ω_r and ω_q are respectively the resonator and qubit frequencies and g is the qubit-resonator coupling rate. The operators σ_+ and σ_- represent respectively the processes of exciting and de-exciting the qubit. In the limit when the detuning between the qubit and the resonator is small compared with their coupling rate, i.e. $\Delta = |\omega_q - \omega_r| \ll g$, energy is directly exchanged between the two systems, thus changing the qubit state. In the dispersive limit, when the qubit is far detuned from the resonator compared with g and the resonator linewidth κ, $\Delta \gg g, \kappa$, there is no longer a direct exchange of energy between the two systems. Instead, the qubit and resonator push each others' frequencies. The Hamiltonian can be approximated, with the so called dispersive approximation, in the limit of few photons in the resonator, taking the form

$$H_{\text{disp}} = \left(\omega_r + \chi\sigma_z\right)\left(a^\dagger a + \frac{1}{2}\right) + \frac{\widetilde{\omega}_q}{2}\sigma_z, \tag{2.50}$$

where $\chi = g^2/\Delta$ is the qubit-state dependent frequency shift, that allows us to distinguish the two qubit states by interrogating the resonator.

This technique is fundamental for the single microwave photon detector (SMPD), a type of photon counter that was lately implemented in a haloscope in the QUAX experiment [12], obtaining a scan rate enhancement of a factor 20.

The SMPD is a SC circuit, depicted in Fig. 2.7 with a transmon qubit coupled to two resonators: a 'buffer' resonator whose frequency ω_b can be tuned to the incoming photon frequency, and a 'waste' resonator with fixed frequency ω_w. A four-wave-mixing (4WM) process activated by a pump pulse at frequency ω_p converts with close to unit efficiency an itinerant photon entering the buffer resonator into a qubit excitation ω_q and a waste photon. The energy conservation implies that $\omega_p + \omega_b = \omega_q + \omega_w$.

The waste resonator quickly damps its converted photon in the environment ensuring the irreversibility of the 4WM process and forcing the qubit to remain in its excited state, which is then measured using the dispersive readout method. To achieve axion measurements, the buffer is connected to the 3D resonator in which the Primakoff effect takes place.

Chapter 3

The Josephson Parametric Amplifier

The concepts of parametric amplification and frequency conversion apply to a rather broad range of electronic, optical and mechanical systems. In fact, any system that can periodically convert energy between conjugate field variables as, for instance, voltage and current, electric and magnetic fields, or momentum and position, can produce some sort of parametric behavior if the corresponding mediating elements can be modulated. Circuit reactances, spring constants, and indices of refraction are examples of elements that are modulated in the systems. ([3])

3.1 Parametric amplification in optics

In quantum optics a parametric interaction is defined as a process that takes place in a nonlinear medium, where electromagnetic waves of different frequencies can mix and generate new frequencies. A well-known parametric interaction is the spontaneous parametric down conversion (SPDC), which leads to entangled photons generation [16]. SPDC happens when an intense electromagnetic wave of frequency $\omega_p/2\pi$, called pump, is sent towards a nonlinear medium and generates two electromagnetic waves, called signal (idler) of frequency $\omega_s/2\pi$ ($\omega_i/2\pi$) such that energy is conserved. The 'signal' wave generally carries the frequency of interest. When dealing with parametric amplification, the spontaneous character of SPDC in the emission is replaced by a stimulated emission when the pump and the signal are simultaneously sent to the nonlinear medium, producing the so-called "Difference-Frequency Generation" (DFG). ([11])

Considering the second-order nonlinear polarization of a non-linear medium with ϵ_0 the dielectric constant and $\chi^{(2)}$ the second order susceptibility

$$P^{(2)}(t) = \epsilon_0 \chi^{(2)} E(t)^2. \tag{3.1}$$

By applying the pump and signal field

$$E(t) = E_p e^{-i\omega_p t} + E_s e^{-i\omega_s t} + c.c. \tag{3.2}$$

with c.c. standing for complex conjugates, we obtain

$$\begin{aligned} P^{(2)}(t) = \quad & \epsilon_0 \chi^{(2)} \left[E_p^2 e^{-2i\omega_p t} + E_s^2 e^{-2i\omega_s t} + 2E_p E_s e^{-i(\omega_p+\omega_s)t} + 2E_p E_s^* e^{-i(\omega_p-\omega_s)t} + c.c. \right] \\ & + 2\epsilon_0 \chi^{(2)} \left[E_p E_p^* + E_s E_s^* \right]. \end{aligned} \tag{3.3}$$

If the non-linear material hosted in a resonator, that supports modes with angular frequencies ω_s and $\omega_i = \omega_p - \omega_s$, only the DFG process is allowed:

$$P(\omega_i = \omega_p - \omega_s) = 2\epsilon_0 \chi^{(2)} E_p E_s^* \tag{3.4}$$

As depicted in Fig. 3.1, each pump photon generates a signal and an idler photon $\omega_p = \omega_s + \omega_i$ in a so-called Three Way Mixing (3WM) process, that can also be exploited for amplification. A Four Wave Mixing (4WM) is instead based on higher order non-linearities, as in the Kerr effect, in which two pump photons convert to signal and idler photons with the relation $2\omega_p = \omega_s + \omega_i$.

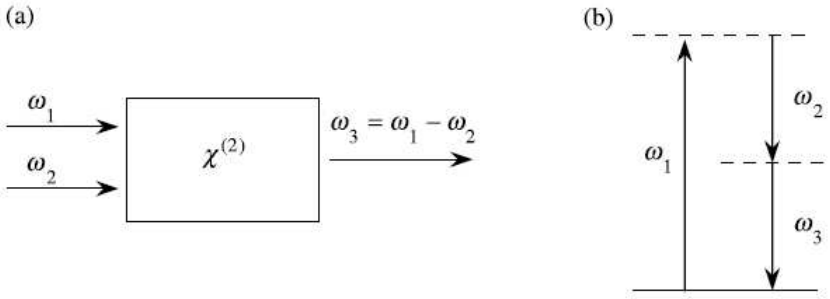

Figure 3.1: (a) Difference frequency generation optical scheme: two photons of different frequency ω_1 and ω_2 enter the non-linear crystal and a third photon of frequency $\omega_3 = \omega_1 - \omega_2$ is emitted. (b) energy level representation of DFG [11].

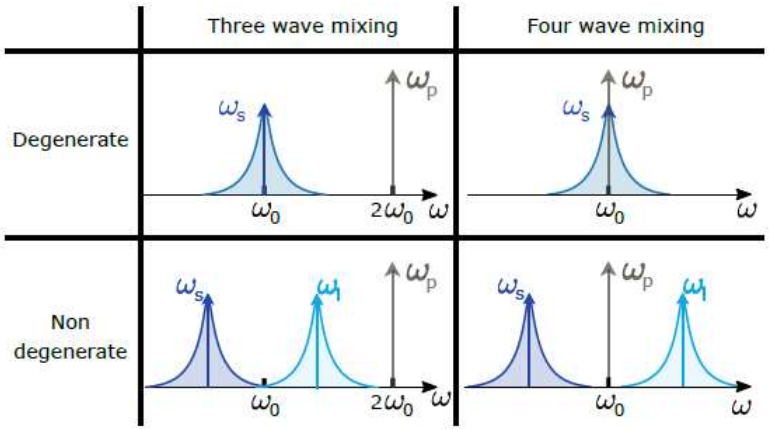

Figure 3.2: Comparison between 4WM and 3WM in degenerate and non degenerate cases from [51]: in the case of degenerate 3WM the signal ω_s is amplified by a pump of frequency $\omega_p = 2\omega_s$; in degenerate 4WM pump and signal have the same frequency $\omega_s = \omega_p$; for non degenerate 3WM the pump needs to be set at the sum of signal and idler frequencies $\omega_p = \omega_s + \omega_i$ while for the relative 4WM we have $\omega_p = \omega_i - \omega_s$.

The key requirement to accomplish parametric amplification in an optical medium is that the refractive index n depends on the wave amplitude. The pump modulates n over time and therefore induces a periodic modulation of the wave velocity. In this sense, n becomes a time-varying parameter of the equation describing wave propagation, hence the name parametric. This leads to energy transfer between the pump and the signal, giving rise to gain. To maximize the stimulated signal emission, the interaction time between the pump, the signal in the nonlinear medium must be increased. To do so, it is common to put the nonlinear medium in an optical resonator, giving rise to a nonlinear resonator (NLR) with the resonant frequency $\omega_0/2$ as shown in Fig. 3.2.

Parametric amplification is said to be non-degenerate if the idler wave evolves in a spatially separated mode from that of the signal. Otherwise, if signal and idler evolve in the same spatial mode, the amplifier is said to be degenerate. ([51]) Note that a degenerate parametric amplification with the same frequency for signal and idler is a phase-sensitive process, as the amplifier gain is sensitive to the phase difference between the pump and the signal, as detailed in Chapter 2.

3.1.1 3WM in quantum optics

As the amplifier characterized in this thesis is based on a non-degenerate 3WM process, here we analyze its ideal behaviour through the quantum optics formalism.

To study the intra-resonator fields dynamics, we start by introducing the Hamiltonian of the system H_{sys}:

$$\hat{H}_{sys} = \sum \hat{H}_{res} + \hat{H}_{int} \tag{3.5}$$

where $\hat{H}_{res}$ is the NLRs Hamiltonian and $\hat{H}_{int}$ accounts for the interactions between NLRs fields.

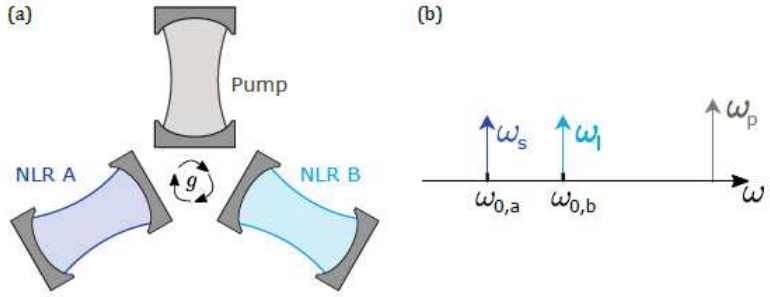

Figure 3.3: Three wave mixing non-degenerate process. (a) Two nonlinear resonators (NLR A and NLR B) and the pump oscillator are coupled with rate g (*chi* in the text). They have a specific engineered interaction, modeled with the Hamiltonian H_{int}. (b) Signal amplification occurs when its frequency $\omega_s/2\pi$ is close to NLR A resonant frequency $\omega_{0,a}$ and fulfills energy conservation $\omega_s = \omega_p - \omega_i$. In this scheme, signal and idler amplifications are also spatially separated [51].

In the case of non-degenerate 3WM, three different oscillators, denoted in Fig 3.3 as NLR A, B and C, are coupled with coupling χ. Their fields position and momentum operator are defined as:

$$\hat{X}_j = x_j^{zpf}\left(\hat{j} + \hat{j}^\dagger\right) \ , \ \hat{Y}_j = -iy_j^{zpf}\left(\hat{j} - \hat{j}^\dagger\right) \ with \ j = \{a, b, c\} \tag{3.6}$$

with i the imaginary unit, x_j^{zpf} and y_j^{zpf} the respective zero point fluctuation and $\hat{j}^\dagger$ and $\hat{j}$ the creation and annihilation operators of the fields. The 3WM Hamiltonian therefore takes the form:

$$\hat{H}_{3\mathrm{WM}} = \hbar\omega_{0,a}\hat{a}^\dagger\hat{a} + \hbar\omega_{0,b}\hat{b}^\dagger\hat{b} + \hbar\omega_{0,c}\hat{c}^\dagger\hat{c} + \hbar\chi\left(\hat{a} + \hat{a}^\dagger\right)\left(\hat{b} + \hat{b}^\dagger\right)\left(\hat{c} + \hat{c}^\dagger\right) \tag{3.7}$$

If one replaces the field c with a far off-resonance pump field p, a parametric interaction between fields a and b is induced by the pump. In order to modulate n of the medium the nonlinear resonator must be driven by an intense pump field. Therefore for its large amplitude, the pump is modeled as a classical drive with:

$$X_p = x_p\left(p + p^*\right) \ , \ Y_p = -iy_p\left(p - p^*\right) \tag{3.8}$$

where x_p and y_p are the dimensionless amplitudes of position and momentum. With these assumptions on the pump field, the 3WM Hamiltonian becomes:

$$\hat{H}_{3\mathrm{WM}} = \hbar\omega_{0,a}\hat{a}^\dagger\hat{a} + \hbar\omega_{0,b}\hat{b}^\dagger\hat{b} + \hbar\chi\left(\hat{a} + \hat{a}^\dagger\right)\left(\hat{b} + \hat{b}^\dagger\right)\left(p + p^*\right) \tag{3.9}$$

To obtain amplification the pump must be driven at the sum of the other two signals frequencies $\omega_p = \omega_a + \omega_b$. At this point by applying the rotating wave approximation RWA, whereby only slow fields in the rotating frame of interest are considered while the others are discarded, the Hamiltonian reduces to

$$\hat{H}_{3\mathrm{WM}} = \hbar\omega_{0,a}\hat{a}^\dagger\hat{a} + \hbar\omega_{0,b}\hat{b}^\dagger\hat{b} + \hbar\chi\left(p\hat{a}^\dagger\hat{b}^\dagger + p^*\hat{a}\hat{b}\right) \tag{3.10}$$

with the last term representing the non-degenerate amplification.

To further study the fields behaviour we introduce the Quantum Langevin Equation (QLE) which describes, in the Heisenberg picture, the intra-resonator fields ($\hat{a}$ and $\hat{b}$) evolution of a resonator coupled to a reservoir of propagating modes (($\hat{a}_{in,out}$ and $\hat{b}_{in,out}$) ([27]). Under the Markov approximation, whereby the system itself does not affect the reservoirs from which the fields are coming ([73]), and the RWA, the QLE for signal $\hat{a(t)}$ and idler $\hat{b(t)}$ read

$$\begin{cases} \frac{\partial \hat{a}}{\partial t} = \frac{i}{\hbar}\left[H_{3\mathrm{WM}}, \hat{a}\right] - \frac{\kappa_a}{2}\hat{a} + \sqrt{\kappa_a}\hat{a}_{in} \\ \frac{\partial \hat{b}}{\partial t} = \frac{i}{\hbar}\left[H_{3\mathrm{WM}}, \hat{b}\right] - \frac{\kappa_b}{2}\hat{b} + \sqrt{\kappa_b}\hat{b}_{in} \end{cases} \tag{3.11}$$

where $\kappa_{a,b}$ are the NLR coupling rates with the external fields. The two equations are coupled linearly by the amplification Hamiltonian

$$\begin{cases} \frac{\partial \hat{a}}{\partial t} = -i\omega_{0,a}\hat{a} - i\chi p\hat{b}^\dagger - \frac{\kappa_a}{2}\hat{a} + \sqrt{\kappa_a}\hat{a}_{in} \\ \frac{\partial \hat{b}}{\partial t} = -i\omega_{0,b}\hat{b} - i\chi p\hat{a}^\dagger - \frac{\kappa_b}{2}\hat{b} + \sqrt{\kappa_b}\hat{b}_{in} \end{cases} \tag{3.12}$$

where $\omega_{0,"a,b"}$ are the resonance frequencies of the NLRs.

If we consider the case where the amplification occurs in reflection, we take the boundary conditions

$$\begin{cases} \sqrt{\kappa_a}\hat{a}[\omega_a] = \hat{a}_{out}[\omega_a] + \hat{a}_{in}[\omega_a] \\ \sqrt{\kappa_b}\hat{b}[\omega_b] = \hat{b}_{out}[\omega_b] + \hat{b}_{in}[\omega_b] \end{cases} \tag{3.13}$$

with $\omega_{a,b}$ the frequencies of the modes

From these equations, in the large gain limit, we can obtain the important relation between the actual maximum power gain $G_{max} = \hat{a}_{out}/\hat{a}_{in}$ delivered by the amplifier and its dynamic bandwidth ΔBW, in general defined as the -3 dB bandwidth or Full Width at Half Maximum (FWHM).

$$\sqrt{G_{max}} \times \Delta\mathrm{BW} = \frac{2}{\left(\frac{1}{\kappa_a} + \frac{1}{\kappa_b}\right)} = \text{const.} \tag{3.14}$$

As we can see, the product between G_{max} and ΔBW is thus conserved. In practice, the higher the gain, the smaller the bandwidth. This can be understood in terms of interaction time between the signal and the nonlinear medium inside the resonator: to have a higher gain the interaction time must increase, and so its instantaneous bandwidth decreases.

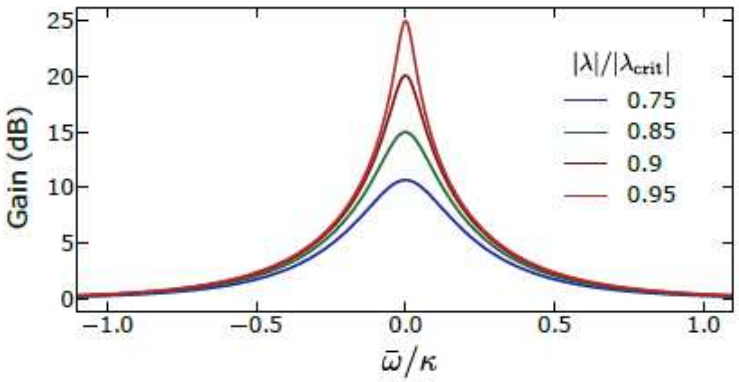

Figure 3.4: Signal power gain vs reduced detuning $\bar{\omega}/\kappa$ between the pump and the signal frequency. We display the gain for different pump strength λ. κ is the amplification bandwidth while λ_{crit} is the maximum pump strength over which no more improvement on the maximum gain are obtained [51].

3.2 Basic concepts in circuit Quantum Electrodynamics

We're concerned with parametric amplification in electronic circuits working in the microwave range. The measurement of signals of the order of few to even a single photon requires the first stage of the detection to be performed in an ultracryogenic, dissipationless regime, thus adding minimal noise in the amplification process The background needed to understand the working principle of the devices tested in the present thesis is that of circuit quantum electrodynamics (cQED), in which the study and control of light-matter interaction at the quantum level is devised. In this context we model lumped LC resonators as quantum harmonic oscillators (QHO) in section 3.2.1, we introduce the Josephson

Junction as the dissipationless, non-linear element to accomplish parametric amplification in section 3.2.2, and finally discuss its application as a tunable inductance through an external flux in the DC SQUID in section 3.2.3. This latter concept is at the basis of the Josephson Parametric Amplifier (JPA).

3.2.1 The quantum harmonic oscillator

The electromagnetic energy stored in an LC resonator oscillates between the electrostatic energy in the capacitor C, associated to the charge Q present on its plates, and the magnetic energy in the inductance L, related to the magnetic flux Φ in the coil. Therefore the total energy of the system can be expressed as ([36])

$$H = \frac{Q^2}{2C} - \frac{\Phi^2}{2L} = \frac{1}{2}CV^2 + \frac{1}{2}LI^2 \tag{3.15}$$

Note that this Hamiltonian is analogous to the one of a mechanical oscillator of coordinate Φ, conjugate momentum Q and mass C. With this analogy in mind, the two conjugate variables of charge and flux are promoted to quantum operators satisfying the commutation relation

$$\left[\hat{\Phi}, \hat{Q}\right] = \hat{\Phi}\hat{Q} - \hat{Q}\hat{\Phi} = i\hbar \tag{3.16}$$

and the two variables are expressed in terms of ladder operators:

$$\hat{\Phi} = \sqrt{\frac{\hbar}{2\omega_0 C}}\left(\hat{a} + \hat{a}^\dagger\right) \tag{3.17}$$

$$\hat{Q} = -i\sqrt{\frac{\hbar\omega_0 C}{2}}\left(\hat{a} - \hat{a}^\dagger\right) \tag{3.18}$$

with $\omega_0 = 1/\sqrt{LC}$ the angular frequency of the resonator. We thus get the canonical Hamiltonian of the QHO [61]:

$$H = \hbar\omega_0\left(\hat{a}^\dagger\hat{a} + 1/2\right) \tag{3.19}$$

The Hamiltonian given in eq. 3.15 can be written in terms of reduced flux $\phi \equiv \Phi/\phi_0$, with $\phi_0 = \hbar/(2e)$ the reduced magnetic flux quantum, and reduced charge $n \equiv Q/2e$, as

$$H = 4E_C n^2 + \frac{1}{2}E_L\phi^2 \tag{3.20}$$

where $E_C = e^2/(2C)$ is the charging energy and $E_L = (\Phi_0/2\pi)^2/L$ is the inductive energy ([36]). With these new definitions we have $\omega_0 = \sqrt{8E_L E_C}/\hbar$.

3.2.2 The Josephson Junction

The previously described concept of optical parametric amplification can be transferred in the context of cQED provided a non-linear element like the SC Josephson Junction (JJ) is introduced in the LC circuit. This element satisfies the cQED requirements, as it is a dissipationless component. As first theorized by Brian Josephson in 1962 ([35]), when two superconductors are separated by a thin insulating layer, a supercurrent I of tunneling Cooper pairs is can flow across the junction, even without a voltage applied between the two leads. The intensity of this current depends on the phase difference ϕ between the macroscopic wave functions on either sides of the junction:

$$I = I_c \sin\phi \tag{3.21}$$

where I_c is the critical current, that is the maximum supercurrent that is supported before a resistive current sets in.

In his work, Josephson also showed that the time derivative of ϕ is related to the voltage across the junction according to

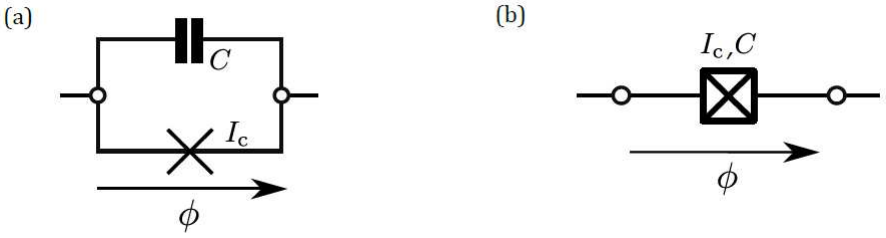

Figure 3.5: Sketches of a Josephson junction. (a) Electrical circuit of a Josephson junction. It can be modeled as a perfect nonlinear element, represented as a cross with a critical current $I_c$in parallel with a capacitor C. (b) Compact representation of (a) [51].

Figure 3.6: On the right a scheme of a Josephson junction composed of SC-insulator-SC, with the cooper pairs tunneling. On the left a microscope image of a JJ.

$$\frac{\mathrm{d}\phi}{\mathrm{d}t} = \frac{V}{\phi_0} \tag{3.22}$$

therefore an AC supercurrent with angular frequency $\omega = V/\phi_0$ is produced by the voltage drop. Combining the effects described by eqs. 3.21 and 3.22 we obtain:

$$L_J = \frac{V}{\mathrm{d}I/\mathrm{d}t} = \phi_0 \frac{\mathrm{d}\phi/\mathrm{d}t}{\mathrm{d}I/\mathrm{d}t} = \frac{\phi_0}{\mathrm{d}I/\mathrm{d}\phi} = \frac{\phi_0}{I_c \cos\phi} = \frac{L}{\sqrt{1-(I/I_c)^2}} \tag{3.23}$$

In the first part of the equation the two Josephson relations are inserted in the definition of inductance. The last equation is obtained combining eq. 3.21 with the fundamental trigonometric relation $(\cos\phi)^2 = 1 - (\sin\phi)^2 = 1 - (I/I_c)^2$, defining $L = \phi_0/I_c$ the linear part of the inductance. Expanding to the second order in I/I_c we get

$$L_J = L + \frac{L}{6}(I/I_c)^2 \tag{3.24}$$

The nonlinear dependence of the JJ inductance on the current, and in turn on the power, is now evident and shows that the JJ is the element that allows for modulation in the LC circuit. An LC circuit whose inductance is due in part to one or more JJ behaves like a parametric amplifier when driven with a sufficiently intense pump tone. One must also take into account the capacitive effect between the two SC leads as a parallel plate capacitor C_J. Therefore a Josephson junction can be modeled as a nonlinear LC circuit with self resonant angular frequency, called plasma frequency $\omega_\Pi = 1/\sqrt{LC_J}$. ω_Π only depends on the thickness of the tunnel barrier, controlled during the fabrication of the junction. Given the typical value for L and C_J, plasma frequency is in the order of the tens of gigahertz. This motivates the use of Josephson based amplifiers in the microwave range. JJs are generally fabricated in a low vacuum pressure environment by first depositing a film of Al or Nb. The oxide layer growth is controlled by letting oxigen enter the chamber at fixed flow and pressure to obtain the wanted tunnel thickness. To complete the junction, oxigen is pumped out and a second SCr layer is produced. The deposition of both the SC layers is performed with litographic techniques. Usual insulator thickness is of the order of some nanometers while its area typically extends on few squared micrometers. A simple JJ design and a microscope image are displayed in Fig. 3.6.

In the cQED formalism, replacing the linear inductance L of the LC resonator with a JJ modifies the functional form of the potential energy, resulting in the new Hamiltonian

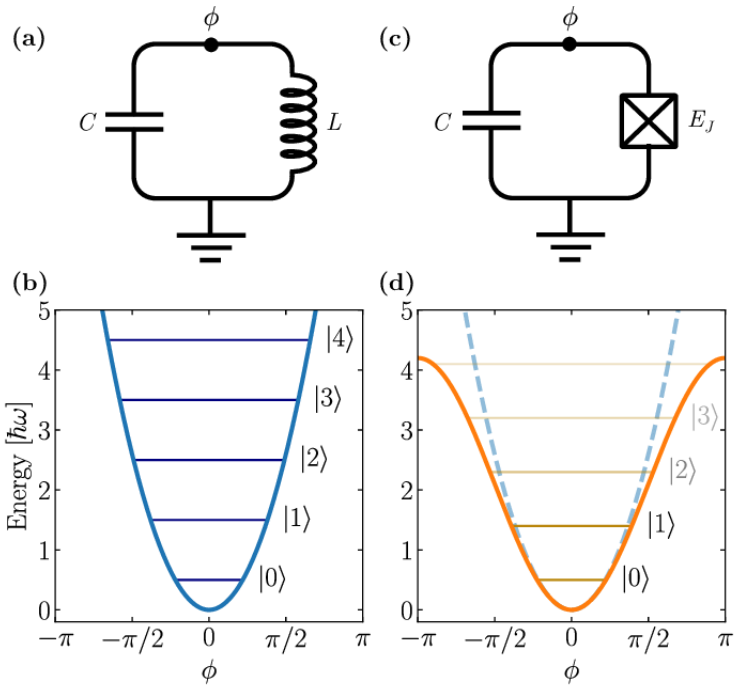

Figure 3.7: Circuit schemes of LC and JJ circuits with relative harmonic and anharmonic potential with respect to the flux coordinate [56]

$$H = 4E_C n^2 - E_J \cos(\phi) \tag{3.25}$$

where $E_C = e^2/(2C_\Sigma$, $C_\Sigma = C_s + C_J$ is the total capacitance, sum of the shunt capacitance C_s and the self capacitance of the junction C_J, and $E_J = I_c\phi_0$ is the Josephson energy. The effect of the JJ on the LC circuit QHO potential energy is depicted in Fig. 3.7

3.2.3 DC SQUID

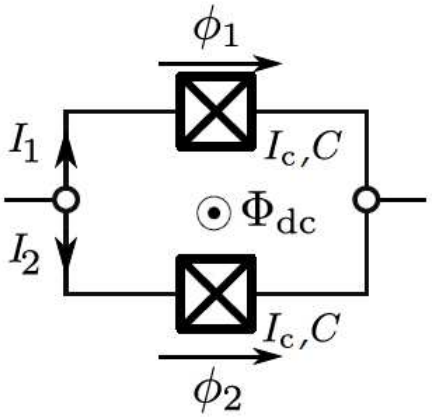

Figure 3.8: Schematic of a symmetric DC SQUID. Two identical Josephson junctions are in parallel in a SC loop. The loop is threaded with an external DC magnetic flux Φ_{DC} [51].

Another non-linear element that is of importance for the present thesis is the DC Superconducting QUantum Interference Device (SQUID). In its simplest realization it consists of a SC loop with two identical JJ in parallel, as represented in Fig. 3.8, in which an external applied magnetic field B sources

a magnetic flux Φ_{dc}. The total current flowing in the loop is

$$I_{tot} = I_1 + I_2 = I_c \sin\phi_1 + I_c \sin\phi_2 = 2I_c \cos\left(\frac{\phi_1 - \phi_2}{2}\right) \sin\left(\frac{\phi_1 + \phi_2}{2}\right) \tag{3.26}$$

where I_c is the critical current of the identical JJs, and ϕ_1 and ϕ_2 are the phase difference across the two JJs labelled as in the scheme. The supercurrent flowing in the loop when threaded by an external magnetic field follows the formula

$$J_s = \frac{\hbar\rho e}{m}\left(\nabla\theta - \frac{2eA}{\hbar}\right) \tag{3.27}$$

where ρ is the density of Cooper pairs, e and m respectively the charge and mass of the electron, A the vector potential, here defined through $B = \nabla \times A$, and $\nabla\theta$ the gradient of the SC phase [28]. In this way we obtain a relation between the phase gradient and the external magnetic field. If we consider the bulk of the ring, J_s tends to zero and leaves $\nabla\theta = A/\phi_0$. We can now calculate the circulation of these two quantities in the loop, considering a contour entirely in the bulk superconductor. In the DC SQUID the circulation of $\nabla\theta$ is equal to the difference between ϕ_1 and ϕ_2, while

$$\oint_{\text{SQUID}} \frac{A}{\phi_0} \cdot \mathrm{d}l = \int_\Sigma \Sigma\nabla \times \frac{A}{\phi_0} = \int_\Sigma \Sigma\frac{B}{\phi_0} = \frac{\Phi_{dc}}{\phi_0} \tag{3.28}$$

where we used the Stoke's theorem to pass from a line integral on the SQUID loop to an integral on the surface enclosed by the SQUID. From these two relations we get $\phi_1 - \phi_2 = \frac{\Phi_{dc}}{\phi_0}$, therefore the total current becomes

$$I_{tot} = 2I_c \cos\left(\frac{\Phi_{dc}}{2\phi_0}\right) \sin\left(\frac{\phi_1 + \phi_2}{2}\right) = I_c^{rm_{SQUID}} \sin\phi_{tot} \tag{3.29}$$

with the phase mean value $\phi_{tot} = (\phi_1 + \phi_2)/2$ and the SQUID critical current $I_{c_{SQUID}} = 2I_c \cos(\Phi_{dc}/(2\phi_0))$ As a consequence the DC SQUID can be treated as a single JJ with a flux modulated maximum supercurrent and a flux tunable inductance

$$L_{\text{SQUID}} = \frac{\phi_0}{I_{tot}} = \frac{L_J}{2\cos(\Phi_{dc}/(2\phi_0))} \tag{3.30}$$

This equation illustrates that the DC SQUID can be used both as a tunable inductance as well as a non-linear element to build a parametric amplifier.

The use of a SQUID in place of a single JJ changes the cQED Hamiltonian in

$$H = 4E_C n^2 - 2E_J \left|\cos(\Phi_{dc}/(2\phi_0))\right| \cos(\phi) \tag{3.31}$$

3.3 The basic Josephson Parametric Amplifier

A basic implementation of JJ and DC SQUID in a JPA is schematized in Fig. 3.9. The device usually consists of a coplanar waveguide resonator shorted to ground via a Kerr-nonlinearity, represented in the figure as lumped elements. In the scheme the former component is a quarter-wavelength resonator $\lambda/4$ denoted in blue while the latter consists of two parallel Josephson junctions forming a SQUID, denoted in orange.

There are two different mixing processes that can be exploited in JPAs, depending on how the pumping process is implemented. They are referred to as "current-pumping" and "flux-pumping", illustrated in Figs. 3.9(b) and 3.9(c) respectively. In the current-pumping case, the system can be modeled as a Duffing oscillator, with a fourth-order nonlinear term in its Hamiltonian, due to the "Kerr non-linearity", that generates a 4WM process[36]. In the flux-pumped case, the parametric process is driven by threading a magnetic flux Φ_{ac} through a SQUID loop. In turn Φ_{ac} modulates the frequency of the resonator, resulting in a third-order term nonlinearity and a 3WM process.

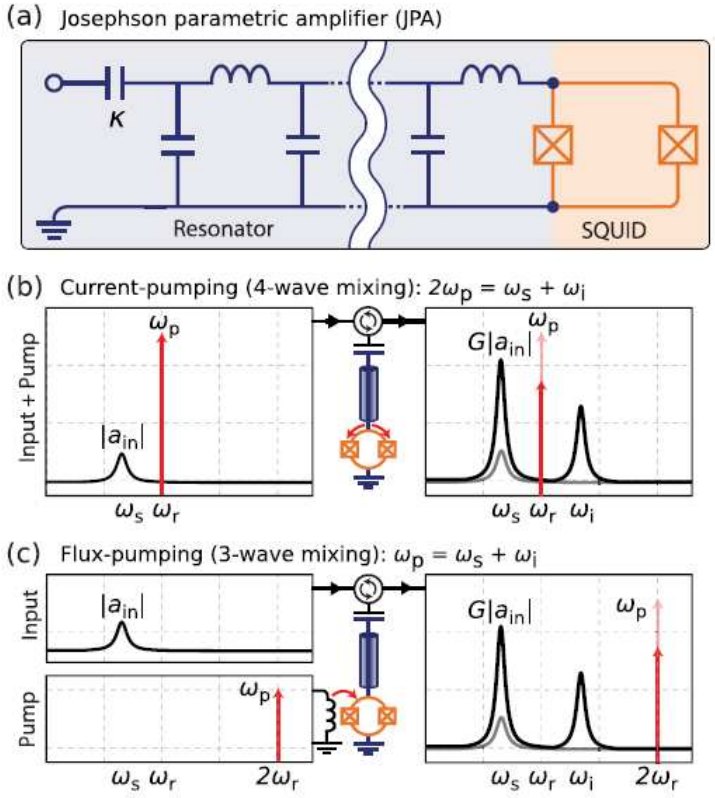

Figure 3.9: Circuit schematics and pump schemes of a Josephson parametric amplifier. (a) The device consists of a quarter-wavelength resonator (blue), represented as lumped elements, shorted to ground via a Kerr-nonlinearity consisting of two parallel Josephson junctions (orange) forming a SQUID. The pump (red) can be applied in two ways; (b) either by modulating the current through the junctions (four-wave mixing) at the resonant frequency, $\omega_p \approx \omega_r$, or (c) by modulating the ac-flux Φ_{ac} around a static DC-flux point Udc using a separate fast-flux line (three-wave mixing). The flux pump is applied at twice the resonance frequency, $\omega_p \approx 2\omega_r$ [36].

3.3.1 The TWPA

Another remarkable application of the Josephson effect is the Josephson Traveling Wave Parametric Amplifier (JTWPA). These devices exploit a 4WM process through the Kerr nonlinearity in an array of JJ, diluting the parametric amplification on the whole length of its transmission line (fig. 3.10). It amplifies in transmission, with both pump and signal injected through the same port. Thus no circulators are needed to separate input and output. Its behaviour resembles that of nonlinear optical crystals ([11]), in which phase-matching issues come into play. Circuit engineering allows to overcome these issues with solutions borrowed from quantum optics and photonics [51].

3.4 The Josephson Parametric Converter

The first stage of the receiver chain in the present thesis test is a Josephson parametric converter (JPC) (or Josephson Mixer). This circuit is based on the Josephson Ring Modulator (JRM) first introduced by the group of Michel Devoret at Yale University [9], [10]. In particular the JPC in use in this experiment employs a shunted JRM, consisting of a ring of four identical Josephson junctions connected to the center of the ring by four linear inductors (Fig. 3.13), with amplifying resonant frequency that can be ideally tuned by threading a magnetic flux in the ring.

The simplest JPC design is depicted in Fig. 3.11 (a), in which a shunted JRM is coupled with three modes of angular frequency ω_a, ω_b and ω_c. This circuit can be used to accomplish parametric down-conversion (Fig. 3.11 (b)), which allows for amplification and entanglement generation, or for noiseless frequency conversion (Fig. 3.11 (c)). For the first the mode used as pump is driven at the sum of the

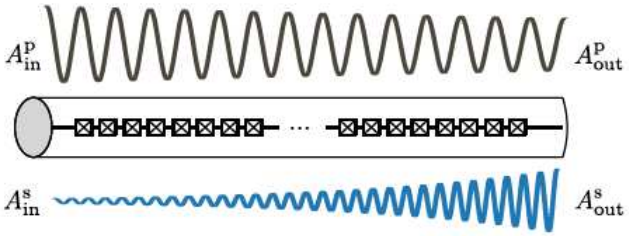

Figure 3.10: Schematic of a traveling-wave (TW) amplifier. The signal is amplified along the nonlinear transmission line. It is co-propagating with the pump, whose amplitude decreases since there is energy exchange between the pump and the signal [51].

angular frequencies of the two other modes, while the latter occurs when the pump has an angular frequency equal to the difference of the other modes.

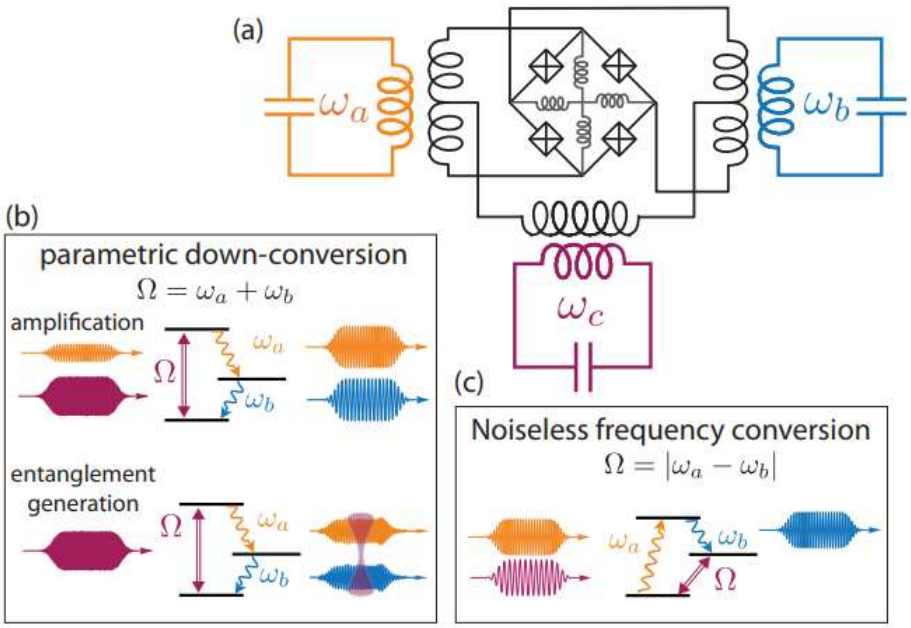

Figure 3.11: (a) Electronic scheme of a shunted Josephson Ring Modulator (JRM) inductively coupled to three modes $\hat{a}$, $\hat{b}$ and $\hat{c}$. (b) When the pump is operated at the sum frequency $\Omega = \omega_a + \omega_b$, the JRM performs a parametric down-conversion. It can then be used for amplification and entanglement generation. (c) When the pump is operated at the difference frequency $\Omega = |\omega_a - \omega_b|$, the JRM performs a noiseless frequency conversion [27]

.

Before presenting the distinctive features of the JPC in its parametric amplifier modality, the JRM 3WM Hamiltonian and the flux dependence of the modes frequencies are derived analyzing the circuit with the cQED theory.

The shunted JRM Hamiltonian is the sum of the energies, seen in section 3.2, of its single elements, namely four JJ and four inductors, labelled respectively a, b, c, d and $\alpha, \beta, \gamma, \delta$ as in Fig. 3.12. The reduced fluxes passing through the elements are indicated with the same labels and those at the ring nodes with the numbers $1, 2, 3, 4$. Thus it's Hamiltonian can be written as

$$H_{ring} = -E_J[\cos\varphi_a + \cos\varphi_b + \cos\varphi_c + \cos\varphi_d] + \frac{1}{2}E_L[\varphi_\alpha^2 + \varphi_\beta^2 + \varphi_\gamma^2 + \varphi_\delta^2] \tag{3.32}$$

The circuit ring can sustain three independent modes, X, Y, Z shown in the right part of Fig. 3.12. These modes arise from the four JJ disposition and can be expressed as a combination of the node fluxes and the external magnetic flux Φ_{ext} threading the ring. In terms of the modes reduced fluxes

$\varphi_X, \varphi_Y, \varphi_Z$ and the the Hamiltonian becomes

$$H_{ring} = -4E_J \cos\frac{\varphi_X}{2}\cos\frac{\varphi_Y}{2}\cos\varphi_Z\cos\frac{\varphi_{ext}}{4} - 4E_J \sin\frac{\varphi_X}{2}\sin\frac{\varphi_Y}{2}\sin\varphi_Z\sin\frac{\varphi_{ext}}{4} + \frac{1}{4}E_L(\varphi_X^2+\varphi_Y^2+2\varphi_Z^2) \tag{3.33}$$

where $\varphi_{ext} = \Phi_{ext}/\varphi_0$ is the reduced external flux.

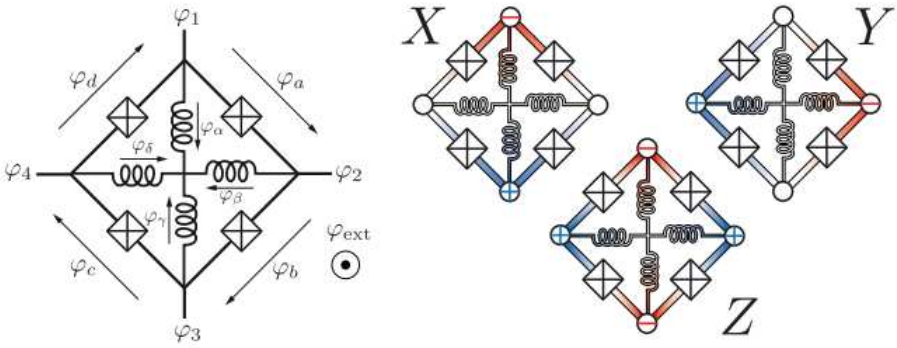

Figure 3.12: Shunted JRM circuit on the right, with represented all the reduced fluxes in the circuit and the external reduced magnetic flux. On the right its three normal modes X, Y, Z (The flux enters from the blue nodes and exits from the reds) [27].

We can have a deeper comprehension of the processes that take place in the JRM by expanding to the third order the Hamiltonian in $\varphi_{X,Y,Z}$

$$\begin{aligned} H_{ring} = &- E_J \sin\left(\frac{\varphi_{ext}}{4}\right)\varphi_X^2\varphi_Y^2\varphi_Z^2 \\ &+ \frac{1}{2}\left(\frac{E_L}{2} + E_J\cos\frac{\varphi_{ext}}{4}\right)(\varphi_X^2+\varphi_Y^2) \\ &+ \frac{1}{2}\left(E_L + 4E_J\cos\frac{\varphi_{ext}}{4}\right)\varphi_Z^2 \\ &- 4E_J\cos\left(\frac{\varphi_{ext}}{4}\right) \\ &+ O(\varphi_{X,Y,Z}^4) \end{aligned} \tag{3.34}$$

The first term of the equation represents the third order 3WM process while the second and the third equation terms produce the frequency tuning as shown in the following.

The JRM inductances relatives to the normal modes are defined as $L^{-1}_{X,Y,Z} = \varphi_0^{-2}\partial^2 H/\partial\varphi^2_{X,Y,Z}$, that solved gives:

$$\begin{cases} L^{\text{JRM}}_{X,Y} = \frac{\varphi_0^2}{\frac{E_L}{2}+E_J\cos\frac{\varphi_{ext}}{4}} \\ L^{\text{JRM}}_{Z} = \frac{\varphi_0^2}{E_L+4E_J\cos\frac{\varphi_{ext}}{4}} \end{cases} \tag{3.35}$$

Note that their value is modulated by the external magnetic flux.

As long as the inductances maintain positive values the system remains stable. One can show that the Z mode inductance always becomes negative before X and Y modes. Therefore the JRM operates in a stable region for $E_L/4 + E_J\cos\varphi_{ext} > 0$. When this condition is not satisfied the system encounters a symmetry breaking. In turn the JPC in which the JRM is implemented loses its parametric down-conversion process. The symmetry breaking range corresponds in Fig. 3.14(c) to the narrow arches while on the steep part of the broad arches the 3WM process is stable.

When the JRM nodes are connected to four resonators one obtains the JPC circuit. In Fig. 3.13 are present a microscope image of the mixer and the equivalent circuit. The resonators connected at nodes 1 and 3 and at nodes 2 and 4 are equal and their inductance and the capacitance are indicated with $L_{a,b}$ and $C_{a,b}$. Comparing Fig. 3.13(c) and the normal modes represented in Fig. 3.12, we can see that the resonators a and b are respectively coupled to the modes X and Y.

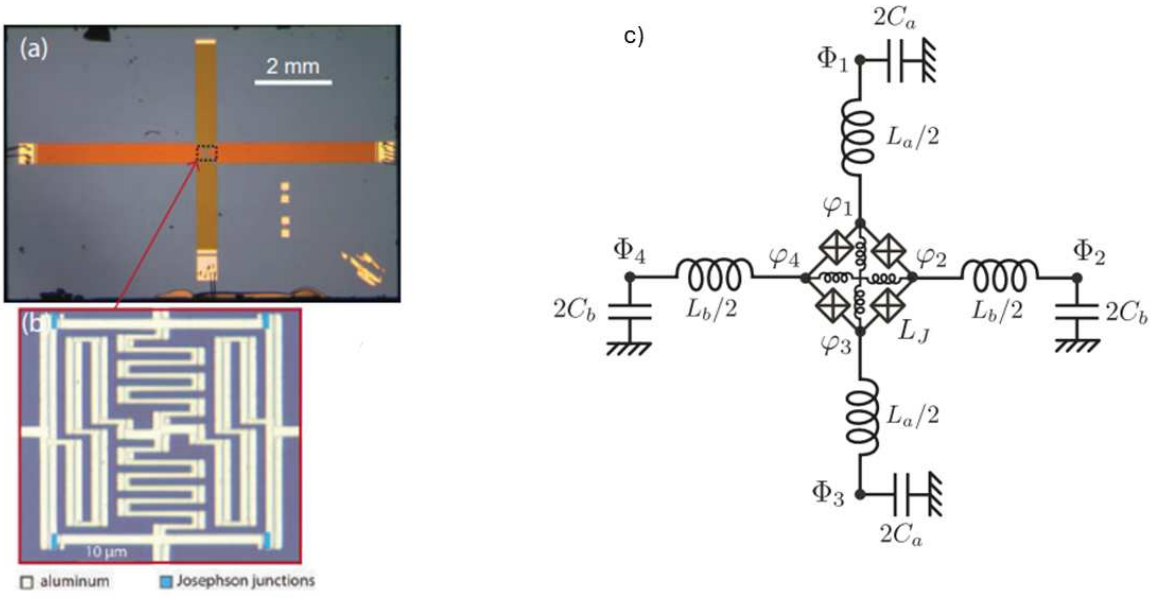

Figure 3.13: (a) microscopic image of Josephson parametric converter circuit. (b) microscopic image of shunted JRM. (c) Relative JPC circuit model [27]

Therefore the JPC can be fed with three resonant modes that can couple to the JRM modes: the differential (Φ_a, Q_a) and (Φ_b, Q_b) will couple to the ring modes φ_X and φ_Y respectively, and the common mode (Φ_c, Q_c) will couple to φ_Z.

The relation between the JRM modes reduced fluxes $\varphi_{X,Y,Z} = \varphi_{a,b,c}$, renamed for simplicity, and the resonant modes $\Phi_{a,b,c}$ is encoded in the participation ratios $\xi_{a,b,c}$

$$\xi_{a,b,c}(\varphi_{ext}) = \frac{\varphi_0 \varphi_{a,b,c}}{\Phi_{a,b,c}} \tag{3.36}$$

This ratio represents the fraction of the resonant mode energy that enters in the JRM.

The circuit can be decomposed in equivalent circuits for the normal modes and the inductances of each normal mode are calculated as:

$$\begin{aligned} L_a^{tot}(\varphi_{ext}) &= L_a + L_a^{JRM}(\varphi_{ext}) \\ L_b^{tot}(\varphi_{ext}) &= L_b + L_b^{JRM}(\varphi_{ext}) \\ L_c^{tot}(\varphi_{ext}) &= \tfrac{L_a + L_b}{4} + L_c^{JRM}(\varphi_{ext}) \end{aligned} \tag{3.37}$$

The quadratic part of the JPC Hamiltonian with these new definition becomes the sum of three LC oscillators, each one belonging to a resonant mode

$$H_{(2)} = \frac{\Phi_a^2}{2L_a^{tot}(\varphi_{ext})} + \frac{Q_a^2}{2C_a} + \frac{\Phi_b^2}{2L_b^{tot}(\varphi_{ext})} + \frac{Q_b^2}{2C_b} + \frac{\Phi_c^2}{2L_c^{tot}(\varphi_{ext})} + \frac{Q_c^2}{2C_c} \tag{3.38}$$

where $C_c = \frac{4C_aC_b}{C_a+C_b}$ is the capacitance of the common mode. The resonant frequency of each mode is then given by the LC circuit formula:

$$\omega_{a,b,c}(\varphi_{ext}) = \frac{1}{\sqrt{L_{a,b,c}^{tot}(\varphi_{ext}) C_{a,b,c}}} \tag{3.39}$$

The dependence of the inductance on the magnetic flux threading the ring, produce modes with tunable resonance frequencies.

The third order term of the JRM Hamiltonian, linked to the 3WM process, can be expressed in the fluxes $\Phi_{a,b,c}$ by using the participation ratio.

$$H_{3WM} = E_J \sin\frac{\varphi_{ext}}{4}\varphi_a\varphi_b\varphi_c = \frac{E_J}{\varphi_0^3}\xi_a(\varphi_{ext})\xi_b(\varphi_{ext})\xi_c(\varphi_{ext})\sin\frac{\varphi_{ext}}{4}\Phi_a\Phi_b\Phi_c. \tag{3.40}$$

We can quantize the fluxes and introduce the creation and annihilation operators of the modes a, b and c, as in eq. 3.17:

$$\hat{\Phi_a} = \sqrt{\frac{\hbar}{2\omega_a C_a}}\left(\hat{a}+\hat{a}^\dagger\right) = \sqrt{\frac{\hbar\omega_a L_a^{tot}}{2}}\left(\hat{a}+\hat{a}^\dagger\right) \tag{3.41}$$

obtaining the Hamiltonian in its quantum form One obtains the Hamiltonian in its quantum form

$$H_{3WM} = \hbar\chi(a+a^\dagger)(b+b^\dagger)(c+c^\dagger) \tag{3.42}$$

where the coupling rate χ is defined as

$$\chi = \frac{E_J}{\varphi_0^3}\xi_a\xi_b\xi_c\sin\left(\frac{\varphi_{ext}}{4}\right)\sqrt{\frac{\hbar\omega_a\omega_b\omega_c L_a^{tot}L_b^{tot}L_c^{tot}}{8}} \tag{3.43}$$

that is the 3WM mixing eq. 3.7 we found in quantum optics, proving that the JPC is effectively a parametric amplifier. Note that this circuit is only operable as a phase-preserving amplifier, since signal and idler modes are coupled to different resonators and therefore they are never temporally matched.

As shown in Fig. 3.14a-b the JPC achieves amplification up to over 30 dB gain G. When the gain exceeds 5 dB, the gain-bandwidth relation (see eq. 3.14) holds to less than a MHz deviation for both signal and idler. In particular for a $G = 20\,\mathrm{dB}$, necessary to overcome the noise of the HEMT following in the amplifying chain, the JPC has a bandwidth of 3 MHz. In Fig. 3.14c the measured resonance frequency of the signal cavity is plotted as a function of the applied flux to the ring modulator without pump. Note that in the wide arches the frequency follows the behaviour of eq. 3.39 (solid line).

As expected in the symmetry breaking region (narrow arches) there is no amplification, while $G \sim 20\,\mathrm{dB}$ is observed in the range from 8.1 to 8.5 GHz (Fig. 3.14(d)). The final tuning range is of $\sim$ 400 MHz, two orders of magnitude greater than the bandwidth. In the Fig. 3.14(d) the labels reported near the gain curves represent the number of input photons per dynamical bandwidth for different signal frequencies at the 1 dB compression point. Note that the number is smaller at frequencies near the instability region (Fig. 3.14(c)), due to saturation or pump depletion for lower signal powers.

As concerns added noise, for the JPC in this publication [58] an added noise temperature $T_n = 1.14\,\mathrm{K}$ has been measured, making the JPC 20-40 times better than the best commercial HEMT amplifier. Yet it is still about five and a half times noisier than the SQL.

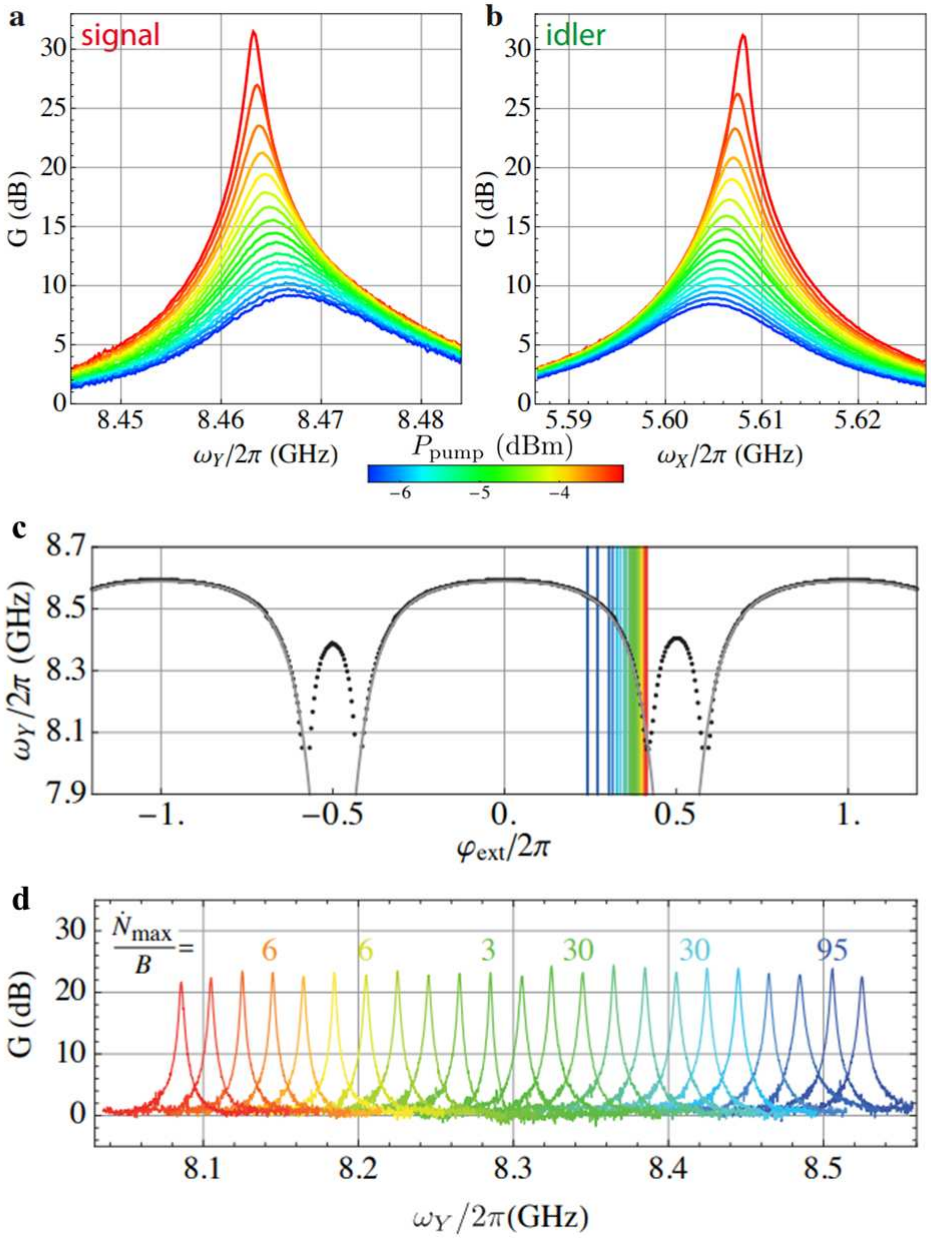

Figure 3.14: Main measured characteristics of JPC, as Gain dependence on pump power (a, b) and on flux bias (c, d) [58]

Chapter 4

Experimental apparatus

As detailed in chapter 2, a haloscope detector is a microwave cavity immersed in a static magnetic field readout a low noise receiver chain. In this thesis we focus on minimizing noise added by the electronic chain, through the utilization of a SC parametric amplifier. These amplifiers reach the so called Standard Quantum Limit (SQL) where noise is set by the quantum fluctuation of the microwave field. The cavity and the first stage of amplification, together with some components of the receiver chain are cooled down to mK temperatures, to minimize the thermal noise. To reach these temperatures we use a dilution refrigerator (DR) whose working principle is described in sec 4.1 The 3D resonator geometrical parameters and expected lowest frequency electromagnetic modes will be given in section 4.2. together with a general description of the receiver components in section 4.3 The estimates that were needed to correctly equip the DR and the final scheme employed in this thesis are reported in section 4.4

4.1 The dilution refrigerator

To reach millikelvin temperatures the dilution refrigerator (DR) exploits the properties of the two isotopes of helium, ^{3}He and ^{4}He, in their liquid phase.

The insert of DR used in this thesis is shown in Fig. 4.1. . The main structure entails five gold plated copper plates whose thermodynamical temperature T and cooling power are reported in tabs. 4.1c,4.1b,4.1a The most important processes take place in the still (ST) and the mixing chamber (MXC) plates. In the latter ^{3}He is mixed with ^{4}He, absorbing energy from the surrounding environment.

Temperature	Cooling power
100 mK	1.296 mW
92.4 mK	1 mW
23.6 mK	26 μW

(a)

Plate	Temperature
50 K	35 K
4 K	2.85 K
Still	882 mK
CP	82 mK
MXC	6 mK

(b)

Plate	Temperature	Cooling power
50 K	45 K	30 W
4 K	4.2 K	1.5 W
Still	1.2 K	40 mW
CP	140 mK	200 μW
MXC	20 mK	19 μW

(c)

Table 4.1: (a) Measured cooling powers at different temperature of the MXC at the commissioning of Leiden Cryogenic DR used in this experiment. (b) Measured lowest temperatures of different plates at the commissioning of Leiden Cryogenic DR used in this experiment. (c) Cooling powers and temperature of bluefors XLD400DR (DR similiar to experimental apparatus one)[37].

Basic properties of dilution refrigerator process

The properties of ^{3}He and ^{4}He isotopes necessary for the DR are the following:

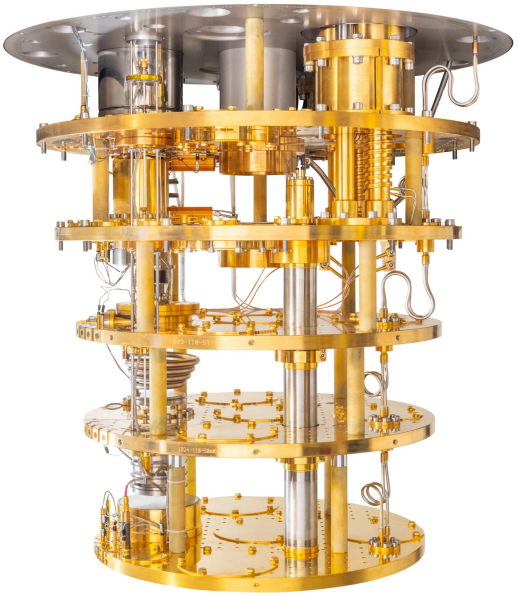

Figure 4.1: Image of the DR of this experimental apparatus unequipped. [18]

1. As shown in the ^{3}He–^{4}He mixture phase diagram in Fig. 4.2a, when cooled below 0.87 K the mixture undergo phase separation, resulting in two different phases between which the ^{3}He atoms can be transferred. The ^{3}He-rich phase is known as concentrated phase while the one poor of ^{3}He is the dilute phase.

2. The specific heat of a ^{3}He atom is larger in the dilute phase than in the concentrated phase. Therefore when an ^{3}He atom passes from the concentrated phase to the dilute phase results in an effective "production of cold" .

3. There is a finite solubility of ^{3}He in ^{4}He even for temperatures approaching absolute zero, corresponding to a ^{3}He concentration $x_{3,d} = 6.6\%$, (see Fig.4.2a) that allows for temperature-independent high ^{3}He molar flow rate. For this reason the cooling power decreases only with T^2, as the specific heats of concentrated and diluted ^{3}He at low enough temperatures are proportional to T. For comparison, the cooling power of the evaporation cooling decreases exponentially with T as shown in Fig. 4.3a

4. The vapour pressures of ^{3}He and ^{4}He at the same temperature are significantly different, as shown in Fig. 4.3b. This allows for pure ^{3}He circulation when the system is pumped.

5. An osmotic pressure difference builds up when helium mixtures at different locations in a cryogenic apparatus have different temperatures and/or concentrations (see Fig. 4.2b).

Owing to the second property given, the cooling power can be calculated as heat of mixing with the formula

$$\dot{Q} = \dot{n}_3[H_d(T) - H_c(T)]. \tag{4.1}$$

When ^{3}He atoms are transferred at a molar flow $\dot{n}_3$ from the concentrated to the dilute phase, cooling results according to the enthalpy difference of the two phases.

Enthalpy is given by

$$H(T) - H(0) = \int_0^T C(T)\mathrm{d}T \tag{4.2}$$

where $C(T)$ is the temperature dependent molar heat capacity. For temperatures below 40 mK and at saturated vapour pressure, C has a linear dependence with the temperature, that is, for concentrated and dilute phase, respectively

$$C_{3,c} = 22T\,[\mathrm{J(mol \cdot K)^{-1}}]$$

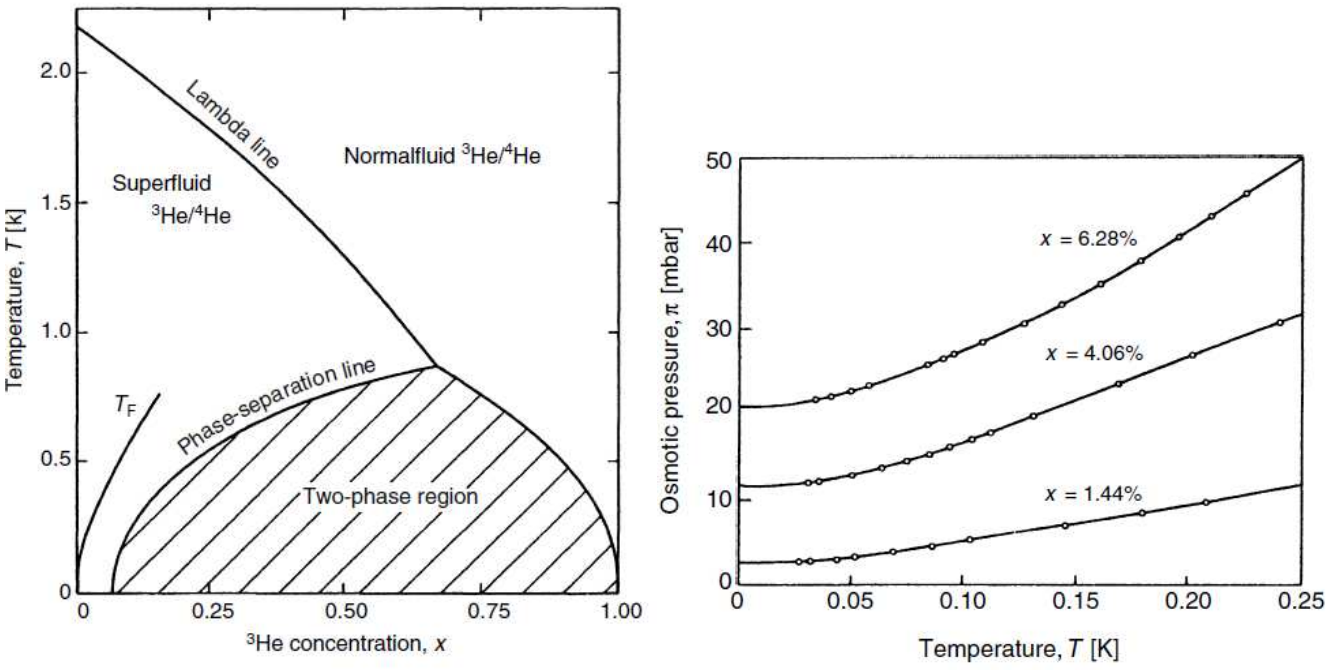

(a) (b)

Figure 4.2: (a) Phase diagram of the ^{3}He-^{4}He mixture with respect to temperature and concentration of ^{3}He. (b)Osmotic pressure diagram of ^{3}He and ^{4}He at different mixture concentrations with respect to temperature [53]

$$C_{3,d}(6.6\%) \simeq 106T\,[\mathrm{J(mol(}^3He\mathrm{)K)}^{-1}]$$

Thus the enthalpy of pure ^{3}He results

$$H_3(T) = H_3(0) + 11T^2\,[\mathrm{Jmol}^{-1}] \tag{4.3}$$

and the one of the dilute phase can be proven equal to

$$H_{3,d}(T) = H_3(0) + 95T^2\,[\mathrm{J(mol(}^3He\mathrm{))}^{-1}] \tag{4.4}$$

Combining eq. 4.3 and 4.4 in eq. 4.1 we get the effective cooling power of the ^{3}He-^{4}He mixing process:

$$\dot{Q} = \dot{n}_3[H_{3,d}(T) - H_3(T)] = 84\dot{n}_3T^2\,[\mathrm{W}]. \tag{4.5}$$

^{3}He atoms can be tranferred from the concentrated to the diluted phase by exploiting properties 4 and 5. The osmotic pressure difference between the mixing chamber and the still can be expressed using the Van't Hoff's law [53] obtaining:

$$\pi_{\mathrm{MXC}} - \pi_{\mathrm{ST}} \simeq \frac{(x_{\mathrm{MXC}}T_{\mathrm{MXC}} - x_{\mathrm{ST}}T_{\mathrm{ST}})R}{V_{m,4}} \tag{4.6}$$

where $V_{m,4}$ is the molar volume of ^{4}He, $R = 8.31\,[\mathrm{J/(mol \cdot K)}]$ is the molar gas constant and x_{MXC}, x_{ST} are respectively the ^{3}He concentration at the MXC and ST stages and their corresponding temperatures T_{MXC} T_{ST}. At equilibrium the two osmotic pressures will be the same. If we assume that $x_{\mathrm{MXC}} = 6.6\%$, $T_{\mathrm{MXC}} = 10\,\mathrm{mK}$ and $T_{\mathrm{ST}} = 0.7\,\mathrm{K}$, we get

$$x_{\mathrm{ST}} = x_{\mathrm{MXC}}\frac{T_{\mathrm{MXC}}}{T_{\mathrm{ST}}} \approx 0.1\% \tag{4.7}$$

By pumping ^{3}He from the still (see Fig. 4.4), its concentration decreases and in the limit in which x_{ST} tends to zero, we obtain the maximum osmotic pressure difference:

$$\Delta\pi_{max} = \frac{x_{\mathrm{MXC}}RT_{\mathrm{MXC}}}{V_{m,4}} \simeq 20\,\mathrm{mbar}. \tag{4.8}$$

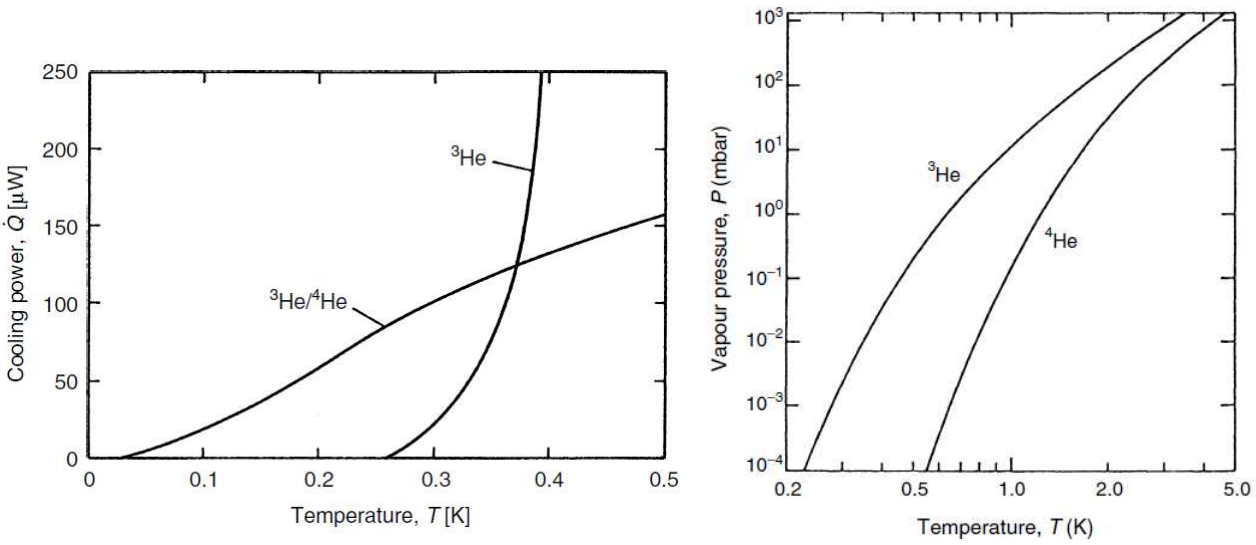

(a) (b)

Figure 4.3: (a) Comparison between the cooling power of the two cooling process with respect to the system temperature. (b) Vapour pressure of ^{3}He and ^{4}He with respect to temperature[53].

This pressure is sufficiently large to drive the ^{3}He from the mixing chamber into the still even if they are separated by a vertical distance of about 1 m.

Operation of the dilution refrigerator

Now that the origin of the cooling power and of the ^{3}He atoms moving force are explained, the DR work cycle can be presented. ^{3}He and ^{4}He gases, initially stored in the gas handling system, are allowed to circulate in the fridge once the whole insert has been precooled by liquid nitrogen and the pulse tube to ~ 3 K (see section 4.1.1). At this temperature ^{4}He is in its liquid state and can be further cooled down by evaporating cooling to about 1.3 K. At about 1.5 K the condensation of ^{3}He takes place, and as for ^{4}He, its temperature can be lowered down to 0.3 K through pumping. As previously mentioned, at 0.87 K, phase separation between ^{3}He-^{4}He mixtures occurs and in turn cooling due to enthalpy of mixing is accomplished. Referring to Fig. 4.4b DR scheme, after pumping on the still mixture, ^{3}He atoms are driven by the osmotic pressure imbalance from the MXC to the still. The dilute phase in the MXC is refurbished of ^{3}He atoms from the concentrated phase, that have absorbed heat from the local environment by passing through the phase boundary.

The cold ^{3}He flux coming up from the MXC to the Still is used to cool down the ^{3}He atoms that are refilling the concentrated phase. This cooling is accomplished through a continuous flow heat exchanger followed by step heat exchangers (see Fig. 4.4a).

These exchangers are designed to minimize the thermal boundary Kapitza resistance R_K, which limits heat transfer at low temperature:

$$R_K = \frac{\Delta T}{\dot{Q}} \propto \frac{1}{T^3 A} \tag{4.9}$$

with A surface area. The continuous flow exchanger maximizes the contact area via two concentric tubes, with the internal spiralled inside the external one. To reach even smaller temperatures, step exchangers are employed. These are made of sintered metal powder, than can increase the effective internal contact area up to hundreds of m^2. The base temperature of the DR is determined by the efficiency of the heat exchangers, in which the incoming ^{3}He is cooled by the outgoing ^{3}He in an effective manner. In fact, using the enthalpy balance between the diluted phase at thermal equilibrium at T_{MXC} and the incoming external flow of concentrated ^{3}He at T_{EX}, the MXC cooling power is:

$$\dot{Q} = \dot{n}_3(95T^2_{\mathrm{MXC}} - 11T^2_{\mathrm{EX}}) \tag{4.10}$$

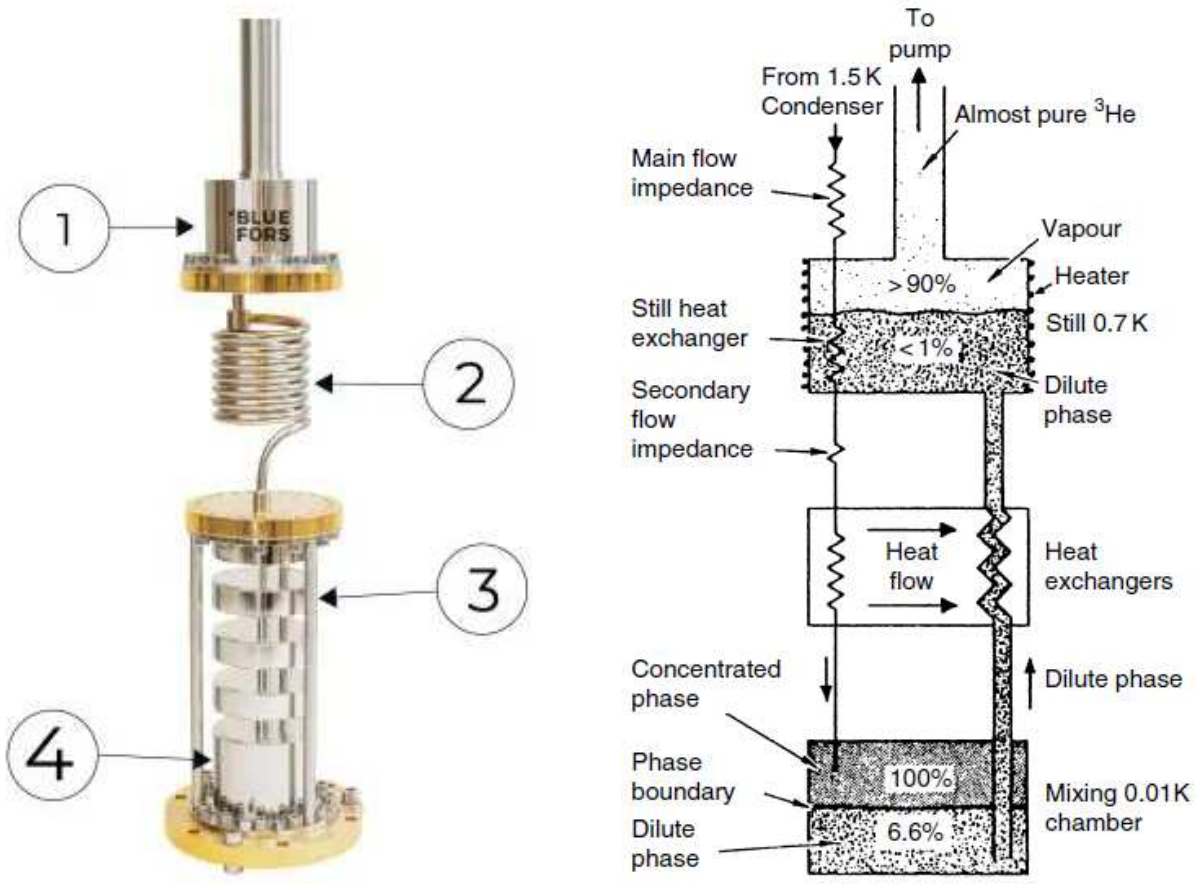

(a) (b)

Figure 4.4: (a)Scheme of the lowest part of the dilution refrigerator, the dilution unit. 1. Still, 2. Continuous flow heat exchangers, 3. Step heat exchangers, and 4. Mixing chamber.[34] (b) Scheme of the dilution refrigerator technique following the ^{3}He flow.[53]

Note that the available cooling power is determined not only by the circulation rate of ^{3}He, but also by T_{EX}. In particular, for $T_{EX} \geq 3T_{MXC}$ there is no cooling power. Temperature can be lowered only by increasing the thermal exchange in the incoming flow.

The various DR plates are inserted into metal cylinders thermalized with the upper level plate. These cylinders act as radiation shields, lowering the heat transfer coming from thermal radiation. In fact the transmission of heat via black-body radiation depends on the temperature as $\dot{Q} \propto T^4$. Thus if we dissipate this heat in multiple steps, its weight on the MXC cooling power is suppressed, up to a factor $\sim 10^{14}$.

4.1.1 The pulse tube cryocooler

For precooling a pulse tube cryocooler (PTC) is mounted on the DR. PTC is a closed cycle refrigerator that achieves cooling down to $\sim$3 K by letting helium gas at 10–20 bar perform work during its compression and expansion. In a pulse-tube cooler the cooling effect relies on smooth periodic, quasi-adiabatic pressure variations and displacement of the working gas in the "pulse" tube (Fig. 4.5), achieved by a pressure wave generator, that can be either a high-frequency pressure oscillator or a low-frequency compressor. Directly connected to the compressor, there is the regenerator, a chamber containing a porous magnetic material of high heat capacity which acts as heat reservoir. Its cold end, at the bottom of Fig. 4.5, is joined to the pulse tube, a simple hollow tube. At its ambient temperature end, this tube is connected through a flow impedance or "orifice" to a reservoir; the buffer volume of the latter is large enough that its pressure can be considered constant. The gas flow oscillating through the orifice separates the heating and cooling effects.

During the compression phase, the gas flows in the system basically from the piston to the reservoir. Part of the heat of compression (Q_o) at the generator is removed by a heat exchanger to the surrounding, usually by cooling water. The regenerator takes up further heat from the gas while it passes from the compressor to the pulse tube. About one third of the gas in the pulse tube at its hot end flows through the orifice into the reservoir and gives off heat (Q_h) to the surrounding.

During the expansion phase, the flow is reversed. The gas at the pulse tube cold end expands, lowering its temperature and taking up heat through a heat exchanger from the external environment. This provides the desired cooling power (Q_c). Part of the reservoir gas returns back to the pulse tube hot end and the cold gas is reheated by passing through the regenerator to a temperature a bit lower than the initial one. Therefore multiple cycles allow the cooling of the internal gas and of the elements connected to the cool end heat exchanger.

The function of the pulse tube is to insulate the processes at its two ends. It must be large enough that gas flowing from one end traverses only part of the tube before flow is reversed. Therefore, flow from the cold end never reaches the warm end and in the middle portion a temperature gradient is formed. Maximum cooling efficiency is obtained by properly adjust the phase between the generated pressure wave and the gas velocity in the tube.

The absence of moving parts at its cold end strongly reduces the influence of vibrations to the connected experiment. The cooling power goes to zero when the thermal expansion coefficient of the compressed gas goes to zero. This happens at 2 K for ^{4}He and around 1 K for ^{4}He at a pressure of 15 bar. The unit available in the present DR can deliver up to 1 W at 4.2 K.

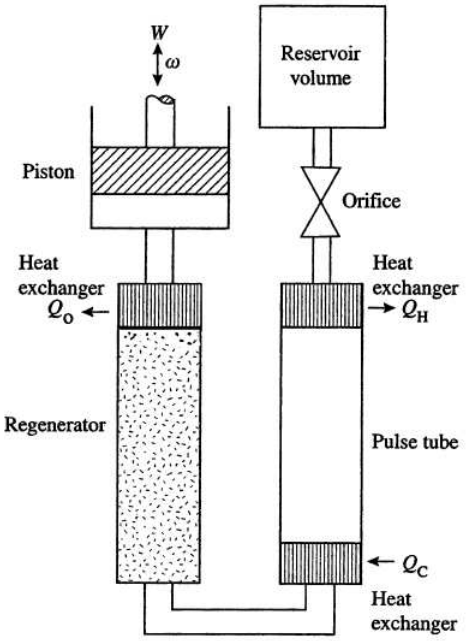

Figure 4.5: Pulse tube scheme[53].

4.1.2 Thermometers

Knowing the temperature of each component that needs to be cooled in this experimental apparatus is of importance to assess the noise contributions. The fridge si equipped with a number of temperature sensors, listed in tab. 4.2. They are of different types, as detailed in the following sections.

Resistance thermometers

Resistance thermometry is based on the temperature dependence of the electrical resistance of metals, semiconductors or complicated compounds. As the resistivity has no simple, a priori known temperature dependence, a calibration is often needed.

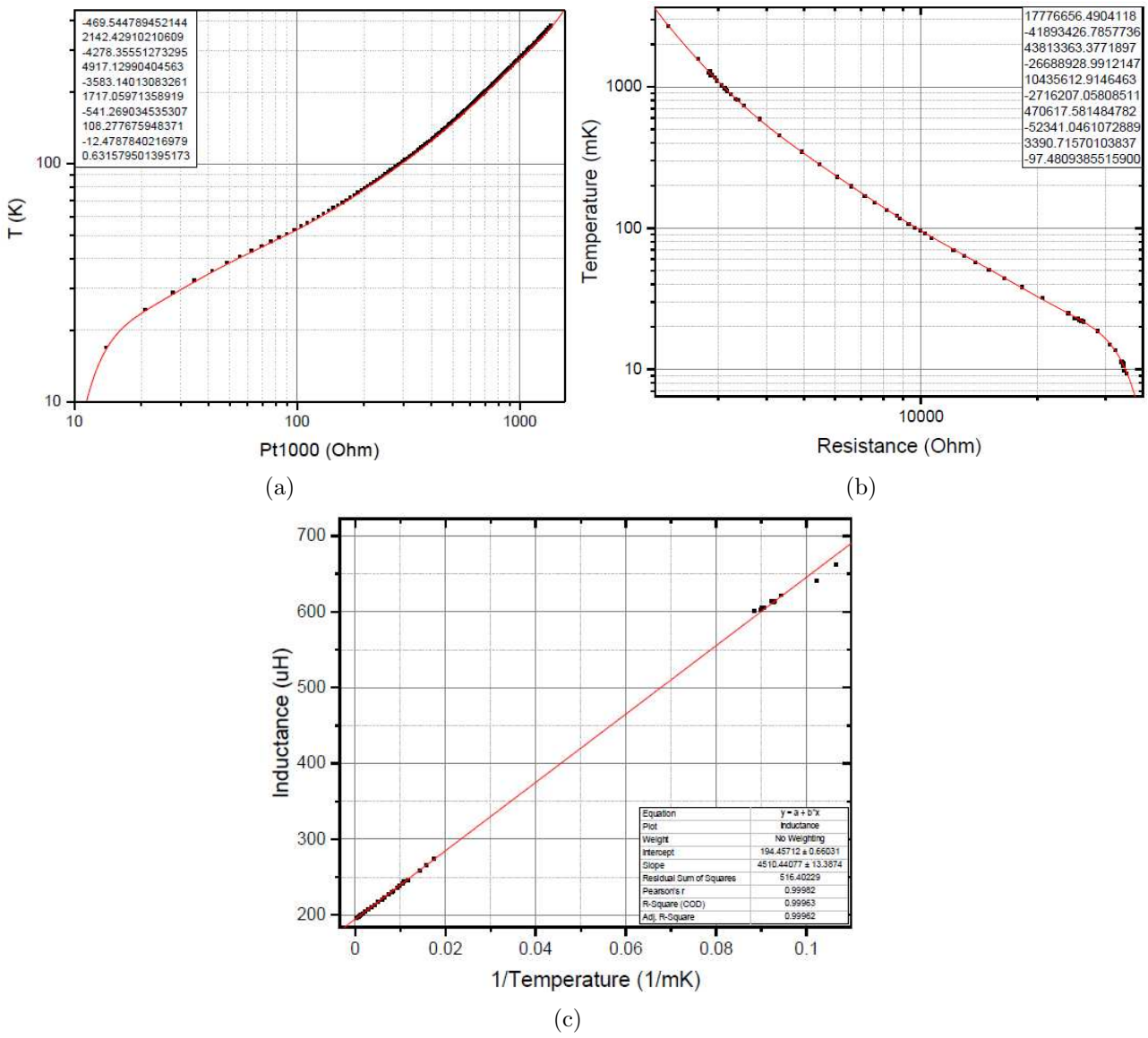

Figure 4.6: Datasheet plots of thermometers calibration results of respectively Pt1000 (a), TT-2146 (b) and CMN 1020-173 (c).

Platinum is the pure metal most commonly used for resistance thermometry. In fact it is chemically resistant, can be obtained with high purity, which diminishes the temperature-independent residual resistivity part, and its R–T dependence is linear over an appreciable temperature range, see Fig. 4.6a. A Pt-1000 thermometer is a platinum resistor with a resistance of exactly $1000\,\Omega$ at 0°C. As a drawback, sensitive thermometry with a Pt resistor or with other pure metals is only possible down to about 10 K; at lower temperatures the temperature-independent component becomes relevant.

The thermometers named RuO2 10k(n), RuO2 1k5 and TT-2146 are metal-ceramic composites consisting of a mixture of conductive RuO2 and Bi2RuO2 embedded in a lead silicate glass matrix, deposited on an alumina substrate and heated to above its glass point. The resulting negative non-metallic resistance characteristic, see Fig. 4.6b, depends mostly on the metal-to-glass ratio. Among their properties the most notable are reproducibility, weak magnetoresistance, small size and mass and low cost. Resistors with room temperature values in the range of 0.5 to a few kΩ are suitable for low-temperature thermometry with a sensitivity comparable to that of Ge resistance thermometers. Their R-T dependence in a limited temperature range between 0.05 and 0.5 K can be well described by the expression

$$R = R_0 \exp(T_0/T)^{1/4} \tag{4.11}$$

with the constants R_0 and T_0 depending on composition fits the data well. This dependence cor-

responds to an electronic conduction mechanism due to variable-range hopping in three dimensions between localized states near the Fermi energy with a constant electronic density of states.

magnetic thermometer

CMN 1020-173 belongs to the magnetic thermometers exploiting electronic paramagnets properties. It relies on the T^{-1} dependence of the magnetization

$$M = \frac{\lambda B}{\mu_0 T} \tag{4.12}$$

of a paramagnet with the Curie constant λ. These equations are valid for temperatures greater than the ordering temperature T_c, where the susceptibility follows the Curie law. The magnetization is measured as a variation of the inductance of a coil containing the paramagnet.

Substances suitable for electronic magnetic thermometry are paramagnets containing elements with partly filled 3d or 4f electronic shells. The paramagnetic salt with the lowest ordering temperature is Cerium Magnesium Nitrate (CMN) with $T_c \simeq 2\,\mathrm{mK}$. These salts can be used over the widest temperature range known and indeed it is the most widely applied paramagnetic thermometer.

Noise Thermometry

The conduction electrons in a metal perform random thermal movements (Brownian motion), which result in statistical voltage fluctuations of a resistive element. Therefore all resistive elements of an electronic circuit are noise sources.

The Nyquist theorem derives the following equation for the component of the time averaged noise voltage within the frequency band $\Delta\nu$ of a resistor with value R at temperature T:

$$\langle u^2 \rangle = 4 k_B T R \Delta\nu \tag{4.13}$$

Therefore by measuring the time averages mean square noise voltage produced by a known resistance in a certain frequency band, we can derive the resistance temperature. Noise voltages at low temperatures are very small, producing for instance $10^{-8}\,\mathrm{V}$ at 4 K or $10^{-9}\,\mathrm{V}$ at 10 mK. Those values are usually not measurable with semiconductor amplifiers and therefore one has to rely on a SQUID with its extremely low intrinsic noise as the amplifying element.

Thermometer	Plate	Temperature range
Pt1000	50 K	$300 \div 10\,\mathrm{K}$
Pt1000	3 K	$300 \div 10\,\mathrm{K}$
RuO2 10k(n)	3 K	$10 \div 0.6\,\mathrm{K}$
RuO2 10k(n)	Still	$10 \div 0.6\,\mathrm{K}$
RuO2 1k5	CP	$4000 \div 20\,\mathrm{mK}$
Pt1000	MXC	$300 \div 10\,\mathrm{K}$
TT-2146	MXC	$3\,\mathrm{K} \div < 10\,\mathrm{mK}$
CMN 1020-173	MXC	$300\,\mathrm{K} \div < 10\,\mathrm{mK}$

Table 4.2: Thermometers and plates where are positioned. The temperature range is only an estimate from the calibration plots in the DR datasheet

4.2 Cavity parameters

The cavity used in the present experiment is a cylindrical copper cavity of internal radius $R \sim 6.94\,\mathrm{cm}$ at $T \sim 10\,\mathrm{mK}$.

Its lowest TM mode it's the TM_{010} with frequency

$$f_{TM010} = \frac{2.405 \cdot c}{R} \sim 10.4017\,\mathrm{GHz} \tag{4.14}$$

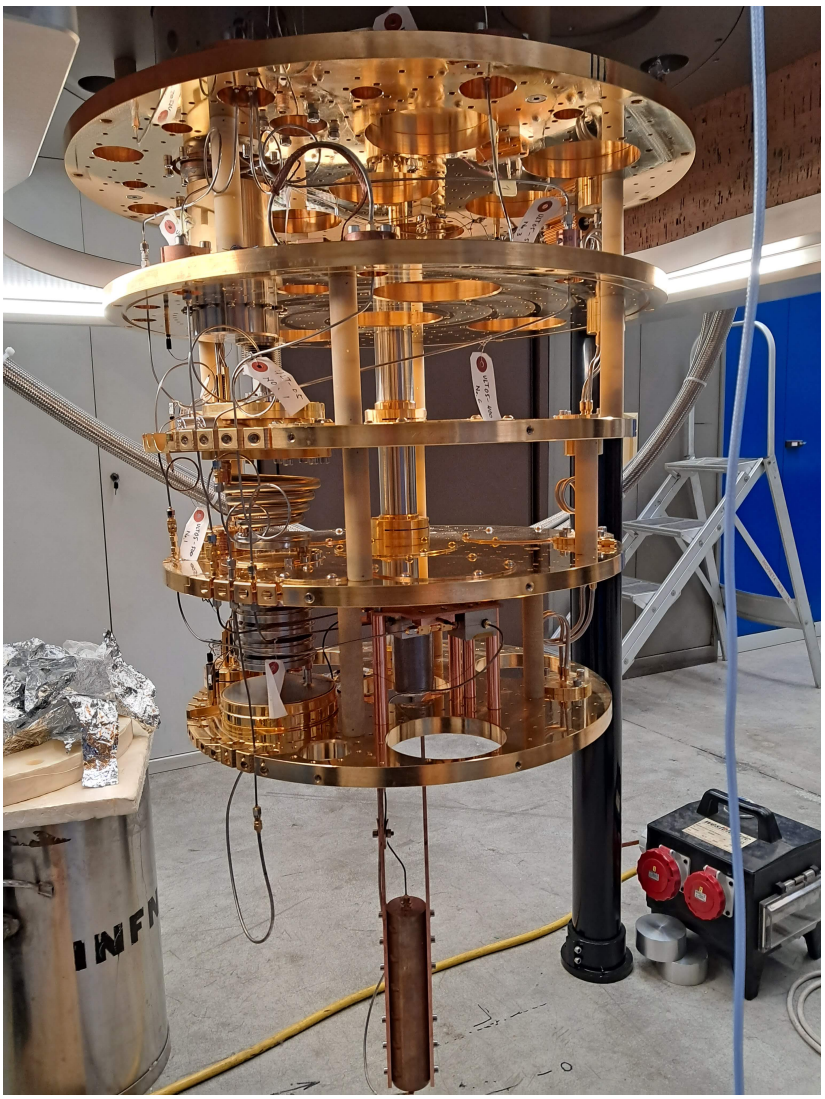

Figure 4.7: Photo of the DR equipped with all the elements of the present experiment.

where c is the speed of light and its factor comes from the Bessel functions, eigenstates of the electromagnetic field inside the cavity. The length of the cavity does not influence its modes frequency, but as we saw in section 2 is important for the scan rate, that is inversely proportional to the cavity volume. The measured frequencies of the first three TM modes at mK temperature are

$$\begin{aligned} f_{TM010} &= 10.4017\,\text{GHz} \\ f_{TM011} &= 10.4418\,\text{GHz} \\ f_{TM012} &= 10.5216\,\text{GHz} \end{aligned} \tag{4.15}$$

.

The cavity, as shown in Fig. 4.7 is placed under the MXC plate, in the centre of the DR, and is connected to the DR by two high RRR copper supports. In this way it can be easily inserted in the magnet coil in future experiments.

The cavity is coupled to the circuit by two antennas positioned in the opposite ends of the cylinder. The antenna connected to the L1 line is weakly coupled while the coupling of the antenna connected to the L2/L3 lines will be measured chapter 5.

4.3 Receivers and electronics

The DR is equipped with 4 microwave lines interconnected and a DC line necessary for the magnetic flux bias of the JPC, as seen in section 3. The microwaves lines are named from L1 to L4 as in Fig. 4.13 and connects the cryocooled elements inside the DR to the room temperature equipment.

- **L1** this line connects the room temperature equipment to the cavity. The coupling to the transmission line is weak as this line is used to inject signals for cavity testing.
- **L2** is the auxiliary line, used to inject signals for test and diagnostic of the receiver line and for noise temperature measurement. It ends with the connection to antenna A1, to which the signal is routed by the circulator C1. At resonance, signals are absorbed by the cavity, while off-resonance they are totally reflected and thus injected to the receiver line.
- **L3** corresponds to the receiver line and is always used as an output line to the external instrumentation. It starts from the cavity antenna A1, passing through two circulators, C1 and C2. The signal travelling in the line is amplified in reflection by the S port of the JPC and sent to the following two HEMTs by passing through circulators C2 and C3
- **L4** is the P pump line, necessary to inject the signal that modulates the JPC internal modes and produces the parametric amplification (see section 3). It is connected to the port P of the JPC

4.3.1 Amplifiers

In the receiver line, the SC parametric amplifier is followed by two FET-based amplifiers, a cryogenic one installed at the 3 K stage if the DR, and an amplifier at room temperature.

HEMT

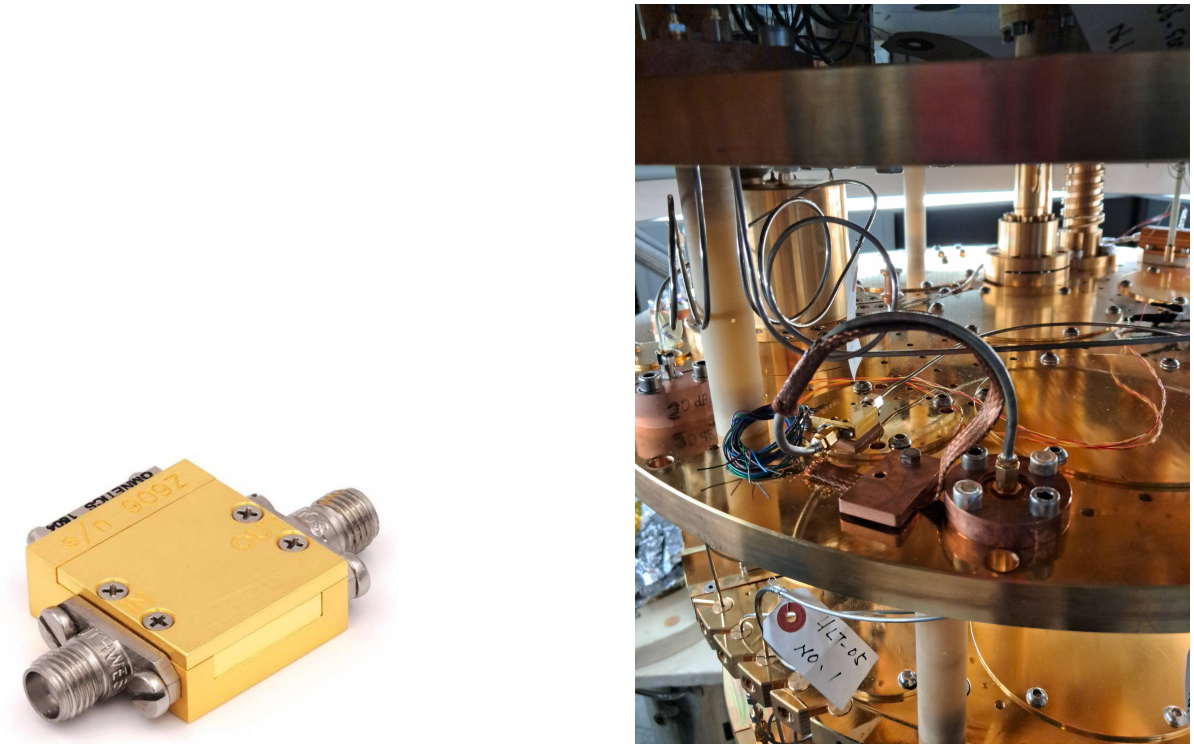

(a) (b)

Figure 4.8: (a) image of the HEMT from LNF (b) Photo of the cryogenic HEMT positioned on the 3K plate

HEMT are field effect transistors (FET) based on an heterojunction, i. e. a PN junction of two materials with different band gaps. Heterojunctions generate high mobility electrons through a highly doped wide-bandgap n-type donor-supply layer like AlGaAs, and a non-doped narrow-bandgap channel layer with no dopant impurities, as GaAs. The n-type layer is depleted by surface trapping of free electrons and by electron transfer into the undoped layer due to its high electron affinity. This

design creates band offsets at the interface, forming a two-dimensional electron gas (2DEG) within a triangular potential well in the conduction band of the undoped side. Thus electrons are confined in a two-dimensional plane parallel to the heterointerface where they can move without colliding with any impurities, enhancing their mobility. This thin layer of highly concentrated and mobile conducting electrons results in a low resistivity channel. The bias voltage applied to the gate shaped as a Schottky barrier diode is used to modulate the number of electrons in the channel formed by the 2D electron gas, consequently controlling the conductivity of the device. As traditional FET the gate bias varies the conductivity by changing the width of the channel. Proper band alignment and doping profile gives rise to extremely high electron mobilities, and therefore to amplifiers with high gain and very low noise temperature at microwave frequencies, making them ideal for the detection of weak microwave signals.

The cryogenic HEMT used in this experiment is a model LNF-LNC4_16C s/n 649B, see Fig 4.8ba, manufactured by Low Noise Factory. Due to its significant power dissipation ($\sim 10\,\mathrm{mW}$), this type of amplifier is typically mounted on the 3K plate, as can be seen in Fig. 4.8bb.

A second HEMT is operated at room temperature, connected externally to L3. In the first run the room temperature HEMT model is a AFS4-00101200-22-10P-4, manufactured by MITEQ, while during the second run it was replaced with a model LNF-LNR4_14C_SV s/n, by Low Noise Factory. All the HEMTs specifics are listed in tab. 4.3

Model	V_{ds}	I_{ds}	G	T_{add}	Bandwidth
LNF-LNC4 16C s/n 649B (at 5 K)	0.7 V	15 mA	42 dB	3.1 K	4-16 GHz
AFS4-00101200-22-10P-4 (at 5 K)	15 V	150 mA	30 dB	195 K	0.1-12 GHz
LNF-LNR4 14C SV s/n (at 5 K)	5 V	60 mA	40 dB	57 K	4-14 GHz

Table 4.3: HEMT amplifier nominal specifics: DC bias voltage and current V_{ds}, I_{ds} , Gain G, added noise temperature T_{add} and amplification bandwidth

JPC

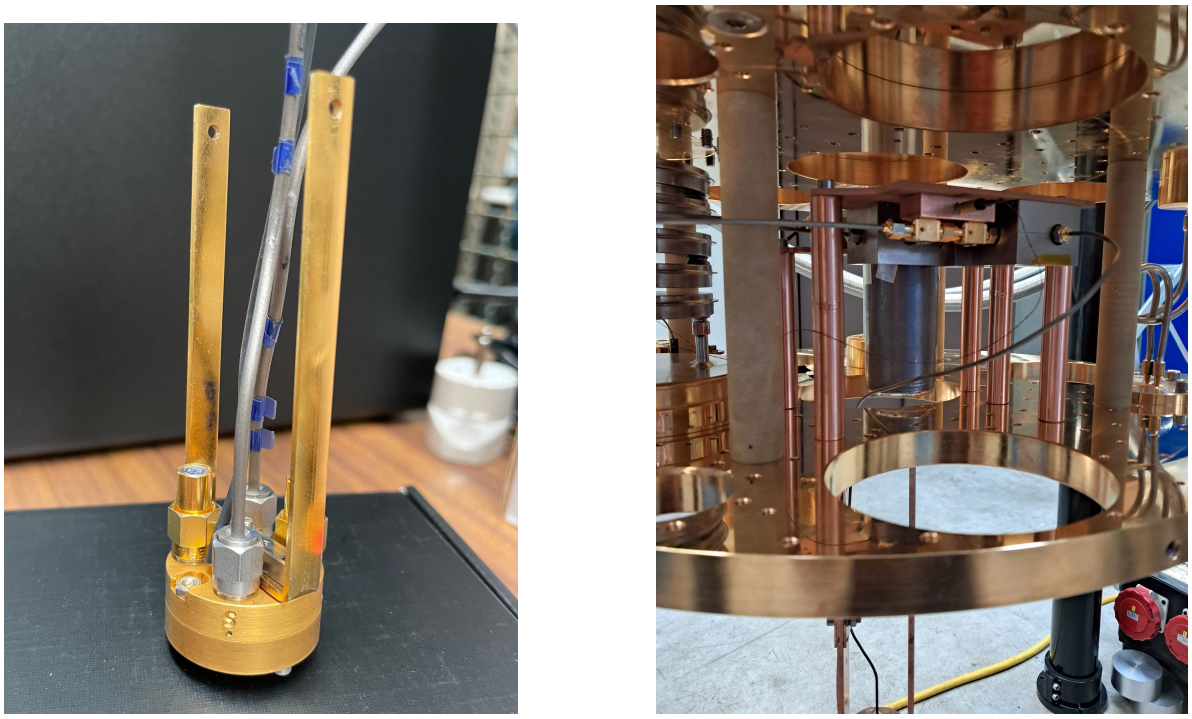

(a) (b)

Figure 4.9: (a) photo of the JPC without external magnetic flux shields (b) Photo of JPC and circulators positioned over the MXC plate.

The parametric amplifier in use for this experiment is a JPC model HF 013 manifactured by Quantum Circuits. It can reach at least 20 dB gain for a signal frequency ranging from 10.62 GHz to 10.241 GHz. At $f = 10.4\,\text{GHz}$ the -1 dB compression point is met at $P(-1\,\text{dB}) = 125 - 128\,\text{dBm}$, over this signal power the amplification behaviour is no more linear and the amplifier is said to saturate. For the same frequency the tabulated bandwidth is $BW = 4\,\text{MHz}$ From the noise point of view, the JPC, practically constituted of non-dissipating elements, can in principle reach the SQL of half a quantum of added noise, that in our case corresponds to a $T_{add,JPC} \sim 0.25\,\text{K}$. In previous realizations [58], this amplifier was measured to have a noise temperature between 0.53 and 0.85 K at 8.46 GHz frequency. The device used in the present work has previously been used as a first stage of a receiver to readout a hybrid magnon-photon system in axion search. The measured noise temperature was 1 K, reaching the SQL [22].

The JPC is screened by the magnetic fields by means of Al,Pb and cryoperm shields. Small amplitude fields can in fact vary the amplification frequency of the signal, shifting the value of the magnetic flux bias. Screening of the SC circuits in multi-Tesla field experiments as those present in haloscope detectors is instead accomplished by vectorially suppressing the stray fields with bucking coils.

Circulators

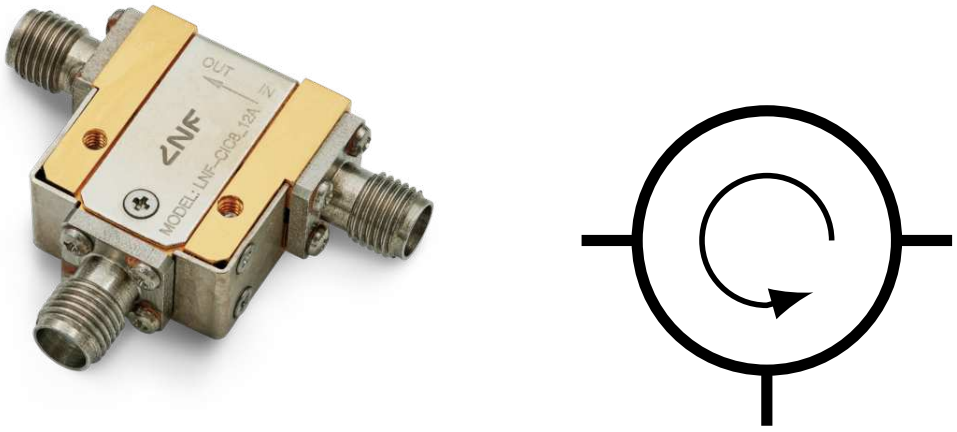

(a) (b)

Figure 4.10: (a) Photo of one of the circulators (b) Scheme symbol of circulators

To isolate the JPC from HEMTs backaction and to route JPC input and output signals to the right lines, three circulators are implemented. Circulators are nonreciprocal three-port devices which rely on the magnetic properties of ferrites to single out a preferred direction. Therefore they allow the passage of the signal with minimal attenuation only towards the next port, depending on the direction in which it acts (in Fig. 4.13 following the direction of the internal arrow). In the other direction, however, the signal is 20 dB attenuated. Different circulators have different frequency ranges on which they can operate optimally, the bigger the circulator, the lower the work frequencies. Measurements at room temperature found an insertion loss of 0.3 dB, that nominally decreases to 0.2 at cryogenic temperatures.

Circulator C1 routes a signal in input to L2 towards the cavity. If the frequency of the signal coincides with one of the cavity modes frequencies, it is absorbed by the cavity, when the antenna is matched to the transmission line. Off-resonance signals are reflected off the cavity port and sent to the JPC. Circulator C2 is used to route the signal amplified in reflection by the JPC to the receiver line. C3 is used as an insulator, since one of its port is terminated with a $50\,\Omega$ resistor, preventing injection of noise by the HEMT stage.

Circulators and JPC are directly connected one with the other, without using any additional cable. Each circulator is enclosed by a magnetic shield which ensures that it does not interfere with other external instruments, such as the JRM of the JPC. In Fig. 4.9b a photo shows the support on which both JPC and circulators are mounted, close to the axis of the cavity so that the geometry of the magnetic field we need to suppress is as simple as possible. The copper support allows to cool down to MXC temperature JPC and circulators. A RuO2 thermometer probe is mounted on it to monitor the amplifier thermalization.

4.3.2 Room temperature equipment

Room temperature instrumentation consists of a vector network analyzer VNA, a signal generator, a spectrum analyzer, a DC current generator to bias the JPC, two other DC generators to bias the HEMTs and a signal generator for the pump tone.

4.4 Equipping the dilution refrigerator

4.4.1 Cabling

Connections inside the DR are all made through three types of semirigid coaxial cables with SMA connectors, manifactured by KEYCOM and designed for cryogenic applications. ULT06 cable materials are cupronickel for the external conductor, foamed PTFE as dielectric and silver plated cupronickel for the internal conductor. Its attenuation per unit length $\alpha(\omega, T)$ at 10 GHz attests its value between 3.7 dB/m at 300 K and 1.49 dB/m at 4 K. We define the cables heat quantity as the heat required for one end of 10 cm long cable to reach 100 K when 4 K heat anchor is applied to the other end, divided by the temperature difference. For ULT06 it has the value of 215 μW/K, therefore this cable shows low insertion loss for a large range of temperatures while maintaining a good heat quantity. These characteristics make it well suited for high temperature plates connections. On the other end the ULT05 cable has lower conductivity and but worse insertion loss, differs from the previous for the copper and stainless steel external conductor and the silver plated brass internal conductor. It has an insertion loss at 10 GHz at 4 K of 1.90 and a heat quantity of 196 μW/K, exploiting the low thermal conductivity of the steel alloy[64].

The total insertion loss of each cable and line is estimated by assuming a uniform temperature gradient on the whole length of the cables, knowing the hot and cold end temperatures T_H and T_C and the length L [23]

$$T(x) = T_H - \frac{(T_H - T_C)}{L} x \tag{4.16}$$

with x the distance of a point in the cable from the hot end.

The insertion loss is then extrapolated at an intermediate temperature between those reported in the data sheet for 300 K, 110 K, 77 K, 20 K and 4 K temperatures, as shown in Fig. 4.11. The insertion loss of the whole cable is calculated through:

$$\Lambda_{ins} = \alpha(\omega, \bar{T}) \cdot L \tag{4.17}$$

with $\bar{T}$ the average temperature of the cable and $\omega/2\pi = 10.4017$ GHz. The temperatures used for the calculation are those obtained in the first commissioning of the DR with $T_{\mathrm{MXC}} = 23$ mK. The results are presented in tab. 4.4.

Line	L1	L2	L3	L4
Total insertion loss (dB)	4.17	3.40	4.17	5.12

Table 4.4: Total insertion loss estimated for each line.

Moreover, to ensure the thermalization of the cables at the CP temperature, an SMA connector with sapphire dielectric has been installed at the cold plate stage to maximise the heat exchange with the internal conductor of the cables.

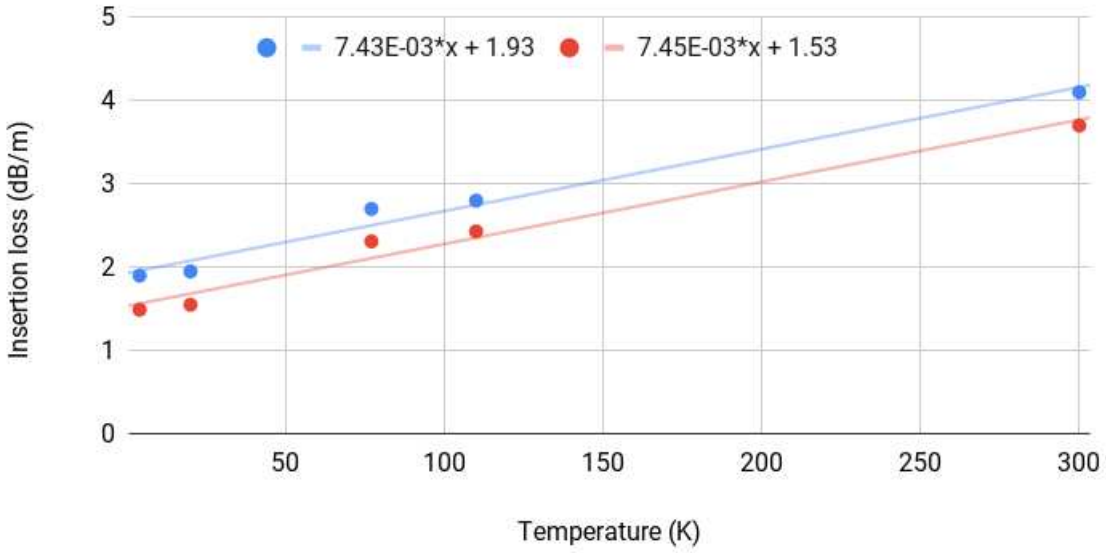

Figure 4.11: Insertion loss temperature dependence fit for ULT05 cable (blue) and ULT06 (red).

Below about 10 K, the NbTi cables used for RF connection under the CP are superconducting and thus allow for decoupling the MC stage from higher temperature plates. In fact in SCs the electrons forming Cooper pairs sit in a lower ground state from the other electrons, separated by an energy gap $\Delta E(T) = 1.76 k_B T_c$, therefore to carry heat they need to separate in normal electrons and jump to the excited states. Only unpaired electron can participate to thermal conductivity, but their number is exponentially dependent on temperature as $\exp(-\Delta E/k_B T)$ and so at sufficiently low temperature $T < T_c/10$ we can safely say that the thermal conductivity of a SC is only due to lattice conductivity, proportional to T^3 as for insulators [53].

In addition, NbTi is a material that tolerates intense magnetic fields when doped with pinning centres. These pinning centres are impurities in the superconductor that trap magnetic fluxes of not too high intensity, penetrating the material, preventing their proliferation and the following return to normal conducting state. In Fig. 4.12 their critical surface is depicted. It's clear that the material can maintain the SC phase for field greater than 9 T, that is the maximum field used until now in axion search.

4.4.2 Thermal photons calculation

Blackbody radiation from higher temperature stages can severely impact both the operation of the DR by preventing to reach base temperature, and add receiver's noise If a coaxial cable has a characteristic impedance R the induced voltage fluctuations $\delta V(t)$ have the following power spectral density:

$$S_V^{th}(T,\omega) = \int_{-\infty}^{+\infty} \mathrm{d}t \langle \delta V(0)\delta V(t)\rangle e^{-i\omega t} = 2R\hbar\omega \frac{1}{\exp(\hbar\omega/k_B T) - 1} \tag{4.18}$$

The last factor in this equation is the photon occupation number given by the Bose-Einstein distribution n_{BE}.

In a coaxial cable connecting room temperature electronics to base temperature circuits, thermal photons propagate down the line towards the lower temperature stages. To reduce the spectral density of thermal radiation attenuators are installed at each temperature stage. An attenuator with an attenuation of $A = 20$ dB $= 100$ effectively acts as a beamsplitter which transmits 1% of the incident signal and adds 99% of blackbody radiation with the effective temperature T_{att} at which the attenuator is thermalized. The noise photon occupation number n_i at stage i with attenuation A_i is given by

$$n_i(\omega) = \frac{n_{i-1}(\omega)}{A_i} + \frac{A_i - 1}{A_i} n_{BE}(T_{i.att}, \omega) \tag{4.19}$$

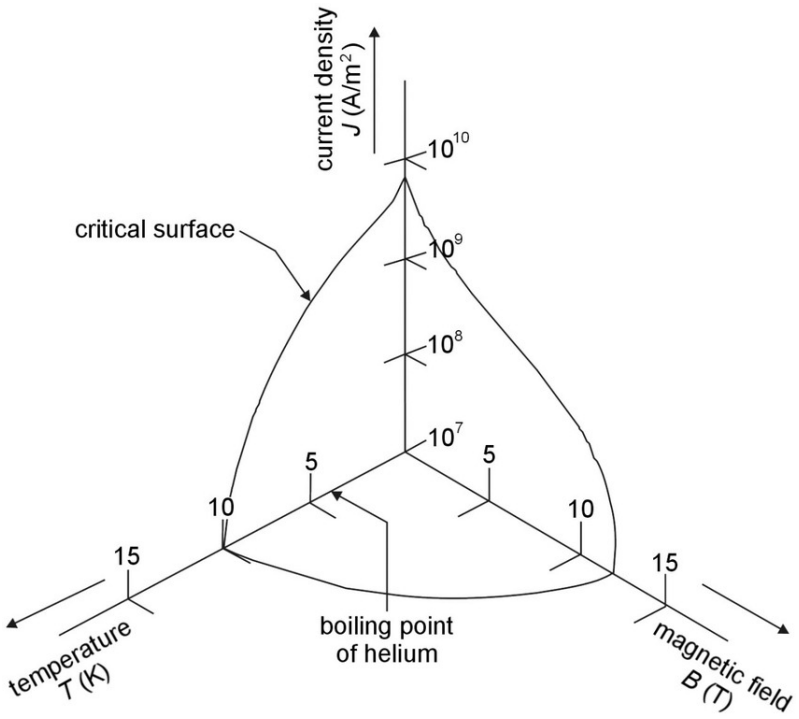

Figure 4.12: Niobium critical surface with respect to temperature, current density and external magnetic field.[33]

When installing a cascade of attenuators in the microwave line thermalized at subsequently lower temperature stages, we employ this relation to determine the noise photon occupation number n_{MXC} at the MXC stage.

The configuration that lowers the most n_{MXC} is to put all the attenuators at the MXC level. However the limited cooling power at this stage (tens of μW) is not compatible with more than 20 dB of attenuation.

The strategy is then to distribute the total attenuation among the various temperature stages to keep the active load on the lower stages well below the cooling powers available at each stage [37]. As a rule of thumb it is not recommended to put more attenuation A_i on stage i than what is needed to thermalize the incoming radiation fields onto that stage[37], i.e. the first term on the r.h.s. of eq. 4.19 should not be significantly smaller than the value to which the second term saturates for A_i. Hence, good reference values for the attenuation on stage i are

$$A_{i,ref} = \frac{n_{BE}(T_{i-1}, \omega)}{n_{BE}(T_i, \omega)}. \tag{4.20}$$

In tab. 4.5 estimates of n_{MXC} in the two different dispositions of attenuators at the 3 K, CP and MXC plates for each line in the present experiment. The frequency considered is the fundamental resonance of the cavity $\omega/2\pi = 10.4$ GHz and for simplicity attenuation in cables has been neglected. The configuration used in the tests named "second run" is clearly better than the "first run".

	First run		Second run	
line	attenuators (3K; CP; MXC)	n° of photons	attenuators (3K; CP; MXC)	n° of photons
L1	(-30 dB; 0; 0)	6.08	(-20 dB; -10 dB; 0)	1.16
L2	(-30 dB; 0; -20 dB)	6.08×10^{-2}	(-12 dB; -10 dB; -20 dB)	4.32×10^{-2}
L4	(-30 dB; 0; -20 dB)	6.08×10^{-2}	(-20 dB; -10 dB; -20 dB)	1.16×10^{-2}

Table 4.5: calculation of number of thermal photons in MXC with different configurations of attenuators

The first run circuit was implemented only for testing the DR with microwave components available in the laboratory, and only later it was possible to mount additional parts that are necessary to ensure a

proper thermalization of the internal coaxial cable conductor, as is the case of the sapphire connectors. In addition, in the second run we installed mainly SC cables at the MXC stage and most importantly we changed the attenuators disposition.

IR filters and eccosorber are also frequantly used in DR systems to prevent the formation of nonequilibrium quasiparticles like unpaired electrons in superconductors, generated by infrared radiation (with frequency above 300 GHz) that enter through coaxial cables and break the Cooper paires, having an energy greater than the SC energy gap. These quasiparticles have a strong influence on the lifetime end decoherence time of qubits but do not play a role in the operation of parametric amplifiers [51], thus we have decided not to install any of them in the present setup. When a photon counting device will be employed to readout the cavity signal, these filtes will be necessary.

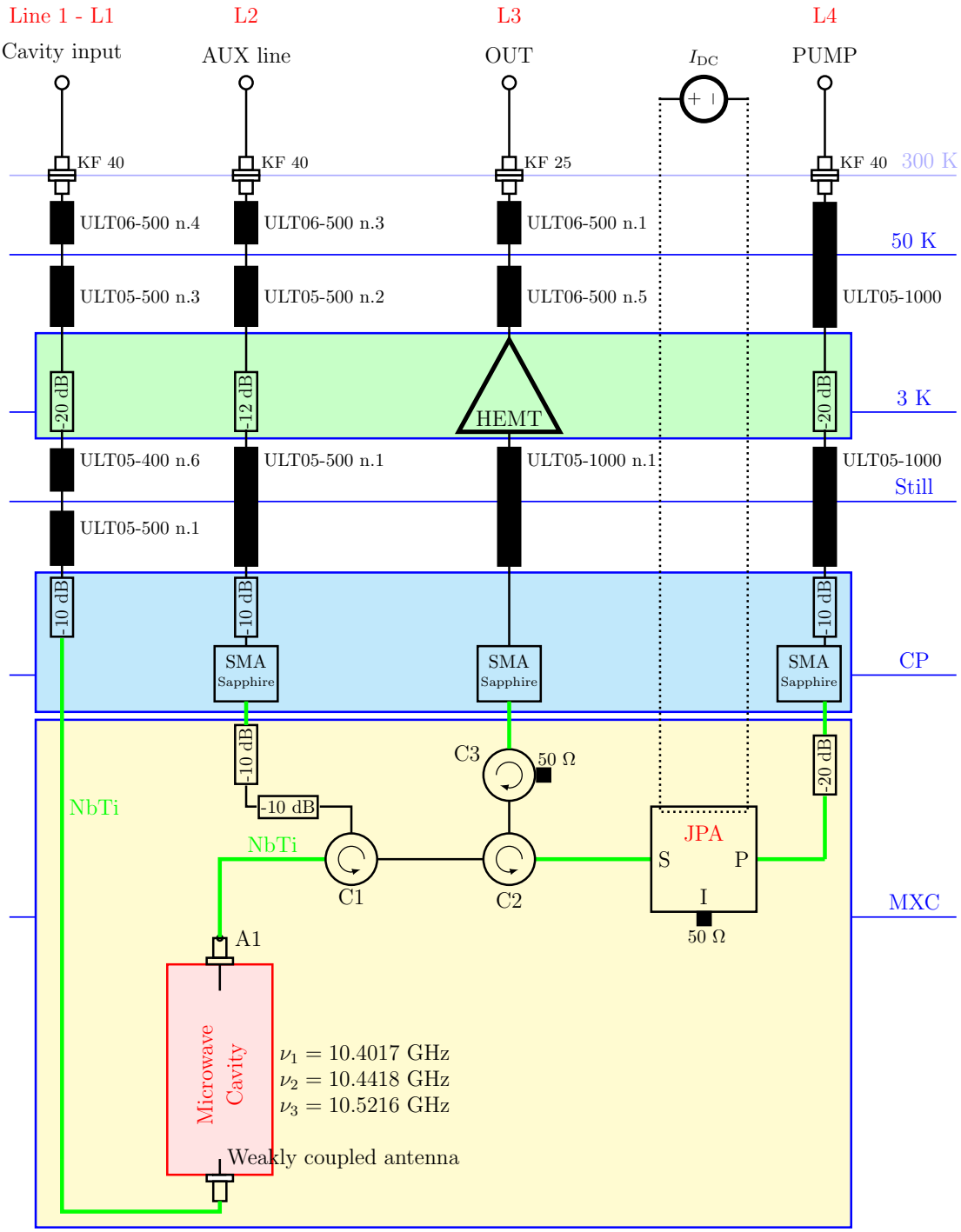

Figure 4.13: DR Lines Scheme: black thin lines represent direct connection, thick ones are coaxial cables, with relative name. Green lines represent SC cables in NbTi. Elements mounted in contact with the MXC have a yellow background, with CP a blue one and in contact with 3K plate have green one. The main cable types used are KEYCOM ULT06 in the warmer part, ULT05 for most of the connections and NbTi cables for connection with the Mixing Chamber plate.

Chapter 5

Measurements and results

The experimental results reported in this section have been obtained during different coolings down of the DR. A first design of the microwave lines was characterized during the experimental runs of July 2023 and October 2023 while the second design was employed in the December 2023 run, that produced interesting results.

The cavity mode of interest, the transverse magnetic TM_{010} is characterized in section 5.1. The parametric Josephson converter tuning and working point characterization methods and results are presented respectively in section 5.2 and 5.3. Finally the system noise temperature measure technique and the relative results are treated in section 5.4

5.1 Cavity characterization

We recall from section 2.1 that a cavity coupled to a transmission line via an antenna has a loaded quality factor Q_L defined as

$$Q_L = \frac{Q_0}{1+\beta} \tag{5.1}$$

where Q_0 is the bare quality factor and β is the coupling factor to the line. For the TM_{010} mode it can be estimated by measuring its transmission curve at a VNA. The source frequency is swept across the cavity resonance, and the transmitted power has a profile that is fitted by a Lorentzian function:

$$L(x) = \frac{A}{\pi}\left(\frac{\Gamma/2}{(x-x_0)^2+(\Gamma/2)^2}\right) \tag{5.2}$$

where A is the intensity scaling, Γ is the FWHM (Full Width at Half Maximum) and x_0 is the peak centre. Thus Q_L corresponds to the ratio between signal peak frequency $f_{peak} = x_0$ and its FWHM (as seen in chp 2?)

$$Q = \frac{f_{peak}}{\Gamma}. \tag{5.3}$$

The quality factor Q_0 and the antenna coupling β for the TM_{010} mode can be derived from the signal in reflection from the cavity by fitting its minimum at resonance with the following function [1]

$$R(\nu; A, \beta, Q_0) = A\frac{(\beta-1)^2 + (Q_0(\nu/\nu_0 - \nu_0/\nu))^2}{(\beta+1)^2 + (Q_0(\nu/\nu_0 - \nu_0/\nu))^2} \tag{5.4}$$

The fit graphS and results are shown in Fig. 5.1a and Fig. 5.1b respectively. For both the measurement we obtain a resonance frequency $f_{TM010} = 10.40167\,\text{GHz}$. The FWHM of the resonance in transmission is $25.0 \pm 0.1\,\text{MHz}$, giving $Q_L = (41,7 \pm 0.2) \times 10^3$, while the parameters obtained by the reflection spectrum fit are $\beta = 1.09 \pm 0.08$ and $Q_0 = (89 \pm 3) \times 10^3$. We can further compare these two measures by calculating Q_L with the results of the second fit. Using eq. 5.1 we obtain $Q_L = (42 \pm 2) \times 10^3$, which is a result in agreement within 0.3σ with the fit value.

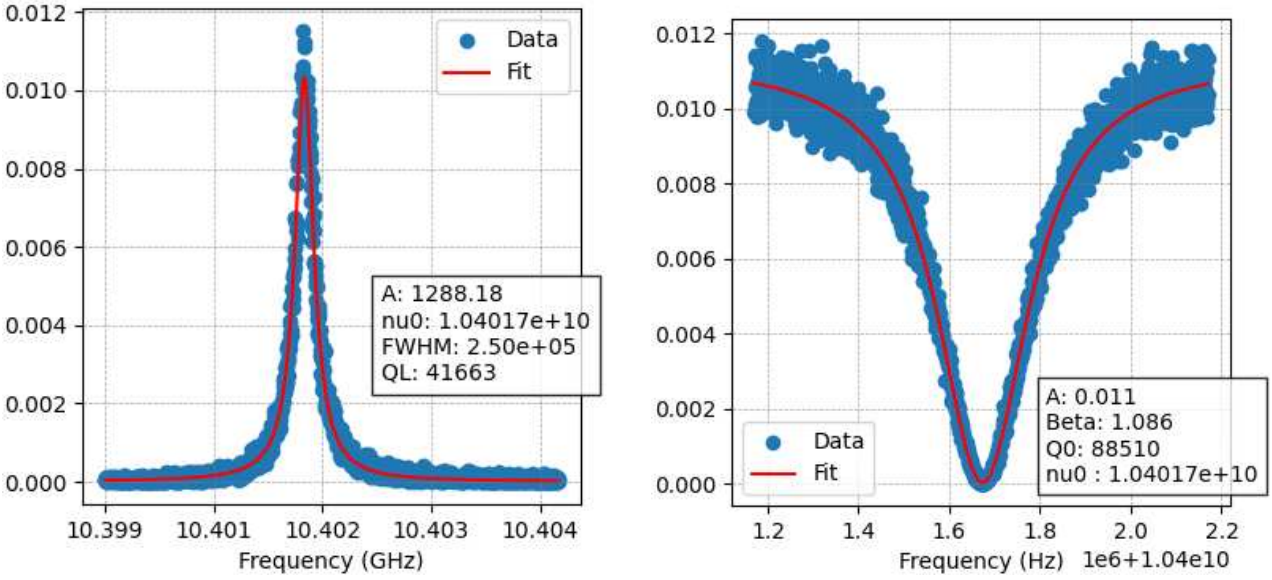

(a) (b)

Figure 5.1: Cavity fits. The measure in transmission (a) is done by injecting a signal with power $P_{in} = -55\,\text{dBm}$ in line L1-L3, with a 100 MHz frequency span and a VNA resolution bandwidth (RBW) of 300 Hz, while for the measure in reflection (b) we inject a power $P_{in} = -50\,\text{dBm}$ in line L2-L3, with a 1 MHz frequency span and RBW of 300 Hz.

5.2 JPC tuning

As detailed in chapter 3, the small gain bandwidth of the JPC requires a fine tuning of the flux bias to center it to the cavity resonance frequency. We describe here the method that has been used to identify the correct settings for its operation, and the characterization that follows once good working points are found. To get amplification at a specific frequency in the given range, we first focus on phase and amplitude maps, that are obtained by changing the flux bias and by recording several reflection spectra over a large frequency span. To do so we vary the bias current I_{bias} that sources the magnetic field threading the JRM (see section 3.4) with the pump tone off. We recall that in a JPC the variation of the flux bias produces a change in frequencies of signal and idler, and thus in the peak frequency of the gain curve of the parametric amplifier. As the bias current is changed, the resonant frequency increases until it hits some maximum value, and then it inverts its trend up to a point where it reaches a minimum. The expected periodicity is observed in the obtained color map, shown in Fig. 5.2. Note that in the amplitude map the structures of help to find the correct setting for the bias current (see section 3.4) are not as clearly seen as in the case of phase maps. In the latter case, the rapid phase change above and under the resonant frequency of the signal resonator is exploited to improve the contrast around the resonance, as shown in Fig. 5.3. The expected arches structures are recognizable, although lacking of the continuous periodicity of wide and narrow lobes visible in Fig. 3.14. The stable and high amplification areas are clearly identified in the phase map.

As reported in the datasheet, amplification with this device can be accomplished in the range from 10.241 GHz to 10.62 GHz. Above this interval the gain is small, while for lower frequencies the amplification is too noisy. Only the big lobes can be used for amplification, since in the small ones the symmetry breaking of the common mode of the JPC doesn't allow for the 3WM process. We observe in both the gain and phase maps sudden jumps that cut the lobes, which are not present in the user guide manual plots. These jumps can be ascribed to poor magnetic shielding condition, even though aging of the circuit might also play a role. The relative position between the JPC and circulators was changed between the first and the second run, and in turn the different amount of magnetic field leaking into the shielding box is at the basis of the observed rigid shift in the maps at Fig. 5.3. As a

rule of thumb, we search for small bias currents to minimize the thermal load on the lower stage, as greater currents would produce more dissipation.

Once the bias current is chosen we can tune the resonator and start to operate the pump parameters, namely its frequency and amplitude. To find the right pump frequency we recall that it has to be equal to the sum of idler and signal frequency to give rise to parametric amplification. Therefore it is necessary to measure the idler resonance at this current bias. It can be directly measured with a phase spectrum in reflection at the idler port or by consulting the datasheet idler phase maps. With the present experimental design with a terminated idler port, we have to rely on the second method. Thus by comparing the measured and the tabulated signal phase maps we identify the lobe structure of the signal and the relative tabulated bias and look for the idler frequency with the same flux modulation on the idler map. To get a rough estimate of the required pump frequency we consider that the idler frequency is approximately 7 GHz therefore the pump should be set at ~ 17 GHz. At this point the pump power can be turned on at ~ -25 dB at the generator and be progressively increased until a marked peak is obtained at the signal analyzer as in the upper graph of Fig. 5.4. Fine tuning of the gain curve amplitude and peak frequency is achieved by varying the bias parameters in small steps.

As shown in tab. 5.1, a number of candidate working points was identified during the experimental tests. We measured the system noise temperature T_{sys} when a sufficiently large gain was obtained and for stable operation of the device.

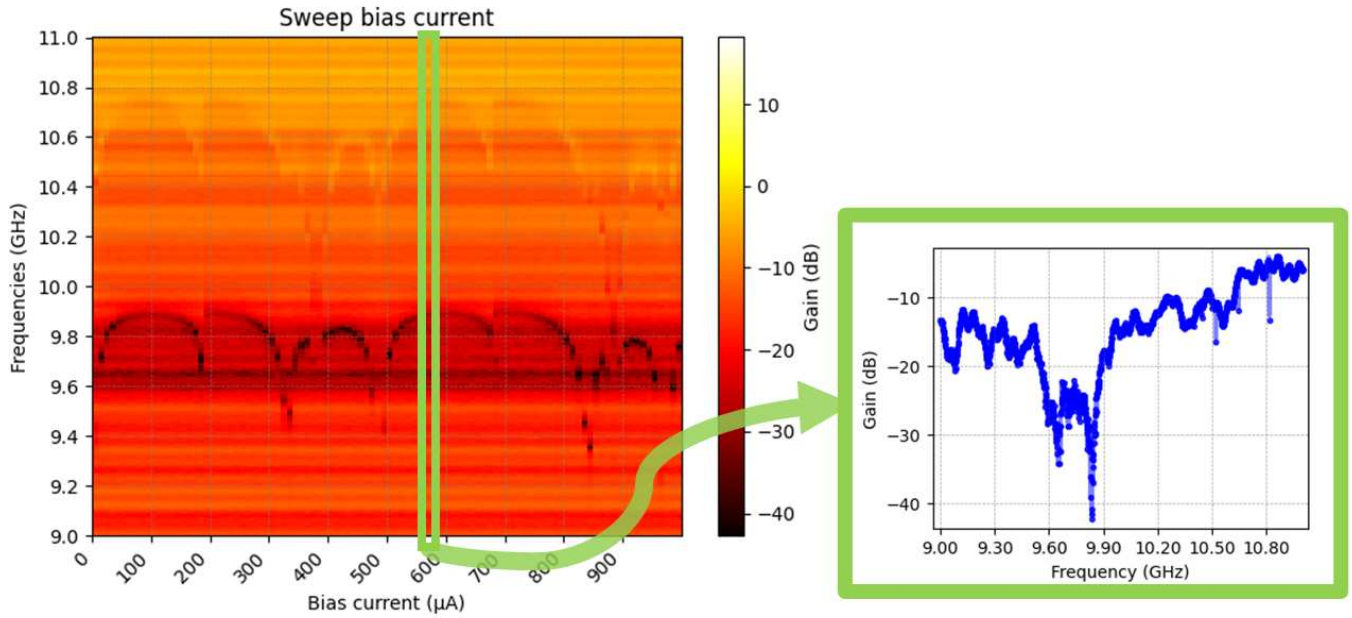

Figure 5.2: The I_{bias} sweep procedure consists in the union of single reflected power spectra of the signal port obtained with a VNA by injecting a power signal in line L1-L3 (an example is shown on the right). The spectrum frequencies span is 3 GHz and the input power is -50 dBm, These are later translated in color depending on the intensity. The final gain map is shown on the left.

	I_{bias} (mA)	f_p (GHz)	P_p (dBm)	T_{sys} (K)	G (dB)	G_{peak} (GHz)
First run	0.5067	17.5066	-9.63		5	- G too low
	-0.0269	17.5039	-10.42	15.3	23	10.4017
	0.075	17.5057	-12.81	5.67	23	10.4017
	0.08155	17.5287	-12.14	11.2	22	10.5217
second run	0.40425	17.50302	-16.02	unstable	20	10.4017
	0.956	17.50488	-16.16	unstable	28.6	10.4017
	0.956	17.50488	-17.5		13	10.5029
	0.959	17.511	-16.6	unstable	24	*
	0.0906	17.9618	-25	2.81	13	10.4022
	0.0906	17.9646	-22	4.49	19	10.4022
	0.0906	17.9656	-19	5.65	21	10.4022
	0.0895	17.9711	-22	2.51	19.7	10.4015
	0.0895	17.9705	-19	3.67	22.3	10.4015

Table 5.1: List of all the bias parameters found during the two experimental runs, The T_{sys} reported are the best measured in each bias condition. *This configuration presents resonant structures that move in frequency when the P_p is increased, instead of increasing their gain.

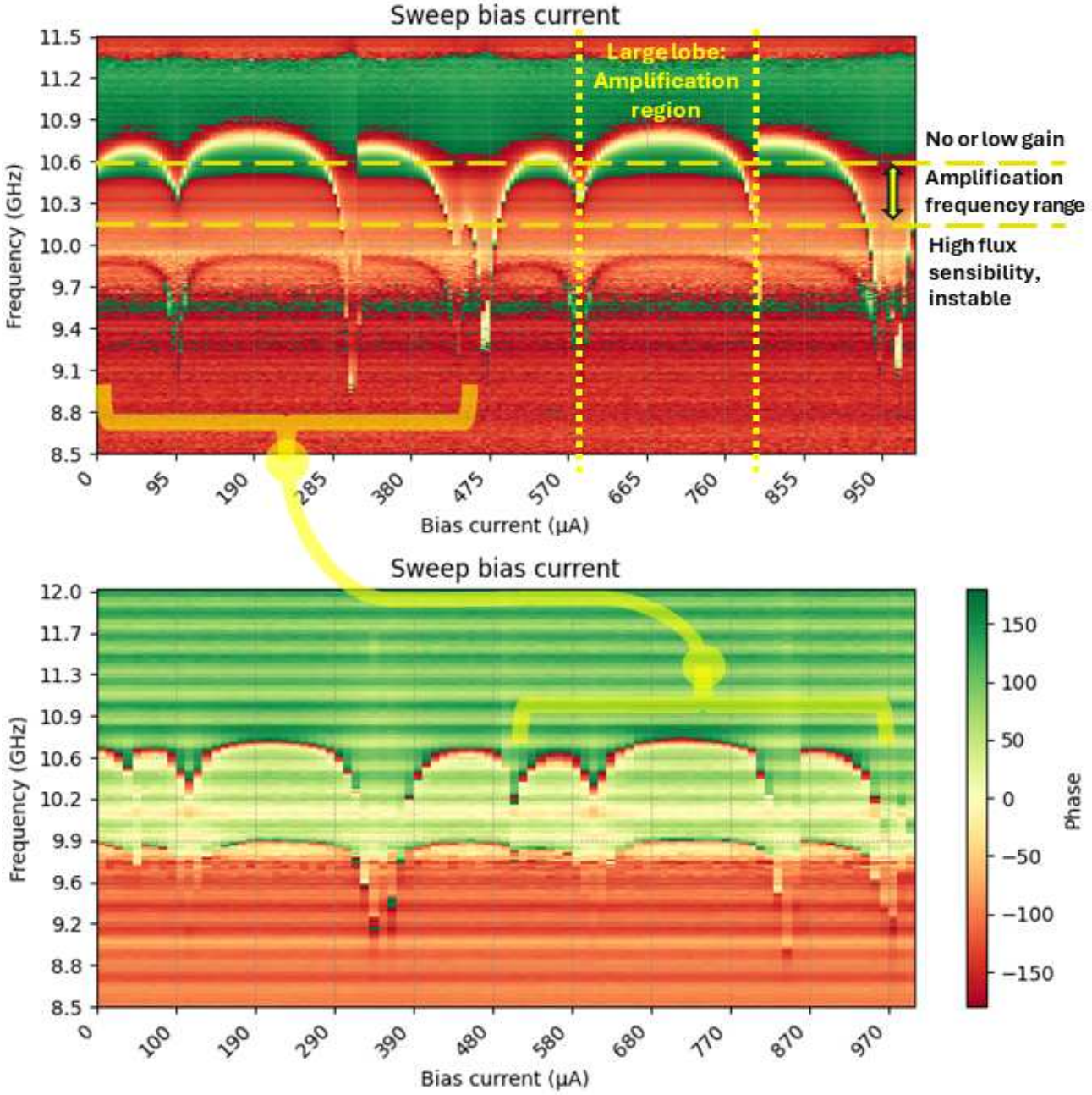

Figure 5.3: Phase maps obtained in different runs, the upper in October and the lower in December. In the upper are shown the interesting amplification areas of the map, in particular the amplification range of frequencies to which the JPC can be tuned. The movement of the lobes structures from one run to the other is indicated by the yellow brackets.

5.3 JPC characterization

We then measure the saturation of the JPC, namely the input power at which the amplification gain starts to decrease. This is accomplished by injecting a signal of power P_{in} in line L2-L3 swept in a range of frequency around the gain peak. The JPC gain is then calculated as the difference between the peak gain obtained with the pump on and with the pump off. Peak gain values are obtained by fitting the pump-on gain curve with a spline function and the pump off with a constant function. As we are only interested to understand the behaviour of each previously identified working point, here we do not evaluate the fit errors. The data for the second working point in tab. 5.1 are reported in Fig. 5.4 with the relative parameters in tab. 5.2. The gain of the JPC for this point saturates for an input value of -55 dBm, where we measure $G \sim 22\,\mathrm{dB}$ while for a smalle signal (-70 dBm) the measured gain is 24 dB Therefore the compression point at the JPC signal port input power, can be estimated at $P(-1\,\mathrm{dB}) = 110\,\mathrm{dBm}$, considering the attenuation in the L2 and in the first part of the L3 lines. If we compare it with the expected tabulated compression point at frequency $\sim 10.4\,\mathrm{GHz}$, $P(-1\,\mathrm{dB}) = 125 - 128\,\mathrm{dBm}$, there's a discrepancy that denotes a bad amplifier behavior. As will be explained in the following, this bias configuration leads to a noisy amplification.

P_{in} (dBm)	$G_{p\,\mathrm{ON}}$	$G_{p\,\mathrm{OFF}}$	G_{JPC}
-70	0.98	-22.99	23.97
-65	0.83	-22.91	23.74
-55	-0.88	-22.85	21.97

Table 5.2: Gains obtained at different input powers by fitting gain curves and background noise in Fig. 5.4. From their difference we calculated the JPC gain to evaluate the saturation of the amplifier

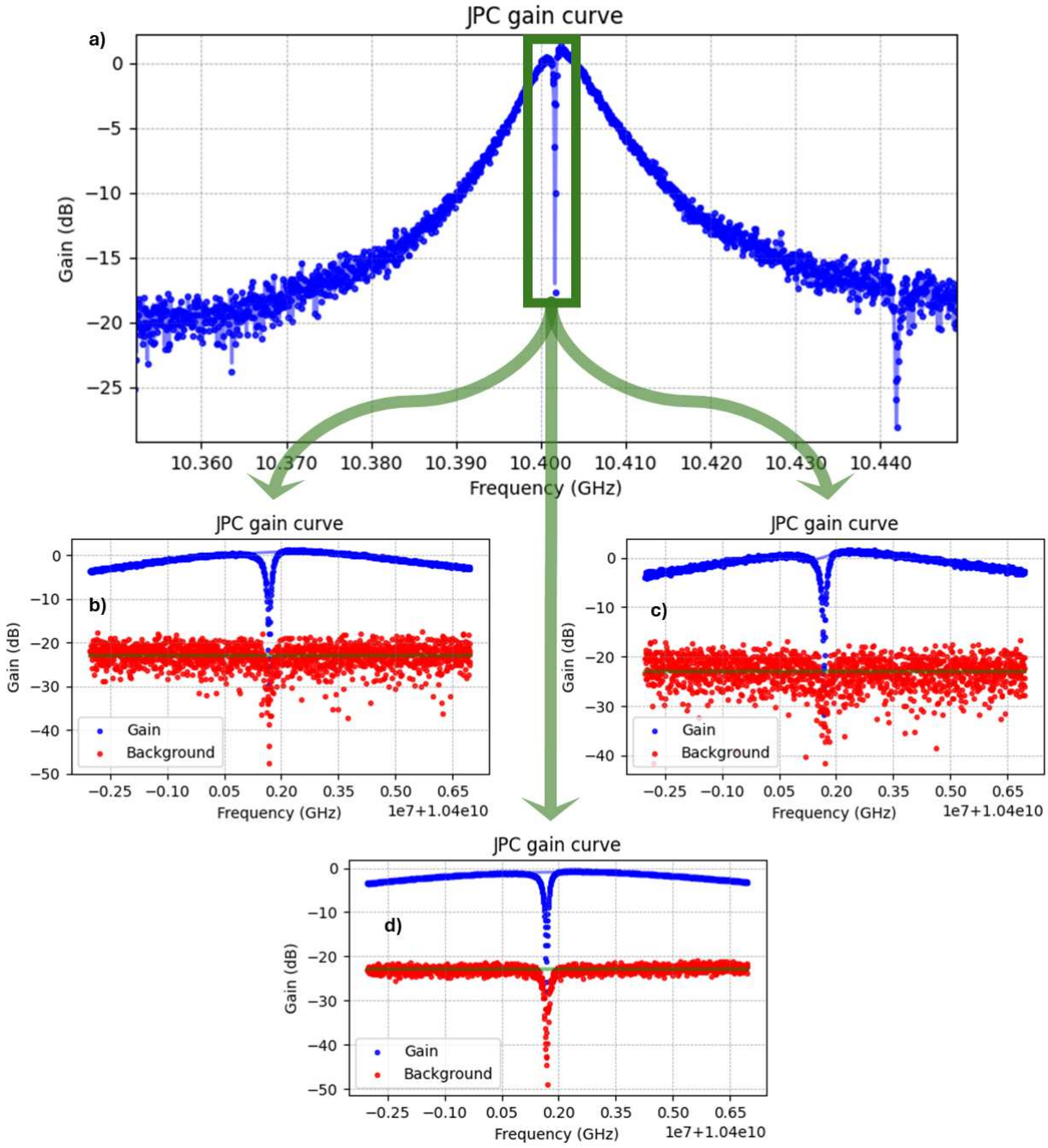

Figure 5.4: (a) gain curve measured at cavity resonant frequency. Lower graphs: gain curves and background noise (measured by turning off the JPC) for different input powers: (b) -70 dBm (c) -65 dBm (d) -55 dBm. gain curves in blue are fitted with spline function, and noise backgrounds in red are fitted with constant function. (d) may present a initial saturation, having a gain smaller than the other cases. The measures are done with a frequencies sweep span of 10 MHz and acquiring the output signal with a VNA with 3kHz resolution bandwidth RBW.

The response of the gain curve to variation in the pump parameters values around the point of maximum gain can give more insights about the working point found. A detuning $\Delta f_p = f_{p,max} - f_p$ of the pump frequency from the maximum gain configuration $f_{p,max}$ should correspond to a variation in the amplified signal frequency of $\Delta f_s \sim \Delta f_p/2$ and a variation in the peak gain inversely dependent on the detuning $G \propto 1/\Delta f_p$. increasing at steps of 10 MHz The gain curves at negative and positive detunings are shown in Fig. 5.5 for $\Delta f_p = n \cdot 10\,\text{MHz}$, with n an integer number. For peak frequencies at the sides of the graph the gain curves lose their lorentzian form and in addition they display multiple peaks. In tab. 5.5 are listed the parameters of the curves obtained by fitting the data with a smooth spline function and the -3 dB bandwidth corresponds to the FWHM in a linear representation. As expected the bandwidth increases with increasing detuning and in turn the gain decreases. Also the signal variation in frequency follows the expected behavior for the small detunings.

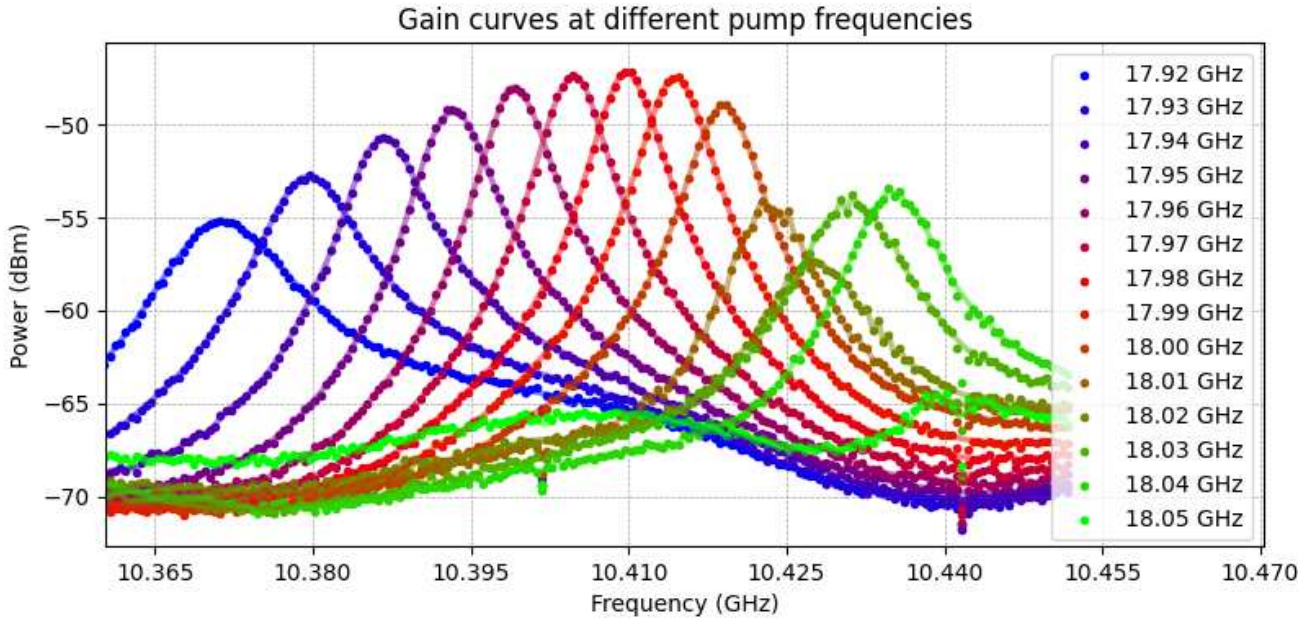

Figure 5.5: Gain curve for different pump frequencies, indicated in the legend. The measures are performed injecting in line L2-L3 a signal input power $P_{in} = -85\,\text{dBm}$ with sweep span of 100 MHz and biasing the JPC at $I_{bias} = 0.0906\,\text{mA}$ and $P_p = -22\,\text{dBm}$.

f_p (GHz)	f_{peak} (GHz)	P_{peak} (dBm)	-3 dB BW (MHz)	G_{JPC} (dBm)	$\sqrt{\text{G}} \times$ BW
17.92	10.37131	-55.17	12.01	9.88	0.037
17.93	10.37962	-52.78	8.61	12.27	0.035
17.94	10.38673	-50.77	6.81	14.28	0.035
17.95	10.39343	-49.33	6.41	15.72	0.039
17.96	10.39914	-47.98	5.41	17.07	0.031
17.97	10.40484	-47.39	5.31	17.66	0.041
17.98	10.40975	-47.16	5.21	17.89	0.041
17.99	10.41435	-47.49	5.41	17.56	0.041
18.00	10.41906	-49.01	5.71	16.04	0.036
18.01	10.42276	-54.16	7.01	10.89	0.025
18.02	10.42797	-57.41	10.21	7.64	0.025
18.03	10.43127	-53.93	8.51	11.12	0.031
18.04	10.43477	-53.58	7.81	11.47	0.029

Table 5.3: Peak frequencies, peak powers and curve bandwidths (at -3 dB form the peak) at different pump powers obtained from fitting the curves in Fig. 5.5. We report also the relative JPC gain and gain-bandwidth product.

Variations in the pump power P_p are expected to increase the JPC gain and slightly move the peak frequency to lower values for the signal, or to higher values for the idler (recall Fig.3.14(a)(b)). The shape of the peak should be similar to a Lorentzian as the gain increases, reducing in turn the bandwidth. In Fig. 5.6 are shown the gain curves for increasing P_p for steps labelled in figure. Data are acquired for an input power exceeding -25 dBm. At -12 dBm the maximum peak value is no longer increasing with pump power and the amplifier is saturated. The last two columns of tables 5.3 and 5.4 are calculated from the fit parameters. JPC gain is calculated as $G_{\text{JPC}} = G_{peak} - G_{peak,\text{OFF}}$ where $G_{peak,\text{OFF}}$ is the peak gain of the pump OFF measure in tab. 5.6. Here we have assumed that the peak value of the pump off gain curve does note significantly vary for different bias condition.

In addition, we verify if the gain-bandwidth relation in eq. 3.14 is satisfied and the results are listed in the last column of both tables. Its average value is $0.04\,\text{Hz}^{-1}$, with a deviation of $0.004\,\text{Hz}^{-1}$ for curves with $G > 10\,\text{dB}$ a quasi-Lorentzian shape. As expected, for lower gain values the gain-bandwidth value is not compatible with the average of the values recorded in the high gain regime. A greater drift is also showed by the $P_p = -12\,\text{dBm}$ measure possibly showing an instability for that bias configuration.

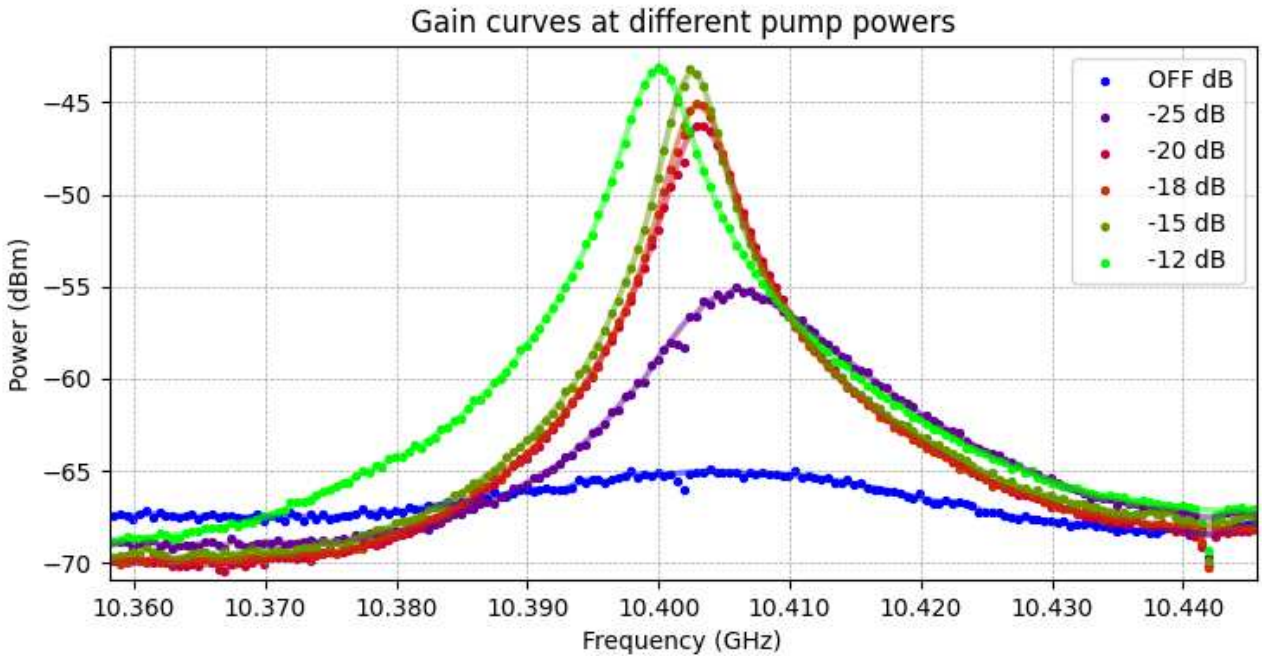

Figure 5.6: Gain curve for different pump powers, indicated in the legend. The measures are performed injecting in line L2-L3 a signal input power $P_{in} = -80\,\text{dBm}$ with sweep span of 100 MHz and biasing the JPC at $I_{bias} = 0.0906\,\text{mA}$ and $f_p = 17.698\,\text{GHz}$. In tab. 5.6 are listed the fit values

P_p (dBm)	f_{peak} (GHz)	P_{peak} (dBm)	-3 dB BW (MHz)	G_{JPC} (dB)	$\sqrt{\text{G}} \times$ BW
-25	10.40595	-55.15	12.31	9.9	0.038
-20	10.40315	-46.24	4.60	18.81	0.040
-18	10.40305	-45.19	4.20	19.86	0.041
-15	10.40265	-43.38	3.60	21.67	0.044
-12	10.40005	-43.23	4.50	21.82	0.055
OFF	10.40365	-65.05			

Table 5.4: Peak frequencies, peak powers and curve bandwidths (at -3 dB form the peak) at different pump powers obtained from fitting the curves in Fig. 5.6. We report also the relative JPC gain and gain-bandwidth product.

An example of low quality working point (second from the top in Tab. 5.1) is shown in Fig. 5.7. In this case we found the high gain and center peak frequency, but variation in the pump power produced

only a change in frequency instead of a change in the peak gain, as shown in Fig. 5.6. Although a slight variation in frequency is expected, the one visible in the figure is too large to be ascribed to the studied parametric amplification process effect.

The high value of noise temperature measured of $T_{sys} \sim 15\,\mathrm{K}$ confirms the hypothesis of instability and noisy behavior. This instability may be sourced by interaction with high order non-linearities present in the JPC circuit [39].

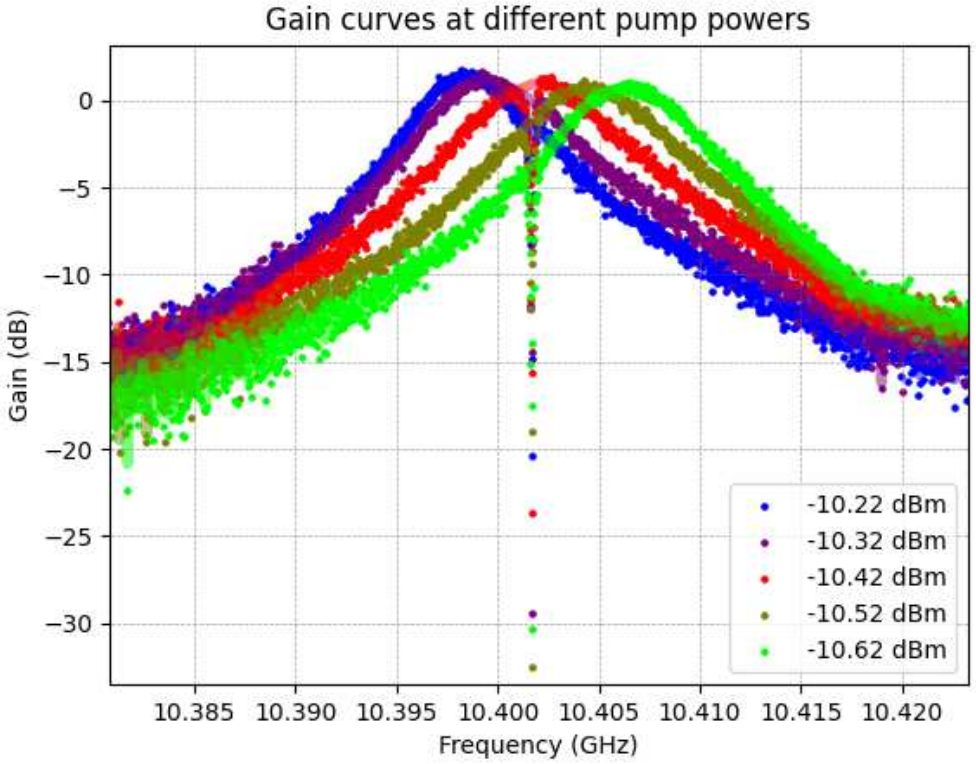

Figure 5.7: Gain curve of first run experiment at different pump powers, indicated in the legend. The important change in frequency of the peak from one power to the other is not expected and can underline a higher order non-linearity that will be unstable for the amplification. The measure are obtained through the VNA injecting a signal $P_{in} = -65\,\mathrm{dBm}$ in line L2-L3 with a frequency span of 50 MHz and acquiring the signal in transmission with a 100 Hz RBW. P_p is changed at steps of 0.10 dBm from -10.22 to -10.62 dBm.

P_p (dBm)	f_{peak} (GHz)	G_{peak} (dBm)	-3 dB BW (MHz)
-10.22	10.39842	1.45	6.16
-10.32	10.39932	1.15	7.41
-10.42	10.40217	1.03	7.66
-10.52	10.40432	0.74	7.76
-10.62	10.40633	0.72	7.31

Table 5.5: Peak frequencies, peak gains and curve bandwidths (at -3 dB form the peak) at different pump powers obtained from fitting the curves in Fig. 5.7

5.4 Noise temperature measurement

The measurement of a receiver noise temperature is typically accomplished with the Y-factor method [54], in which a switch and a calibrated noise need to be included in the electronics scheme. In the

present experiment, we use a method that has been introduced in the QUAX group [22, 13] that makes no use of these additional components. The method is based on measurements of the gains through the different lines in Fig. 4.13 by sending known signals at their inputs and measuring the outputs at a spectrum analyzer.

For the data analyzed in the present section, the temperature of the cavity is measured with a RuO2 thermometer, fixed to the MXC plate, and remained at a stable value $T_c \sim 10\,\mathrm{mK}$

The total gain of a line G_{xy} is the product $g_x \times g_y$ of fractions of the overall line. Referring to the lines description in section 4.3, the gain g_1 corresponds to line L1, g_2 to line L2 and g_3 to line L3 with the addition of the room temperature amplifier, and are calculated as:

$$g_1 = \sqrt{\frac{G_{21}G_{13}}{G_{23}}} \qquad g_2 = \sqrt{\frac{G_{23}G_{21}}{G_{13}}} \qquad g_3 = \sqrt{\frac{G_{13}G_{23}}{G_{21}}}. \tag{5.5}$$

We then measure G_{13}, G_{23} and G_{21} from the transmission power spectra S31, S32 and S21, respectively.

A calibrated signal generator provides as input a pure tone of different power levels P_{in} and the output power levels P_{out} are measured by the spectrum analyzer set to a specific resolution bandwidth B.

$$P_{out}^{xy} = P_n + P_{in} \times G_{xy}, \quad (xy) = \{21, 23, 13\} \tag{5.6}$$

where P_n is the noise power at the spectrum analyzer. A linear fit of the measured values for the three equations (5.6) allows to obtain the three line gains G_{xy} and P_n. The value of g_3, together with g_1 and g_2, is then derived from G_{xy} using eqs. 5.5.

Since G_{xy} and g_x are frequency dependent, the signal generator injects pure tones at the cavity resonance frequency for G_{21} and G_{13}. For G_{23} the signal has to be reflected by the cavity, so the measure is repeated at frequencies detuned above and below the cavity frequency of $f_{detune} = 600\,\mathrm{kHz}$. The final G_{23} value is therefore calculated as an average of the positive and negative detuned measures.

Measures S31 and S32 carry information on g_3, the amplification of the entire receiver chain, and by T_{sys}, the system noise temperature of the detection chain measured at the antenna point A1. The latter is calculated from the formula:

$$P_n^{13} = g_3 k_B T_{sys} B + P_{SA}^n \tag{5.7}$$

that leads to

$$T_{sys} = \frac{P_n^{13} - P_{SA}^n}{g_3 k_B B} \tag{5.8}$$

with B and P_{SA} respectively the resolution bandwidth and the noise floor of the spectrum analyzer. This noise floor is measured $P_{SA} = 100\,\mathrm{fW}$, that is negligible with respect to the noise powers obtained during the measurement operations.

The spectrum analyzer RBW is set to $B = 100\,\mathrm{kHz}$ for all the measures of the spectra S32 and S31. In the case of spectrum S12, in absence of active amplification on this line, the measure of the weak signal requires a smaller RBW of $B = 30\,\mathrm{kHz}$, and therefore a longer acquisition time, producing a smaller noise power. This variation ideally should result only in a shift of the intercept parameter of the fit, leaving the slope parameter that carries the gain informations unchanged, without affecting the noise temperature measures.

5.4.1 Results

In table 5.6 are summarized the collected data for the transmission power spectra S12, S32 and S31 that led to the lowest noise temperature reached during the experimental runs. They are plotted and linearly fitted in Fig. 5.8. Measurements repeated in the exact same conditions give fit parameters that are compatible, also at distance of hours, proving the robustness of the results. Note that for the last five working points reported in tab. 5.1 the measured noise temperature and the JPC gain

P_{in} (dBm)	P_{in} (pW)	P_{out} (nW)
-125	3.2×10^{-4}	0.869
-125	3.2×10^{-4}	0.846
-85	3.16	2.00
-83	5.01	2.84
-81	7.94	4.22
-79	1.26	4.96

(a) L1-L3

P_{in} (dBm)	P_{in} (mW)	P_{out} (fW)
-1	0.794	49.5
0	1.00	49.4
2	1.58	72.1
3	2.00	74.6
5	3.16	97.1
7	5.01	129

(b) L2-L1

P_{in} (dBm)	P_{in} (fW)	P_{out} neg (nW)	P_{out} pos (nW)
-120	1.00	0.713	0.741
-98	158	0.991	1.18
-96	251	1.24	1.32
-94	398	1.53	1.71
-93	501	1.67	1.92
-92	631	1.90	2.11

(c) L2-L3

Table 5.6: Data of the gain measurements for the different lines L1-L3 (a), L2-L1 (b) and L2-L3, with negative and positive frequency detuning (c). This measurement, that led to the lowest noise temperature measured, was performed with bias $P_p = -22\,\mathrm{dBm}$, $I_{bias} = 0.0895\,\mathrm{mA}$ and $f_p = 17.9711\,\mathrm{GHz}$ (second working point from the bottom of Tab. 5.1). The relative linear fits are shown in Fig. 5.8.

increase with pump power. We would instead expect that for higher gains, the noise added by the rest of the receiver chain is smaller.

This may be caused by a not sufficient attenuation and thermalization of the pump line, thus adding thermal noise at the JPC level. Alternatively, we might have operated the amplifier near the compression point for the higher input power data shown in the plot (Fig. 5.8), which would result in a systematic error. In fact, as confirmed by the data reported in table 5.8, the system noise temperature T_{sys} is smaller for low pump powers, and also the error decreases.

To test if the saturation plays a role in the added noise, G_{23} is measured decreasing of $\Delta P_{in} = 5\,\mathrm{dBm}$ all the P_i values necessary for the linear fit. The resulting noise temperature, compared with the previous result at $\Delta P_{in} = 0$ in tab. 5.7, improves for lower input powers, supporting the saturation hypothesis.

ΔP_{in} \ P_p	-19 dB	-22 dB
-5 dBm	$5 \pm 1\,\mathrm{K}$	$3.6 \pm 0.7\,\mathrm{K}$
0 dBm	$5 \pm 1\,\mathrm{K}$	$3.8 \pm 0.8\,\mathrm{K}$

Table 5.7: Comparison of noise temperatures taken at different pump and input powers. ΔP_{in} is the is the shift of all the input power values from those usually used in the linear fit data taking.

A second test is performed by calculating the noise temperature neglecting the highest P_{in} point in the fitting procedure, labeled as "saturation" condition in the following. In tab. 5.8 are shown the fit results for the last working point found (last two rows of tab. 5.1) that exhibited the lower T_{sys}. Together are presented also lines gains g_x, JPC gain G_{JPC} and T_{sys}.

These values are calculated both in the 'normal' case, considering all the data points, and in the 'saturation' condition. JPC gain is calculated as

$$G_{\mathrm{JPC}} = \frac{g_3}{g_{3,\,\mathrm{OFF}}} \tag{5.9}$$

where $g_{3,\mathrm{OFF}}$ is the line gain measured with the pump off. Notice that, in the pump off configuration, the JPC is assumed to be a perfect mirror, adding no losses to the line and thus allowing identify this measure as the system noise with the HEMT as pre-amplifier.

For future tests it would be useful to compare the present results with those obtained with a different method as for instance the Y-factor method, which involves the utilization of a calibrated noise source.

The best noise temperature obtained, together with the line gain g_3 and the JPC gain are

$$T_{sys} = 2.5 \pm 0.2\,\mathrm{K} \qquad g_3 = 83.4 \pm 0.2\,\mathrm{dB} \qquad G_{\mathrm{JPC}} = 20.3 \pm 0.2\,\mathrm{dB}. \tag{5.10}$$

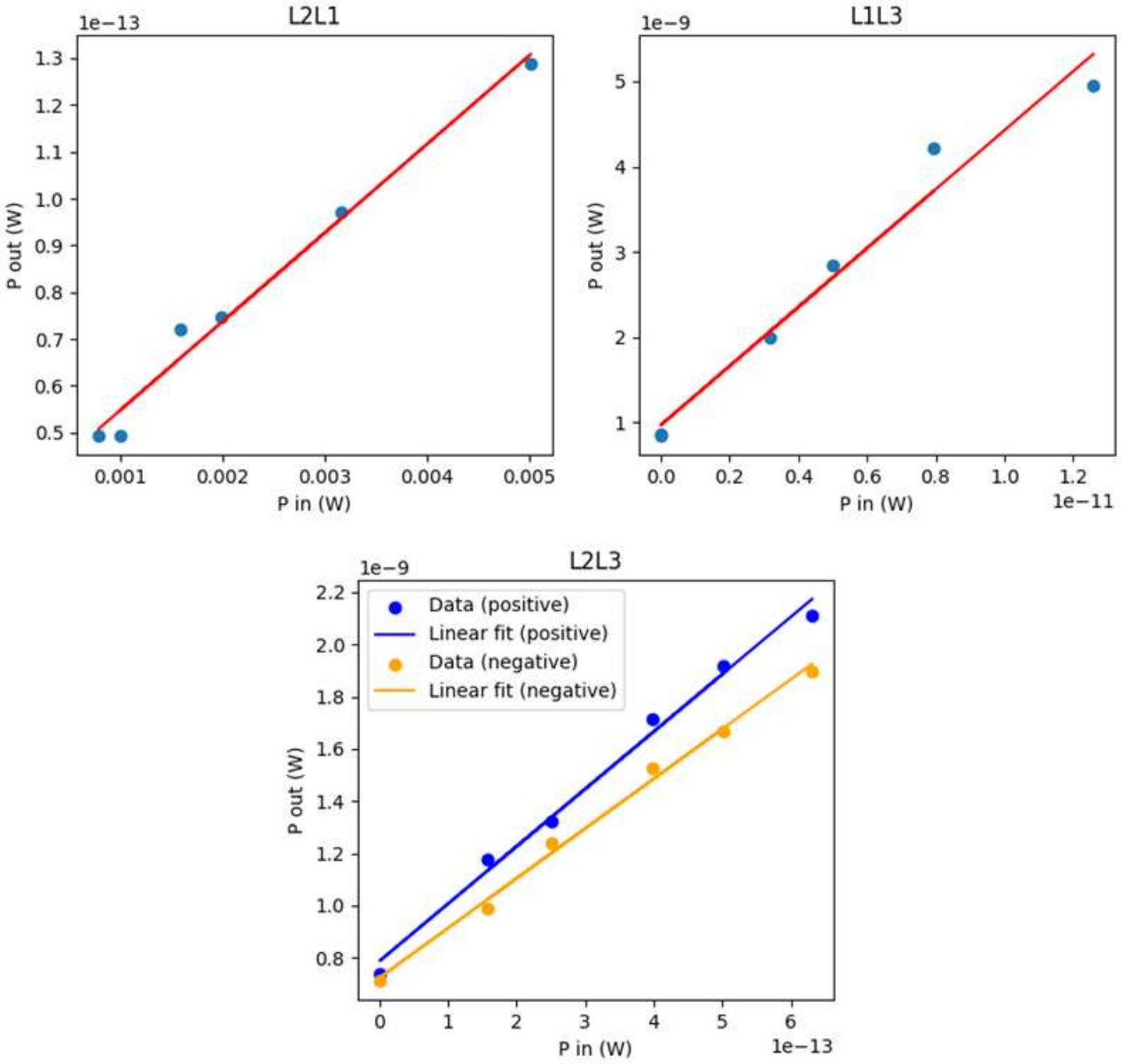

Figure 5.8: Data and linear fits for the T_{sys} calculation of the data shown in tab. 5.6.

We can further estimate the added noise temperature of the JPC $T_{add,\mathrm{JPC}}$ from the system noise temperature formula discussed in chapter 2

$$T_{sys} \approx \frac{hf_{cav}}{2k_B} \coth\left(\frac{hf_{cav}}{2k_B T_{cav}}\right) + \Lambda_1 T_{add}^{\mathrm{JPC}} + \frac{\Lambda_1\Lambda_2}{G_{\mathrm{JPC}}} T_{add}^{\mathrm{HEMT}} \tag{5.11}$$

where the measured cavity temperature is $T_{cav} \sim 10\,\mathrm{mK}$, the cavity frequency is $f_{cav} = f_{010} = 10.4017\,\mathrm{GHz}$, the tabulated cryogenic HEMT amplifier noise temperature is $T_{add}^{\mathrm{HEMT}} \sim 3\,\mathrm{K}$ and the losses from the cavity to the JPC and from the JPC to the HEMT amplifier are respectively $\Lambda_1 = 0.4\,\mathrm{dB}$ and $\Lambda_2 = 2\,\mathrm{dB}$. It's assumed that Λ_1 is due only to circulators and that the gain of the first HEMT amplifier practically suppress the added noise of the rest of the receiver chain. If we compare $T_{add}^{\mathrm{JPC}} \sim 2.03\,\mathrm{K}$ with the expected added noise temperature at SQL at $f_{010} = 10.4017\,\mathrm{GHz}$

$$T_{add}^{SQL} = \frac{hf_{010}}{2k_B} \sim 0.25\mathrm{K}, \tag{5.12}$$

and we assume that the loss introduced by the circulators coincides with the value given by the datasheet, we can infer that the analyzed JPC is seven times noisier than the SQL. As stated in [22],

	-22		-19	
	normal	saturation	normal	saturation
G_{21}	$(1.9 \pm 0.1) \times 10^{-11}$	$(1.9 \pm 0.1) \times 10^{-11}$	$(1.9 \pm 0.1) \times 10^{-11}$	$(1.9 \pm 0.1) \times 10^{-11}$
G_{23}	$(2.05 \pm 0.06) \times 10^{+3}$	$(2.16 \pm 0.07) \times 10^{+3}$	$(3.5 \pm 0.1) \times 10^{+3}$	$(3.4 \pm 0.2) \times 10^{+3}$
G_{13}	$(3.45 \pm 0.3) \times 10^{+2}$	$(4.26 \pm 0.2) \times 10^{+2}$	$(5.77 \pm 0.4) \times 10^{+2}$	$(6.72 \pm 0.2) \times 10^{+2}$
P_n (pW)	1000 ± 200	760 ± 70	2200 ± 500	1800 ± 100
g_1	$(1.8 \pm 0.1) \times 10^{-6}$	$(1.9 \pm 0.1) \times 10^{-6}$	$(1.8 \pm 0.1) \times 10^{-6}$	$(1.9 \pm 0.1) \times 10^{-6}$
g_2	$(1.06 \pm 0.06) \times 10^{-5}$	$(9.8 \pm 0.4) \times 10^{-6}$	$(1.07 \pm 0.05) \times 10^{-5}$	$(9.8 \pm 0.5) \times 10^{-6}$
g_3	$(1.93 \pm 0.1) \times 10^{8}$	$(2.20 \pm 0.09) \times 10^{8}$	$(3.27 \pm 0.2) \times 10^{8}$	$(3.48 \pm 0.2) \times 10^{8}$
T_{sys} (K)	3.6 ± 0.7	2.5 ± 0.2	5 ± 1	3.7 ± 0.3
G_{JPC} (dB)	19.7 ± 0.3	20.3 ± 0.2	22.0 ± 0.3	22.3 ± 0.3

	OFF	
	normal	saturation
G_{21}	$(1.9 \pm 0.1) \times 10^{-11}$	$(1.9 \pm 0.1) \times 10^{-11}$
G_{23}	21.3 ± 0.7	21.2 ± 0.7
G_{13}	3.77 ± 0.03	3.71 ± 0.03
P_n (pW)	27 ± 6	31 ± 4
g_1	$(1.83 \pm 0.09) \times 10^{-6}$	$(1.82 \pm 0.09) \times 10^{-6}$
g_2	$(1.04 \pm 0.04) \times 10^{-5}$	$(1.04 \pm 0.04) \times 10^{-5}$
g_3	$(2.06 \pm 0.08) \times 10^{6}$	$(2.04 \pm 0.07) \times 10^{6}$
T_{sys} (K)	9 ± 2	11 ± 1

Table 5.8: Fit parameters, lines gains g_x, system noise temperatures and JPC gain for best working point, at different pump powers and comparing the normal and saturation conditions

this parametric amplifier in its past operations reached the SQL, allowing for $T_{sys} = 1\,\mathrm{K}$ for readouts of a cavity in the same frequency range. This bad behaviour might be ascribed to a rather typical problem of aging in SC circuit. In addition we do not exclude that the thermalization and degree of attenuation through the RF lines could be further improved.

As shown in tab. 2.1, the added noise temperature of this JPC is lower than that the best commercially available HEMT amplifier ($T_{add} \sim 3\,\mathrm{K}$) for frequencies around 10.4 GHz.

Conclusions

In this thesis work I have characterized a low noise receiver chain devised for future axion dark matter searches. The amplification chain is based on a Josephson parametric converter that via a three wave mixing mechanism pre-amplifies the signal from a microwave 3D resonant cavity, mounted at the lowest stage of a dilution refrigerator to minimize the thermal photon occupation number of its axion-sensitive mode.

The cavity resonator is a pill box cavity with fundamental mode at 10.4017 GHz frequency, with a quality factor $Q_0 = (89 \pm 3) \times 10^3$, critically coupled to the receiver line. When a superconducting magnet will be installed in the dilution refrigerator, the system will be ready to probe for axions at around 10.4 GHz, corresponding to a mass of $\sim 43\,\mu$eV.

A thorough characterization of the four RF lines mounted in the dilution refrigerator was done during this thesis work, as it is crucial to choose the correct components to reach base temperature operation. Note that a temperature of 10 mK will be required when all the RF lines necessary for future photon counting experiments will be installed. Lines have been carefully designed to maximize their thermalization at the various DR levels and to minimize the thermal photon population at the mixing chamber plate. To accomplish these tasks, I studied in depth the optimal attenuators disposition and estimated the various lines losses, in particular those ascribable to coaxial cables.

As Josephson parametric amplifiers have a narrow bandwidth (~ 100 MHz), it is sometimes not straightforward to get optimal operation at the desired frequency. In the present case I had to identify a good working point at the 3D resonator frequency. This entails finding the correct bias flux current, and frequency and power of the pump field. We started by finding the correct JPC bias, based on the working point stability and gain peak at the cavity frequency. Best results were obtained for JPC parameters that gave an overall receiver chain gain of (83.4 ± 0.2) dB and system noise temperature of (2.5 ± 0.2) K.

During the tests, I observed a slight dependence of the noise temperature on the pump power, that could be ascribed to saturation of the JPC, even though the chosen input values were not far above the expected saturation point. In successive tests with lower input power the measured system noise temperature was slightly better, but this issue is certainly worth further study. The JPC gain and added noise were estimated as $G_{\mathrm{JPC}} = 20.3 \pm 0.2$ dB and $T_{add,\mathrm{JPC}} = 2.03$ K, seven times as much the SQL. Compared to the results obtained with this device a few years ago [22], its noise performance degraded, as at the time it was possible to reach SQL operation with a measured overall system noise temperature of ~ 1 K (with added noise of 0.25 K). This bad behaviour might be probably due to aging of the SC circuit. Further tests will however be soon conducted with a different method to measure the system noise temperature, namely using a noise source made available by collaborators at NIST, Colorado.

Bibliography

[1] D. Alesini. *Power coupling*. 2011. arXiv: 1112.3201 [physics.acc-ph].

[2] S. J. Asztalos et al. "SQUID-Based Microwave Cavity Search for Dark-Matter Axions". In: *Physical Review Letters* 104.4 (Jan. 2010). ISSN: 1079-7114. DOI: 10.1103/physrevlett.104.041301. URL: http://dx.doi.org/10.1103/PhysRevLett.104.041301.

[3] Jose Aumentado. "Superconducting Parametric Amplifiers: The State of the Art in Josephson Parametric Amplifiers". In: *IEEE Microwave Magazine* 21.8 (Aug. 2020). [Online; accessed 2024-03-11], pp. 45–59.

[4] Adrian Ayala et al. "Revisiting the Bound on Axion-Photon Coupling from Globular Clusters". In: *Physical Review Letters* 113.19 (Nov. 2014). ISSN: 1079-7114. DOI: 10.1103/physrevlett.113.191302. URL: http://dx.doi.org/10.1103/PhysRevLett.113.191302.

[5] Horace W. Babcock. "The rotation of the Andromeda Nebula". In: *Lick Observatory Bulletin* 498 (Jan. 1939), pp. 41–51. DOI: 10.5479/ADS/bib/1939LicOB.19.41B.

[6] K. M. Backes et al. "A quantum enhanced search for dark matter axions". In: *Nature* 590.7845 (Feb. 2021), pp. 238–242. ISSN: 1476-4687. DOI: 10.1038/s41586-021-03226-7. URL: http://dx.doi.org/10.1038/s41586-021-03226-7.

[7] R Barbieri et al. "Axion to magnon conversion. A scheme for the detection of galactic axions". In: *Physics Letters B* 226.3 (1989), pp. 357–360. ISSN: 0370-2693. DOI: https://doi.org/10.1016/0370-2693(89)91209-4. URL: https://www.sciencedirect.com/science/article/pii/0370269389912094.

[8] Jacob Beckey, Daniel Carney, and Giacomo Marocco. *Quantum measurements in fundamental physics: a user's manual*. 2023. arXiv: 2311.07270 [hep-ph].

[9] N. Bergeal et al. "Analog information processing at the quantum limit with a Josephson ring modulator". In: *Nature Physics* 6.4 (Feb. 2010). [Online; accessed 2024-03-11], pp. 296–302.

[10] N. Bergeal et al. "Phase-preserving amplification near the quantum limit with a Josephson ring modulator". In: *Nature* 465.7294 (May 2010). [Online; accessed 2024-03-11], pp. 64–68.

[11] Robert W. Boyd. *Nonlinear Optics*. [Online; accessed 2024-03-11]. Elsevier, Jan. 2003.

[12] C. Braggio et al. *Quantum-enhanced sensing of axion dark matter with a transmon-based single microwave photon counter*. 2024. arXiv: 2403.02321 [quant-ph].

[13] Caterina Braggio et al. "A haloscope amplification chain based on a traveling wave parametric amplifier". In: *Review of Scientific Instruments* 93.9 (Sept. 2022). ISSN: 1089-7623. DOI: 10.1063/5.0098039. URL: http://dx.doi.org/10.1063/5.0098039.

[14] Benjamin M. Brubaker. *First results from the HAYSTAC axion search*. 2018. arXiv: 1801.00835 [astro-ph.CO].

[15] Dmitry Budker et al. "Proposal for a Cosmic Axion Spin Precession Experiment (CASPEr)". In: *Phys. Rev. X* 4 (2 May 2014), p. 021030. DOI: 10.1103/PhysRevX.4.021030. URL: https://link.aps.org/doi/10.1103/PhysRevX.4.021030.

[16] David C. Burnham and Donald L. Weinberg. "Observation of Simultaneity in Parametric Production of Optical Photon Pairs". In: *Physical Review Letters* 25.2 (July 1970). [Online; accessed 2024-03-11], pp. 84–87.

[17] Carlton M. Caves. "Quantum limits on noise in linear amplifiers". In: *Phys. Rev. D* 26 (8 Oct. 1982), pp. 1817–1839. DOI: 10.1103/PhysRevD.26.1817. URL: https://link.aps.org/doi/10.1103/PhysRevD.26.1817.

[18] *CF-CS110 Series - Leiden Cryogenics*. leidencryogenics.nl/cf-cs110-series/. [Online; accessed 2024-03-14]. Mar. 2022.

[19] Francesca Chadha-Day, John Ellis, and David J. E. Marsh. "Axion dark matter: What is it and why now?" In: *Science Advances* 8.8 (2022), eabj3618. DOI: 10.1126/sciadv.abj3618. eprint: https://www.science.org/doi/pdf/10.1126/sciadv.abj3618. URL: https://www.science.org/doi/abs/10.1126/sciadv.abj3618.

[20] Raymond T. Co and Keisuke Harigaya. "Axiogenesis". In: *Physical Review Letters* 124.11 (Mar. 2020). ISSN: 1079-7114. DOI: 10.1103/physrevlett.124.111602. URL: http://dx.doi.org/10.1103/PhysRevLett.124.111602.

[21] HAYSTAC Collaboration et al. *New Results from HAYSTAC's Phase II Operation with a Squeezed State Receiver*. 2023. arXiv: 2301.09721 [hep-ex].

[22] N. Crescini et al. "Axion Search with a Quantum-Limited Ferromagnetic Haloscope". In: *Physical Review Letters* 124.17 (May 2020). [Online; accessed 2024-03-12].

[23] Sergey Danilin et al. "Engineering the microwave to infrared noise photon flux for superconducting quantum systems". In: *EPJ Quantum Technology* 9.1 (Jan. 2022). ISSN: 2196-0763. DOI: 10.1140/epjqt/s40507-022-00121-6. URL: http://dx.doi.org/10.1140/epjqt/s40507-022-00121-6.

[24] Luca Di Luzio et al. "The landscape of QCD axion models". In: *Physics Reports* 870 (July 2020), pp. 1–117. ISSN: 0370-1573. DOI: 10.1016/j.physrep.2020.06.002. URL: http://dx.doi.org/10.1016/j.physrep.2020.06.002.

[25] R. H. Dicke. "The Measurement of Thermal Radiation at Microwave Frequencies". In: *Review of Scientific Instruments* 17.7 (July 1946), pp. 268–275. ISSN: 0034-6748. DOI: 10.1063/1.1770483. eprint: https://pubs.aip.org/aip/rsi/article-pdf/17/7/268/19120701/268_1_online.pdf. URL: https://doi.org/10.1063/1.1770483.

[26] Michael Dine, Willy Fischler, and Mark Srednicki. "A simple solution to the strong CP problem with a harmless axion". In: *Physics Letters B* 104.3 (1981), pp. 199–202. ISSN: 0370-2693. DOI: https://doi.org/10.1016/0370-2693(81)90590-6. URL: https://www.sciencedirect.com/science/article/pii/0370269381905906.

[27] Emmanuel Flurin. "The Josephson mixer : a swiss army knife for microwave quantum optics". Theses. Ecole normale supérieure - ENS PARIS, Dec. 2014. URL: https://theses.hal.science/tel-01241123.

[28] Kristian Fossheim and Asle Sudboe. *Superconductivity: Physics and Applications*. [Online; accessed 2024-03-11]. John Wiley and Sons, Sept. 2005.

[29] J. Goldstone. "Field Theories with Superconductor Solutions". In: *Nuovo Cim.* 19 (1961), pp. 154–164. DOI: 10.1007/BF02812722.

[30] Eleanor Graham et al. *Rydberg-atom-based single-photon detection for haloscope axion searches*. 2023. arXiv: 2310.15352 [hep-ex].

[31] Peter W. Graham et al. "Experimental Searches for the Axion and Axion-Like Particles". In: *Annual Review of Nuclear and Particle Science* 65.Volume 65, 2015 (2015), pp. 485–514. ISSN: 1545-4134. DOI: https://doi.org/10.1146/annurev-nucl-102014-022120. URL: https://www.annualreviews.org/content/journals/10.1146/annurev-nucl-102014-022120.

[32] H. A. Haus and J. A. Mullen. "Quantum Noise in Linear Amplifiers". In: *Phys. Rev.* 128 (5 Dec. 1962), pp. 2407–2413. DOI: 10.1103/PhysRev.128.2407. URL: https://link.aps.org/doi/10.1103/PhysRev.128.2407.

[33] M. Haverkamp. "Decay and snapback in superconducting accelerator magnets". PhD thesis. Twente U., Enschede, 2003.

[34] *How Does a Dilution Refrigerator Work?* https://bluefors.com/stories/ how-does-a-dilution-refrigerator-work/. [Online; accessed 2024-03-14]. Feb. 2023.

[35] B.D. Josephson. "Possible new effects in superconductive tunnelling". In: *Physics Letters* 1.7 (July 1962). [Online; accessed 2024-03-11], pp. 251–253.

[36] P. Krantz et al. "A quantum engineer's guide to superconducting qubits". In: *Applied Physics Reviews* 6.2 (June 2019).

[37] S. Krinner et al. "Engineering cryogenic setups for 100-qubit scale superconducting circuit systems". In: *EPJ Quantum Technology* 6.1 (May 2019). ISSN: 2196-0763. DOI: 10.1140/epjqt/s40507-019-0072-0. URL: http://dx.doi.org/10.1140/epjqt/s40507-019-0072-0.

[38] S. K. Lamoreaux et al. "Analysis of single-photon and linear amplifier detectors for microwave cavity dark matter axion searches". In: *Phys. Rev. D* 88 (3 Aug. 2013), p. 035020. DOI: 10.1103/PhysRevD.88.035020. URL: https://link.aps.org/doi/10.1103/PhysRevD.88.035020.

[39] G. Liu et al. "Josephson parametric converter saturation and higher order effects". In: *Applied Physics Letters* 111.20 (Nov. 2017), p. 202603. ISSN: 0003-6951. DOI: 10.1063/1.5003032. eprint: https://pubs.aip.org/aip/apl/article-pdf/doi/10.1063/1.5003032/13454231/202603_1_online.pdf. URL: https://doi.org/10.1063/1.5003032.

[40] Simanovskaia Maria. "Design, Fabrication, and Characterization of a High-Frequency Microwave Cavity for HAYSTAC". PhD thesis. University of California Berkeley, 2019.

[41] Richard Massey, Thomas Kitching, and Johan Richard. "The dark matter of gravitational lensing". In: *Reports on Progress in Physics* 73.8 (July 2010), p. 086901. ISSN: 1361-6633. DOI: 10.1088/0034-4885/73/8/086901. URL: http://dx.doi.org/10.1088/0034-4885/73/8/086901.

[42] Yoichiro Nambu. "Axial Vector Current Conservation in Weak Interactions". In: *Phys. Rev. Lett.* 4 (7 Apr. 1960), pp. 380–382. DOI: 10.1103/PhysRevLett.4.380. URL: https://link.aps.org/doi/10.1103/PhysRevLett.4.380.

[43] H. Nyquist. "Thermal Agitation of Electric Charge in Conductors". In: *Phys. Rev.* 32 (1 July 1928), pp. 110–113. DOI: 10.1103/PhysRev.32.110. URL: https://link.aps.org/doi/10.1103/PhysRev.32.110.

[44] Hasan Padamsee, Jens Knobloch, and Tomas Hays. *RF Superconductivity for Accelerators*. [Online; accessed 2024-03-11]. Wiley-VCH, Feb. 2008.

[45] Daniel Palken. "Enhancing the scan rate for axion dark matter: Quantum noise evasion and maximally informative analysis". PhD thesis. Boulder, May 2020, p. 325.

[46] R. D. Peccei and Helen R. Quinn. "CP Conservation in the Presence of Pseudoparticles". In: *Phys. Rev. Lett.* 38 (25 June 1977), pp. 1440–1443. DOI: 10.1103/PhysRevLett.38.1440. URL: https://link.aps.org/doi/10.1103/PhysRevLett.38.1440.

[47] R. D. Peccei and Helen R. Quinn. "Constraints imposed by CP conservation in the presence of pseudoparticles". In: *Phys. Rev. D* 16 (6 Sept. 1977), pp. 1791–1797. DOI: 10.1103/PhysRevD.16.1791. URL: https://link.aps.org/doi/10.1103/PhysRevD.16.1791.

[48] J. M. Pendlebury et al. "Revised experimental upper limit on the electric dipole moment of the neutron". In: *Phys. Rev. D* 92 (9 Nov. 2015), p. 092003. DOI: 10.1103/PhysRevD.92.092003. URL: https://link.aps.org/doi/10.1103/PhysRevD.92.092003.

[49] H. Peng et al. "Cryogenic cavity detector for a large-scale cold dark-matter axion search". In: *Nuclear Instruments and Methods in Physics Research Section A: Accelerators, Spectrometers, Detectors and Associated Equipment* 444.3 (2000), pp. 569–583. ISSN: 0168-9002. DOI: https://doi.org/10.1016/S0168-9002(99)00971-7. URL: https://www.sciencedirect.com/science/article/pii/S0168900299009717.

[50] A. B. Pippard and William Lawrence Bragg. "The surface impedance of superconductors and normal metals at high frequencies II. The anomalous skin effect in normal metals". In: *Proceedings of the Royal Society of London. Series A. Mathematical and Physical Sciences* 191.1026 (1947), pp. 385–399. DOI: 10.1098/rspa.1947.0122. eprint: https://royalsocietypublishing.org/doi/pdf/10.1098/rspa.1947.0122. URL: https://royalsocietypublishing.org/doi/abs/10.1098/rspa.1947.0122.

[51] Luca Planat. "Resonant and traveling-wave parametric amplification near the quantum limit". Theses. Université Grenoble Alpes [2020-....], June 2020. URL: https://theses.hal.science/tel-03137118.

[52] Planck Collaboration et al. "Planck 2015 results - XIII. Cosmological parameters". In: *AandA* 594 (2016), A13. DOI: 10.1051/0004-6361/201525830. URL: https://doi.org/10.1051/0004-6361/201525830.

[53] Frank Pobell. *Matter and Methods at Low Temperatures*. [Online; accessed 2024-03-14]. Springer Science and Business Media, Apr. 2013.

[54] David M. Pozar and David M. Pozar. *Microwave engineering [risorsa elettronica] / David M. Pozar*. eng. Chichester, 2012.

[55] Georg G. Raffelt. "Astrophysical axion bounds". In: *Lect. Notes Phys.* 741 (2008). Ed. by Markus Kuster, Georg Raffelt, and Berta Beltran, pp. 51–71. DOI: 10.1007/978-3-540-73518-2_3. arXiv: hep-ph/0611350.

[56] S.E. Rasmussen et al. "Superconducting Circuit Companion—an Introduction with Worked Examples". In: *PRX Quantum* 2.4 (Dec. 2021). [Online; accessed 2024-03-11].

[57] J I Read. "The local dark matter density". In: *Journal of Physics G: Nuclear and Particle Physics* 41.6 (May 2014), p. 063101. DOI: 10.1088/0954-3899/41/6/063101. URL: https://dx.doi.org/10.1088/0954-3899/41/6/063101.

[58] N. Roch et al. "Widely Tunable, Nondegenerate Three-Wave Mixing Microwave Device Operating near the Quantum Limit". In: *Physical Review Letters* 108.14 (Apr. 2012). [Online; accessed 2024-03-11].

[59] Vera C. Rubin and Jr. Ford W. Kent. "Rotation of the Andromeda Nebula from a Spectroscopic Survey of Emission Regions". In: *apj* 159 (Feb. 1970), p. 379. DOI: 10.1086/150317.

[60] Andrei D Sakharov. "Violation of CP invariance, C asymmetry, and baryon asymmetry of the universe". In: *Soviet Physics Uspekhi* 34.5 (May 1991). DOI: 10.1070/PU1991v034n05ABEH002497. URL: https://dx.doi.org/10.1070/PU1991v034n05ABEH002497.

[61] J. J. Sakurai and Jim Napolitano. *Modern Quantum Mechanics*. [Online; accessed 2024-03-11]. Cambridge University Press, Sept. 2017.

[62] Paolo Salucci. "The distribution of dark matter in galaxies". In: *The Astronomy and Astrophysics Review* 27 (Feb. 2019). DOI: 10.1007/s00159-018-0113-1.

[63] Yannis K. Semertzidis and SungWoo Youn. "Axion dark matter: How to see it?" In: *Science Advances* 8.8 (2022), eabm9928. DOI: 10.1126/sciadv.abm9928. eprint: https://www.science.org/doi/pdf/10.1126/sciadv.abm9928. URL: https://www.science.org/doi/abs/10.1126/sciadv.abm9928.

[64] *Semi-rigid cables for cryogenic applications*. www.keycom.co.jp/eproducts/upj/upj2/page.htm. [Online; accessed 2024-03-14].

[65] C.E. Shannon. "Communication in the Presence of Noise". In: *Proceedings of the IRE* 37.1 (1949), pp. 10–21. DOI: 10.1109/JRPROC.1949.232969.

[66] P. Sikivie. "Experimental Tests of the "Invisible" Axion". In: *Phys. Rev. Lett.* 51 (16 Oct. 1983), pp. 1415–1417. DOI: 10.1103/PhysRevLett.51.1415. URL: https://link.aps.org/doi/10.1103/PhysRevLett.51.1415.

[67] Pierre Sikivie. "Invisible axion search methods". In: *Reviews of Modern Physics* 93.1 (Feb. 2021). ISSN: 1539-0756. DOI: 10.1103/revmodphys.93.015004. URL: http://dx.doi.org/10.1103/RevModPhys.93.015004.

[68] Slawomir Simbierowicz et al. "Characterizing cryogenic amplifiers with a matched temperature-variable noise source". In: *Review of Scientific Instruments* 92.3 (Mar. 2021). ISSN: 1089-7623. DOI: 10.1063/5.0028951. URL: http://dx.doi.org/10.1063/5.0028951.

[69] I. Stern et al. "Cavity design for high-frequency axion dark matter detectors". In: *Review of Scientific Instruments* 86.12 (Dec. 2015), p. 123305. ISSN: 0034-6748. DOI: 10.1063/1.4938164. eprint: https://pubs.aip.org/aip/rsi/article-pdf/doi/10.1063/1.4938164/15838913/123305_1_online.pdf. URL: https://doi.org/10.1063/1.4938164.

[70] Matthew J. Stott and David J. E. Marsh. "Black hole spin constraints on the mass spectrum and number of axionlike fields". In: *Physical Review D* 98.8 (Oct. 2018). ISSN: 2470-0029. DOI: 10.1103/physrevd.98.083006. URL: http://dx.doi.org/10.1103/PhysRevD.98.083006.

[71] M. Tada et al. "Single-photon detection of microwave blackbody radiations in a low-temperature resonant-cavity with high Rydberg atoms". In: *Physics Letters A* 349.6 (2006), pp. 488–493. ISSN: 0375-9601. DOI: https://doi.org/10.1016/j.physleta.2005.09.066. URL: https://www.sciencedirect.com/science/article/pii/S0375960105015343.

[72] Cumrun Vafa and Edward Witten. "Parity Conservation in Quantum Chromodynamics". In: *Phys. Rev. Lett.* 53 (6 Aug. 1984), pp. 535–536. DOI: 10.1103/PhysRevLett.53.535. URL: https://link.aps.org/doi/10.1103/PhysRevLett.53.535.

[73] D.F. Walls and G.J. Milburn. *Quantum Optics*. [Online; accessed 2024-03-11]. Springer Science and Business Media, Dec. 2012.

[74] Steven Weinberg. "A New Light Boson?" In: *Phys. Rev. Lett.* 40 (4 Jan. 1978), pp. 223–226. DOI: 10.1103/PhysRevLett.40.223. URL: https://link.aps.org/doi/10.1103/PhysRevLett.40.223.

[75] Steven Weinberg. "Nonlinear Realizations of Chiral Symmetry". In: *Phys. Rev.* 166 (5 Feb. 1968), pp. 1568–1577. DOI: 10.1103/PhysRev.166.1568. URL: https://link.aps.org/doi/10.1103/PhysRev.166.1568.

[76] F. Wilczek. "Problem of Strong P and T Invariance in the Presence of Instantons". In: *Phys. Rev. Lett.* 40 (5 Jan. 1978), pp. 279–282. DOI: 10.1103/PhysRevLett.40.279. URL: https://link.aps.org/doi/10.1103/PhysRevLett.40.279.

[77] Natalie Wolchover. *Axions would solve another major problem in physics*. [Online; accessed 2024-03-23]. Mar. 2020. URL: https://www.quantamagazine.org/%20axions-would-solve-another-major-problem-in-physics-20200317/.

[78] C. S. Wu et al. "Experimental Test of Parity Conservation in Beta Decay". In: *Phys. Rev.* 105 (4 Feb. 1957), pp. 1413–1415. DOI: 10.1103/PhysRev.105.1413. URL: https://link.aps.org/doi/10.1103/PhysRev.105.1413.